

國立交通大學

電機與控制工程研究所

碩士論文

One-Push 方法於多角度三維 SOI 微結構組裝之
應用

**Assembly of Three Dimensional
Microstructures with Multiple Angles by
One-Push Method on SOI Wafers**

研究生：吳昌修

指導教授：邱一 博士

中華民國九十七年十一月

One-Push 方法於多角度三維 SOI 微結構組裝之
應用

**Assembly of Three Dimensional
Microstructures with Multiple Angles by
One-Push Method on SOI Wafers**

研究生:吳昌修

Student: Chang Shiou Wu

指導教授:邱一

Advisor: Yi Chiu

國立交通大學 電機學院

電機與控制工程研究所

碩士論文

A Thesis

Submitted to Department of Electrical and Control Engineering

College of Electrical Engineering

National Chiao Tung University

In Partial Fulfillment of the Requirement

For the Degree of

Master

In

Electrical and Control Engineering

November 2008

Hsinchu, Taiwan, R.O.C.

中華民國九十七年十一月

中文摘要

近年來在半導體產業的發展之下，微機電製程技術有許多重大的發展。在眾多領域中對於三維微結構的要求也與日俱增，尤其在光學方面的應用對於三維微結構的角度定位要求相當嚴格。

我們最終目標為設計一微光學資訊儲存平台，因此需要精密的角度定位微結構。為了符合光學鏡面平坦度需求，因此利用 SOI (Silicon On Insulator) 基版上的單晶矽製造微鏡面，避免其他材質在製程中因為應力而產生翹曲。此外，我們亦將使用 SU-8 當結構層來製造出平面微結構，由於 SU-8 有良好的機械特性和低溫製程，可使往後的電路整合更加容易。

本實驗室之前已提出利用單一下壓動作 (One-Push) 即可使微鏡面成功的組裝在 90° 的設計，本論文將利用此 One-Push 方法，將多個垂直微鏡面結構以一次下壓動作同時組裝起來，以實現批次組裝的概念，符合未來在晶圓級組裝節省時間的需求。本論文並且提出 45° 鏡面組裝方式，以便應用在光學資訊平台，同時也探討了利用 SU-8 光阻來當結構層對於角度定位的影響。最後，本論文也應用垂直微結構來製造角反射器 (corner cube reflector)。

本論文已經成功的利用一排探針一次組裝三個微鏡面結構，比起分別組裝的時間減少了 46%。同時也利用 90° 微鏡面的概念製造出角反射器，並且利用光學方法量測光反射後的角度誤差為 $1.19^\circ \pm 0.4^\circ$ 。對於原始 90° 結構的誤差問題提出造成誤差的原因以及改善方式，使得角度從 $89.2 \pm 0.3^\circ$ 改善為 $89.8 \pm 0.3^\circ$ 。最後，本論文製造出 45° 三維微結構，平均角度為 $45.9 \pm 0.2^\circ$ ，未來可以應用於其他角度的微結構。然而扭力樑的設計有所不當，造成扭力樑回復力太大使結構產生變形，未來仍有改善空間。

Abstract

Recently, the Micro Electro Mechanical Systems (MEMS) technology has many important developments with the rapid progress in the semiconductor industry. Many applications demand three-dimensional (3-D) structures. Especially in optics, the angular accuracy of the 3-D microstructures is important.

In this thesis, silicon on insulator (SOI) wafers with almost zero stress are used to avoid stress-induced curvature for optical applications. SU8 has good mechanical property and low process temperature, making it suitable for another structural layer and integration with circuit.

In our previous study, micromirrors were assembled using a novel simple one-push operation. In this thesis, batch assembly of more than one 90° microstructures is demonstrated to reduce the assembly time on the wafer level in the future. An assembly method for 45° structures is proposed to be applied to the optical bench. The angular deviation due to the SU-8 structural layer is also discussed. Finally, the corner cube reflector is fabricated by two 90° out-of-plane microstructure.

Three mirrors are lifted up by an array of microprobes to demonstrate batch assembly in this thesis. The assembly time is reduced by 46%, compared to assembling three mirrors individually. A corner cube is fabricated by two 90° micromirrors. The deviation of the corner cube reflector is measured optically, which is $1.19^\circ \pm 0.4^\circ$. The angular deviation of 90° structure is studied with different flip-up angles of the side latches. The 90° structures are improved from $89.2 \pm 0.3^\circ$ to $89.8 \pm 0.3^\circ$. The design of the 45° assembly method is verified. The devices are fabricated with an average angle of $45.9 \pm 0.2^\circ$. The method can be applied to structures with any other angles. Problems encountered during the study, such as the robustness of torsional beams, are discussed for further work.

致謝

隨著論文的完成，碩士生涯也進入了尾聲，感謝許多人幫助我完成碩士的旅程，我要感謝我的父母，讓我沒有後顧之憂的完成碩士生涯。接著要感謝的是我的指導教授邱一老師，在我的學業旅途中給了我很多專業的指導以及建議，讓我學習到很多關於研究與處事的方法，並且教導我用嚴謹的態度來面對研究的每一個細節，讓我的實驗完成的更加順利。再來要感謝已經畢業的光電所李企桓學長，不僅在學業上指導許多，也常常利用會議前時間分享人生豐富的經驗談，讓我的研究生活不苦悶。已經畢業的煒智學長，感謝你在工作的繁忙之中還能常常撥空幫我分析實驗的困難問題點，讓我的實驗問題迎刃而解。感謝電控所的侯冠州學長與動機所的蕭勝議學長，教導我學業上專業的學識。

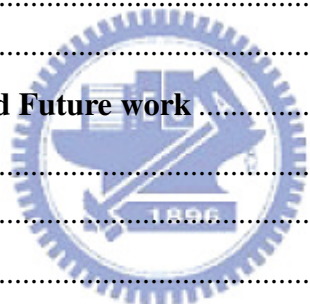
在奈米中心做實驗苦悶的日子，最需要的就是實驗室的夥伴，實驗室的良好氣氛可以讓我把煩悶一掃而空，感謝繁果學長、煒智學長、子麟、弘諳、昇儒陪我度過在實驗室的日子，還有在做完組裝實驗一起互相加油打氣的邱俊誠老師實驗室的夥伴們。大學時代也正在攻讀碩士的朋友們，謝謝你們可以在我無數個做完實驗煩悶的夜晚跟我暢談，讓我累積的壓力得以紓解。

最後再一次感謝我的父母以及我的家人朋友們，感謝你們的鼓勵支持以及幫助，並且期許我在研究所生涯中學到的無論是待人的方法或者是處事的態度，對於我的人生有所幫助，進而在未來有所成就並且貢獻回饋予社會。

Table of Content

中文摘要.....	i
Abstract.....	ii
誌謝.....	iii
Table of Content.....	iv
List of Figures.....	vi
List of Tables.....	xi
Chapter 1 Introduction.....	1
1-1 Motivation.....	1
1-2 Literature survey	3
1-2-1 Microfabricated hinges	3
1-2-2 Three dimensional MEMS by powered assembly	5
1-2-3 Three dimensional MEMS by self assembly	9
1-2-4 Manual or robotic assembly.....	12
1-2-5 Conclusion	17
1-3 Objective and organization of the thesis.....	18
Chapter 2 Principle and Design.....	19
2-1 One-push assembly process	19
2-1-1 V-shaped hinge.....	21
2-1-2 Improvement and extension of previous work.....	21
2-2 Device design.....	22
2-2-1 Batch assembly	22
2-2-2 V-shaped hinge.....	23
2-2-3 Side latch.....	24
2-2-4 Corner cube reflector	25
2-2-5 45° mirror design	26
2-2-6 135° mirror design	30
2-3 Summary.....	31
Chapter 3 Fabrication Process.....	32
3-1 Process flow	32
3-1-1 Device 1	33
3-1-2 Device 2	44
3-2 Fabrication issues and solutions.....	47

3-2-1	Structure patterning.....	47
3-2-2	Oxide etching	48
3-2-3	Vapor HF release.....	48
3-3	Summary	51
Chapter 4	Measurement and Results	52
4-1	Batch assembly	52
4-1-1	Problems	54
4-2	Reflective coating	55
4-3	V-shaped hinge.....	57
4-3-1	Strength of the V-shaped hinge	59
4-4	Angular accuracy of 90° mirrors.....	60
4-5	Corner cube reflector	63
4-5-1	Optical measurement	65
4-6	45° structures	68
4-6-1	Device 1	68
4-6-2	Device 2	71
4-7	Summary	78
Chapter 5	Conclusion and Future work	79
5-1	Conclusion	79
5-2	Future work.....	79
Reference	82



List of Figures

Figure 1-1 Examples of optical MEMS applications, (a) on-chip optical-disk pickup head system ,, (b) microlens scanner with integrated polymer microlens [5], (c) optical cross-connect switches [6].	2
Figure 1-2 (a) Cross section view of fabrication processes, (b) SEM figure of a hinged structure [8].	4
Figure 1-3 (a) Cross section view of the improved hinge, (b) SEM figure [9].	5
Figure 1-4 (a) Cross section view of a SDA, (b) working principle of SDA [10].	6
Figure 1-5 (a) SEM of a free-rotating hinged micromirror lifted by an array of SDA, (b) structure is lifted by SDA [11].	6
Figure 1-6 Schematics of electrostatic force assembly by parallel plates, (a) the voltage is off, (b) the voltage is on.	7
Figure 1-7 Sequence of assembly, (a) ultrasonic vibrations heat and charge the	7
Figure 1-8 (a) Magnetic force assembly, (b) SEM of an assembled structure [14].	8
Figure 1-9 Sequence of magnetic force assembly [14].	9
Figure 1-10 Principle of the polyimide V-groove joint [16].	10
Figure 1-11 Large bending by connecting a series of V-grooves [16].	10
Figure 1-12 (a) Fabrication process for surface tension assembly, (b) self-assembled mirror by surface tension [17].	11
Figure 1-13 (a) Schematic of the structures, (b) assembled structure by combining bimorph beams with locking mechanism [19].	12
Figure 1-14 Conventional assembly process.	13
Figure 1-15 (a) Microgripper is attached to substrate by tethers, (b) metal tip bonded to solder pad [21].	14
Figure 1-16 (a) Solder bonded metal tip is attached to the pad, (b) the micro-part is grasped by the microgripper, (c) the micro-part is inserted in the slot [21].	14

Figure 1-17 SEM of (a) assembled out-of-plane structures, (b) microcoil [21].	15
Figure 1-18 Comparison between (a) conventional beam and (b) serpentine spring [22].	16
Figure 1-19 Assembly procedure (a) no actuation force, (b) the bottom of the device touches the substrate, (c)(d)(e) the conceptual force diagram when the probe moves in lateral direction, (f) finally the structure is at upright position [22].	16
Figure 1-20 (a) Optical microscope view of assembly process, (b) SEM image [22].	17
Figure 2-1 (a) 3-D model, (b) layout design for one-push method [7].	20
Figure 2-2 Assembly process of one-push method [7].	20
Figure 2-3 V-shaped hinge (a) 3-D model, (b) cross section view of the v-shaped hinge, (c) top view.	22
Figure 2-4 (a) Array of microprobes, (b) schematic of batch assembly.	23
Figure 2-5 (a) Conventional hinge, (b) V-shaped hinge.	23
Figure 2-6 Locking height of the side latches.	24
Figure 2-7 Different locking angles of the side latches.	25
Figure 2-8 (a) Illustration of a corner cube reflector, (b) 3D schematic.	25
Figure 2-9 (a) Layout design of Device 1, (b) 3-D solid model.	26
Figure 2-10 Assembly procedure of the device 1 with only one-push operation.	27
Figure 2-11 (a) Layout design of device 2, (b) 3-D model.	28
Figure 2-12 Assembly process of the device 2.	29
Figure 2-13 Form and dimensions of cross sections.	30
Figure 2-14 (a) Illustration of 135° structure, (b) 3D schematic.	31
Figure 3-1 Fabrication process (Device 1).	33
Figure 3-2 Schematic of the vapor HF release setup.	44
Figure 3-3 Temperature measurement before vapor HF release.	44

Figure 3-4 Fabrication process (Device 2).....	46
Figure 3-5 (a) Illustration of AZ4620 photoresist as the etching mask, (b) before baking, (c) after baking.	48
Figure 3-6 (a) Water stains on the chip after vapor HF etching, (b) after baking.....	50
Figure 3-7 Fabricated devices, (a) 90° device without side latch, (b) close-up view of the V-shaped hinge, (c) corner cube reflectors, (d) 45° device.....	51
Figure 4-1 Setup for batch assembly.....	53
Figure 4-2 Sequence of batch assembly of three mirrors, (a) probes are aligned to the push pads, (b) the middle mirror was pushed up first, (c) other mirrors were assembled subsequently, (d) mirrors were assembled at 90°	53
Figure 4-3 Sequence of a failed batch assembly, only two samples were pushed up..	55
Figure 4-4 (a) Mirror before coating (b) mirror after coating.....	56
Figure 4-5 (a) Layout of the conventional hinge, (b) right side, (c) left side.	57
Figure 4-6 (a) Layout of the V-shaped hinge, (b) SEM photograph of the V-shaped hinge, (c) zoom in of the V-shaped hinge.	58
Figure 4-7 (a) SEM photograph of 90° mirror without side latch, (b) and (c) the same sample taken at two measurements.....	59
Figure 4-8 Step in the SU-8 photoresist, (a) layout design (b) cross section, (c) schematic, (d) SEM photograph of the SU-8 step [7].....	61
Figure 4-9 Change the SU8-step in layout, (a) layout design, (b) cross section.....	61
Figure 4-10 Offset of the mirror plate.....	62
Figure 4-11 Side latches with different flip-up angles, (a) 10°, (b) 20°, (c) 40°.	63
Figure 4-12 Measured angle of mirrors with different side latches angles.....	63
Figure 4-13 (a) Assembled corner cube reflector, (b) surfaces of the corner cube reflector.	64
Figure 4-14 SEM photograph of the fabricated corner cube reflector.	64

Figure 4-15 Illustration of the optical measurement.....	65
Figure 4-16 (a) Experimental setup, (b) highlight of the corner cube reflector.....	65
Figure 4-17 Optical path alignment, (a) laser beam alignment, (b) lens and beam splitter alignment.	66
Figure 4-18 Reflected spots on the screen placed at (a) 10 mm, (b) 60 mm away from the beam splitter.	67
Figure 4-19 Angular deviation of the corner cube reflector.....	67
Figure 4-20 Fabricated Device 1, (a) 45° structure, (b) support of 45° structure (b) 135° structure, (d) support of 135° structure.	68
Figure 4-21 Mechanical steps in SU-8, (a) 45° device, (b) 135° device.	69
Figure 4-22 Cross sectional view, (a) After SU-8 process. (b) problem of the assembly process.....	70
Figure 4-23 SEM of 135° devices, (a) restoring force beam was destroyed due to the step, (b) the step lock the structure out of rotational axis.	70
Figure 4-24 Assembly process of a 45° mirror without SU-8, (a) before assembly, (b) the mirror was first aligned and pushed up by Probe 1.....	71
Figure 4-25 (a) An assembled 45° device, (b) side view of 45° device, (c) Highlight of the locking mechanism, (d) torsional beam and mechanical stop (continued).	73
Figure 4-26 An assembled mirror at 45.8°.....	74
Figure 4-27 The bent supports, (a) side view, (b) perspective view.	75
Figure 4-28 Bending of the supports after assembly, (a) 3-D profile.	75
Figure 4-29 (a) Simulation of the support, (b) side view.	76
Figure 4-30 (a) Simulation of a thicker support, (b) side view.....	76
Figure 4-31 Broken torsional beam.	77
Figure 5-1 Micro optical bench.....	80

Figure 5-2 Fabrication process of the optical bench.....81



List of Tables

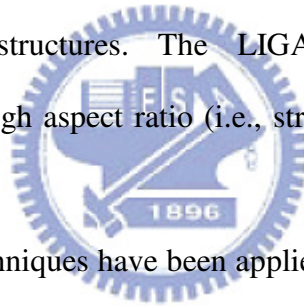
Table 3-1 Parameters of vapor HF release	43
Table 3-2 Modified parameters of vapor HF release	49
Table 4-1 Different rotation angles of the corner cube reflector.....	67
Table 4-2 Angle measurement (resolution: 0.2°)	74



Chapter 1 Introduction

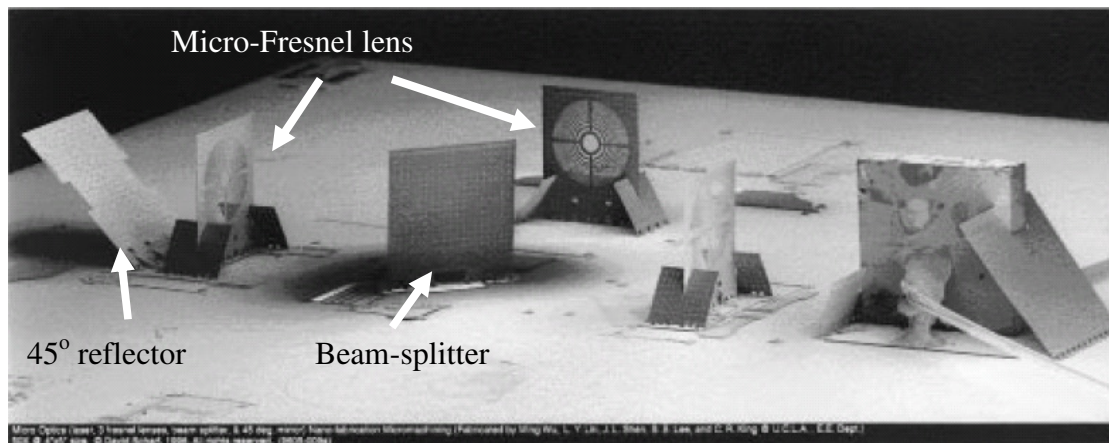
1-1 Motivation

Micro Electro-Mechanical Systems (MEMS) is a technique to fabricate mechanical structures at microscales. Mechanical structures, actuators, sensors, and optical elements in MEMS can be implemented by bulk micromachining [1], surface micromachining [2], and the LIGA processes [3]. Bulk micromachining fabricates micro-components by anisotropic or isotropic etching of the substrate which usually is silicon. Surface micromachining is the planar process by deposition and etching of substrate and sacrificial layers to fabricate mechanical structures. High planar resolution is the advantage of surface micromachining which is the most widely used technique to fabricate microstructures. The LIGA process is suitable for manufacturing structures with high aspect ratio (i.e., structures that are much higher than broad).

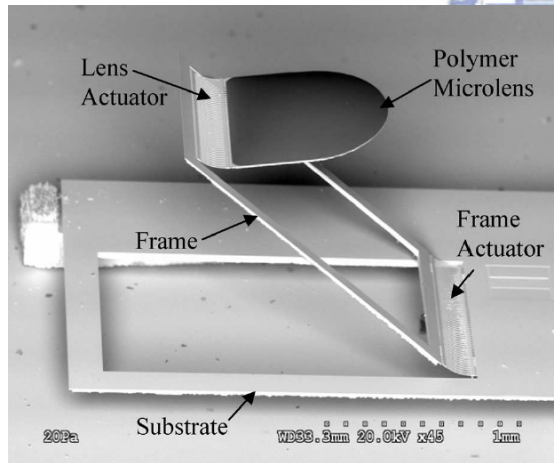


In the past years, MEMS techniques have been applied to optical engineering, and biomedical engineering. In particular, three-dimensional (3-D) out-of-plane structures on the silicon wafers are important components in applications such as free-space optical bench [4]. Figure 1-1 shows the scanning electron micrographs (SEM) of an optical pickup head and other 3-D applications [4-6]. Furthermore, many sensors and actuators also have the demand for 3-D structures. Batch fabrication and assembly processes are important issues for MEMS technique with new 3-D applications. Many techniques for fabricating complex 3-D structure have been proposed in the past 20 years. One of the most important issues for the 3-D structures is angular positioning of out-of-plane structures, especially for optical applications. Based on this demand, a micro assembly process with good positioning accuracy is needed for fabricating an

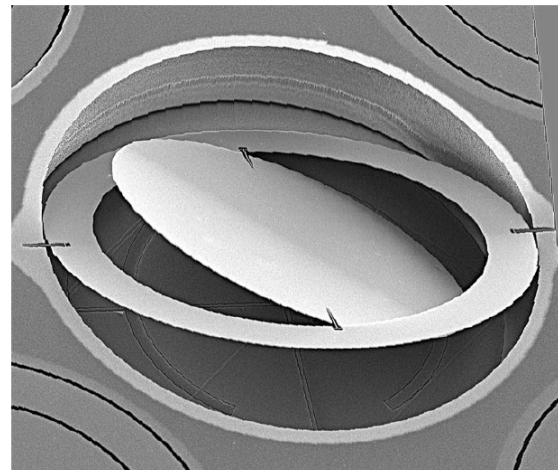
optical bench. In our previous study [7], 90° out-of-plane structures were fabricated and assembled by the proposed one-push method. However, the angular accuracy still needs to be improved and an assembly method for arbitrary angles is also desired. Thus, solving the angular accuracy problem and developing the assembly method for arbitrary angles are the objectives of this thesis.



(a)



(b)



(c)

Figure 1-1 Examples of optical MEMS applications, (a) on-chip optical-disk pickup head system, (b) microlens scanner with integrated polymer microlens [5], (c) optical cross-connect switches [6].

1-2 Literature survey

Most 3-D components are fabricated by surface micromachining and then flipped up to form the 3-D microstructures. Micro hinges are a common solution to anchor the flip-up components. In the past years, many assembly methods for 3-D structures have been proposed. In addition to manual assembly, external forces powered by scratch drive actuators, magnetic force, electrostatic force, or ultrasonic agitation were also used to assemble 3-D structures. Pre-stressed bimorph beams and surface tension were also used for self-assembly. Recently, automatic assembly process was also demonstrated by standard or specially designed equipments. In this section, techniques for 3-D structure assembly are reviewed.

1-2-1 Microfabricated hinges

Surface micromachining is usually used to manufacture MEMS devices with the structure layer thickness less than 5 μm . It was developed in the 80's for combining MEMS and planar integrated circuits (IC) technology on a common silicon wafer. In [8], the proposed micro hinge structures enabled the surface micromachined structures to rotate out of the plane. Two structural layers were used to fabricate the hinge. The poly-1 layer was used as structure layer and hinge pin, while the poly-2 layer was used to fabricate the hinge staple that could cover the hinge pin, as shown in Figure 1-2. This invention enabled micro-structures to rotate out of the plane and also opens an important door for future three-dimensional (3-D) applications.

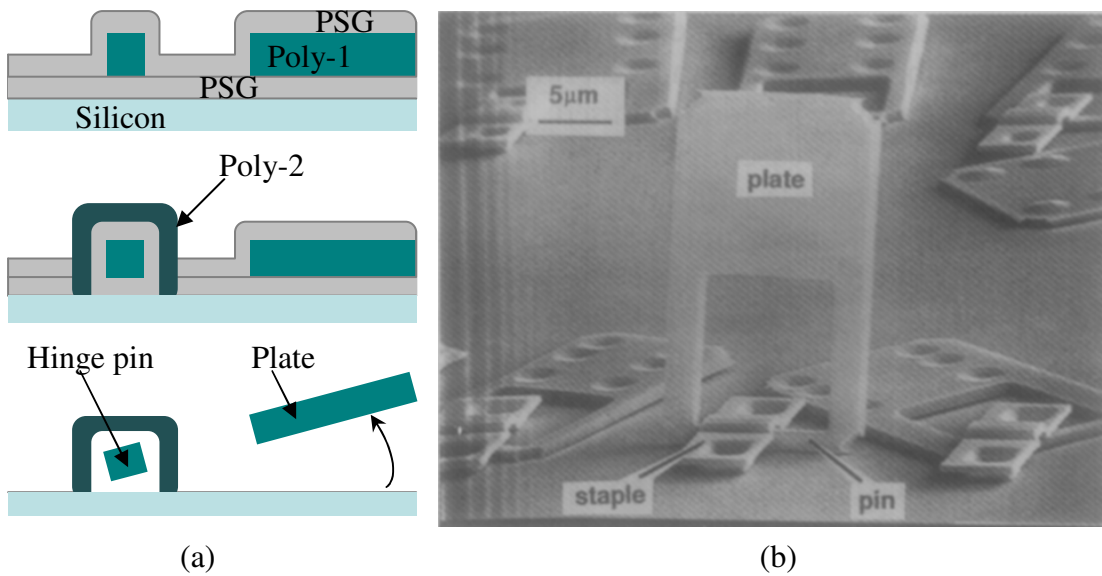


Figure 1-2 (a) Cross section view of fabrication processes, (b) SEM figure of a hinged structure [8].

However, conventional microfabricated hinges have an important problem due to the play between the pin and the staple. Therefore the pin can not be precisely positioned. In order to solve this problem, an improved hinge was proposed [9], as shown in Figure 1-3. A cantilever beam was used to press and fix the hinge pin, which was made wider than the polysilicon layer thickness. The vertical hinge play was eliminated in this invention and the fabricated structure could not shift vertically anymore. However, the lateral play still existed and would cause shift in assembly process.

To eliminate the lateral play and improve the positioning accuracy, a solution was proposed in our previous study [7]. The V-shaped hinge locks the hinge pin in desired axis by the geometric design. The comparison between the V-shaped hinge and the conventional hinge will be presented in Chapter 4.

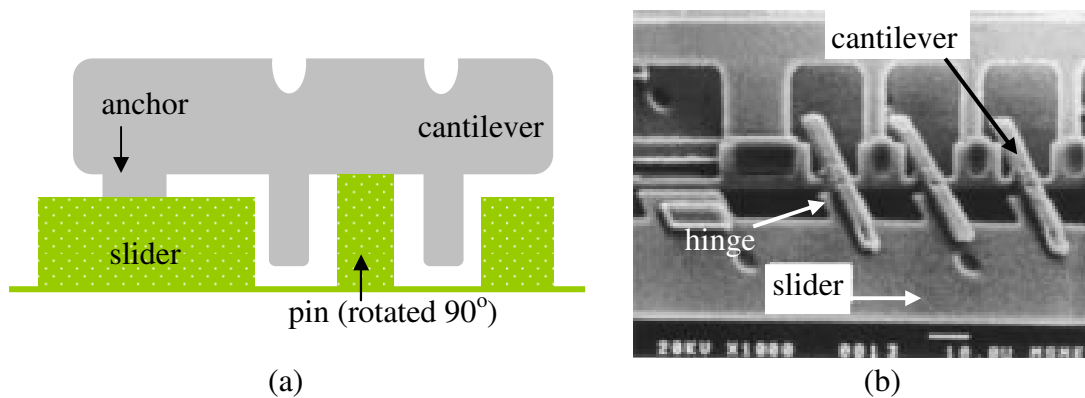


Figure 1-3 (a) Cross section view of the improved hinge, (b) SEM figure [9].

1-2-2 Three dimensional MEMS by powered assembly

Assembly powered external forces such as scratch drive actuators, magnetic force, electrostatic force, and ultrasonic agitation are reviewed in this section.

Scratch drive actuator assembly

The scratch drive actuator (SDA), as shown in Figure 1-4, was proposed in 1993 [10]. A scratch drive actuator is usually composed of a plate, a bushing, an insulator and a substrate electrode, as shown in Figure 1-4 (a). With an applied voltage, the plate is pulled down to the substrate by the electrostatic force. The bushing is tilted at this stage and moves a small distance. Once the voltage is removed, the plate and bushing return to their initial position. With this motion in cycles, the SDA can go forward to the desired position. Figure 1-4 (b) shows the working principle step by step. Figure 1-5 illustrates a micromirror assembled by using an array of SDA [11].

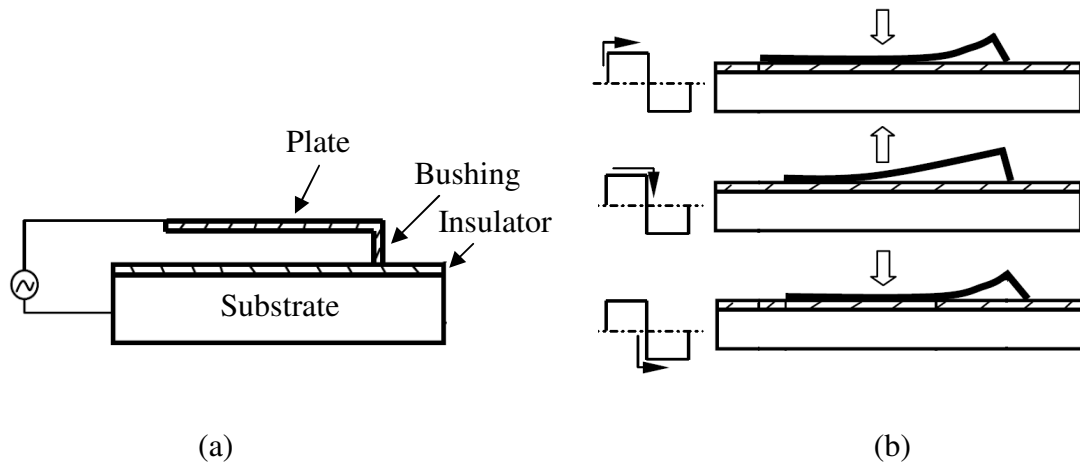


Figure 1-4 (a) Cross section view of a SDA, (b) working principle of SDA [10].

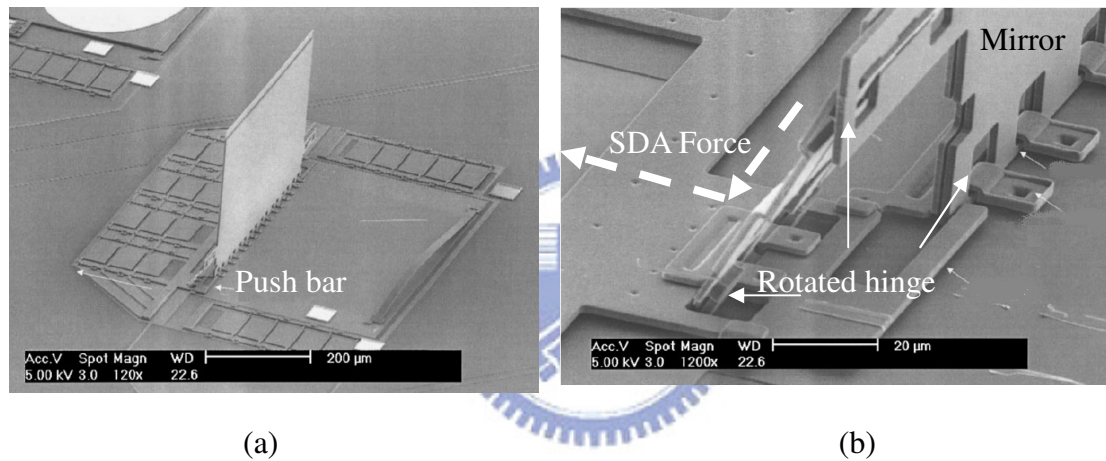


Figure 1-5 (a) SEM of a free-rotating hinged micromirror lifted by an array of SDA, (b) structure is lifted by SDA [11].

Electrostatic force assembly

Electrostatic force generated by parallel plates [12] or ultrasonic waves [13] can be used to assemble 3-D structures. The operation principle of generating electrostatic force by parallel plates is shown in Figure 1-6. When the voltage is applied, the electrostatic attraction force between the ground plane and the hinged plate enables the hinged plate to move out of the plane, as shown in Figure 1-6 (b). The advantage of electrostatic force assembly is easy control of voltage.

In addition to parallel plates, ultrasonic wave is another way to generate electrostatic force. Ultrasonic vibrations are generated with an attached piezoelectric actuator to vibrate polysilicon plates on silicon nitride or polysilicon surfaces [13]. The friction brings contact electrification charge on the substrate and the flap. The electrostatic repulsion force is generated to lift up the flap, as Figure 1-7 shows. The parts were first actuated in ambient pressure (Figure 1-7(a)). However, at atmospheric pressure the structures would not be lifted up due to the air drag on the flaps. As the pressure was low enough with the ultrasound still on, the hinged flaps were lifted up (Figure 1-7(b)).

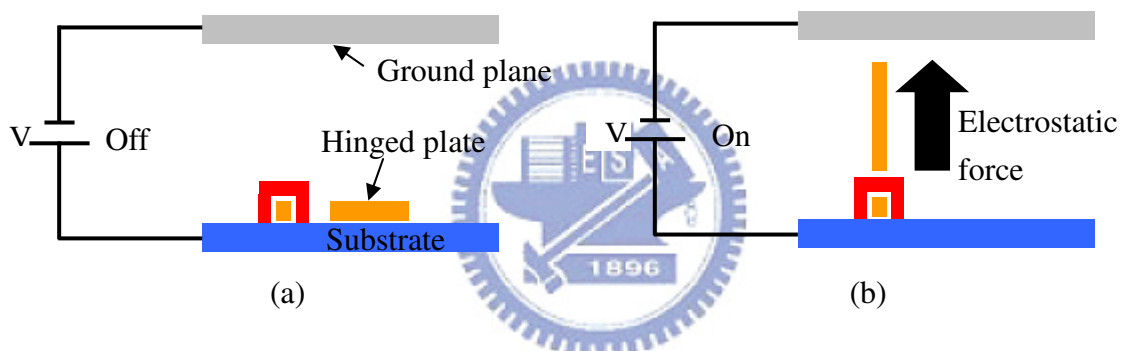


Figure 1-6 Schematics of electrostatic force assembly by parallel plates, (a) the voltage is off, (b) the voltage is on.

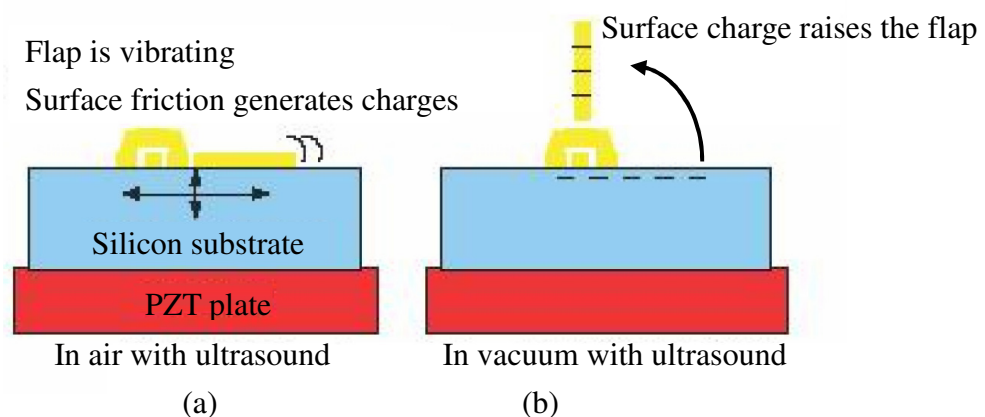


Figure 1-7 Sequence of assembly, (a) ultrasonic vibrations heat and charge the polysilicon parts, (b) electrostatic repulsion forces the plate up [13].

Magnetic force assembly

Magnetic forces can be applied to actuate assemble 3-D structures by passing current through them (Lorentz force) or by depositing magnetic material on them. As shown in Figure 1-8 (a), electroplated magnetic material such as Permalloy is integrated with the hinged flap [14]. When an external magnetic field is applied, the hinged flap will be lifted up and rotate around the rotational axis. The rotation angle is determined from the volume of the magnetic material and the applied external field. Figure 1-8 (b) shows an assembled structure by the magnetic force. By choosing different volume of Permollay electroplated on the flap, a precise sequence assembly can be achieved by changing the magnetic field strength [14, 15]. An example is shown in Figure 1-9. As H_{ext} is increased gradually, the primary flap will be lifted up to 90° first due to the greater volume of Permollay. With the increase of H_{ext} , the secondary flap will be lifted up and lock the primary flap by the friction force.

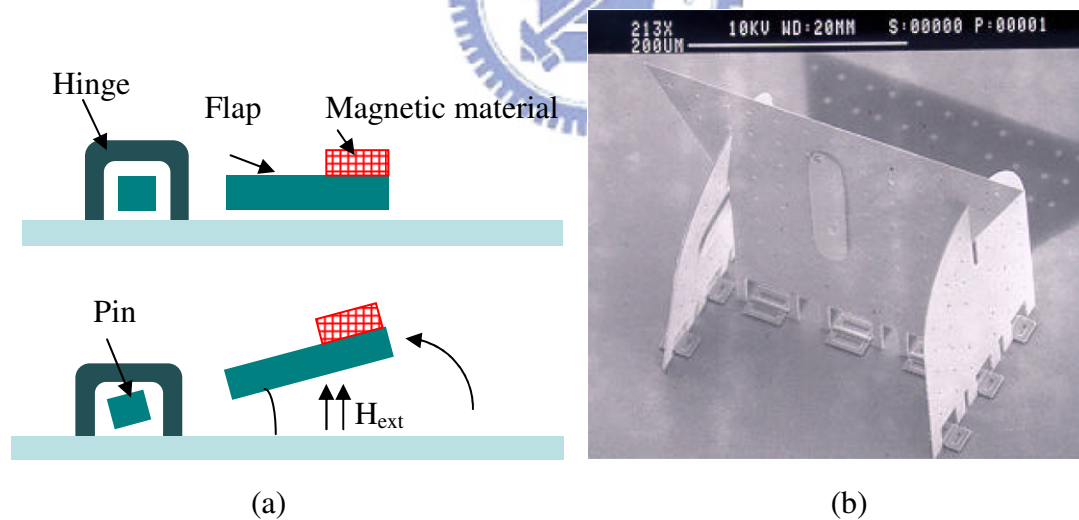


Figure 1-8 (a) Magnetic force assembly, (b) SEM of an assembled structure [14].

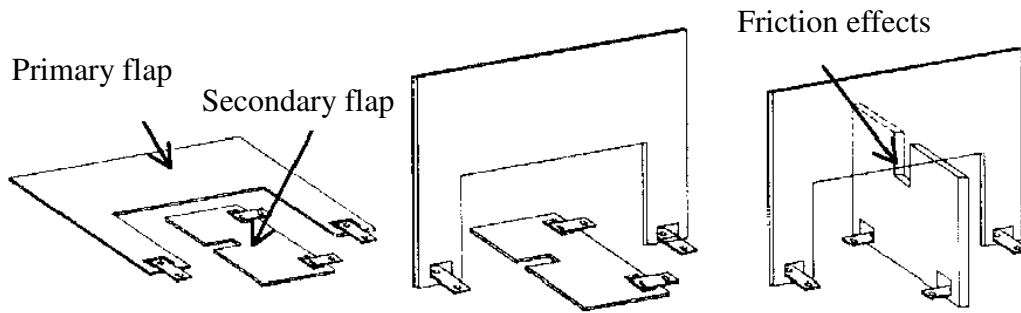
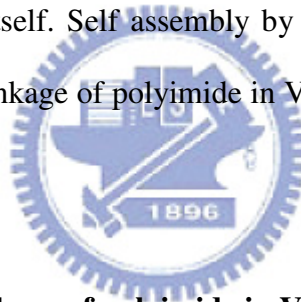


Figure 1-9 Sequence of magnetic force assembly [14].

1-2-3 Three dimensional MEMS by self assembly

Aside from external applied forces, 3-D microstructures can be assembled by the intrinsic force of the fabricated structures. In other words, the fabricated structure can be assembled to 3-D structure itself. Self assembly by pre-stressed bimorph beams, surface tension, and thermal shrinkage of polyimide in V-grooves are reviewed in this section.



Self assembly by thermal shrinkage of polyimide in V-grooves

Thermal shrinkage of polyimide in V-grooves can be used for self assembly as illustrated in Figure 1-10 [16]. V-grooves are etched through a silicon membrane and filled with polyimide. The polyimide in V-grooves shrinks when it is cured. With a larger lateral length of polyimide at the top of the V-groove than at the bottom, the structure bends as a result of to different amount of shrinkage of polyimide. With a series of V-grooves, large bending can be achieved, as shown in Figure 1-11 [16].

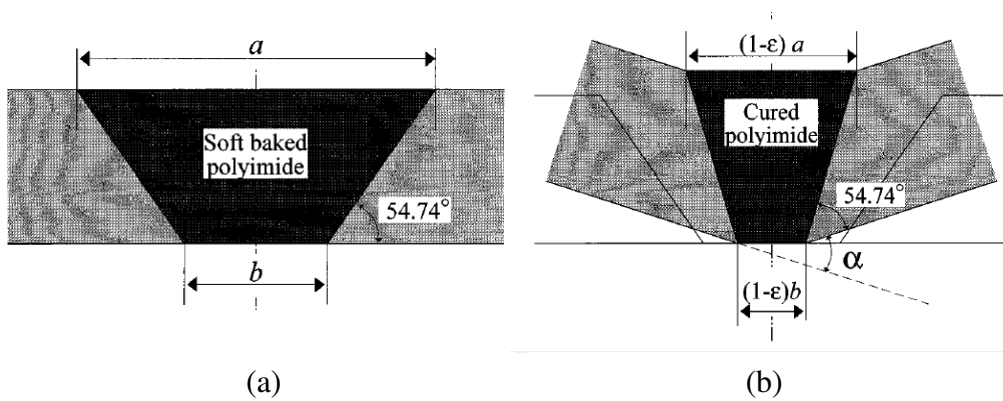


Figure 1-10 Principle of the polyimide V-groove joint [16].

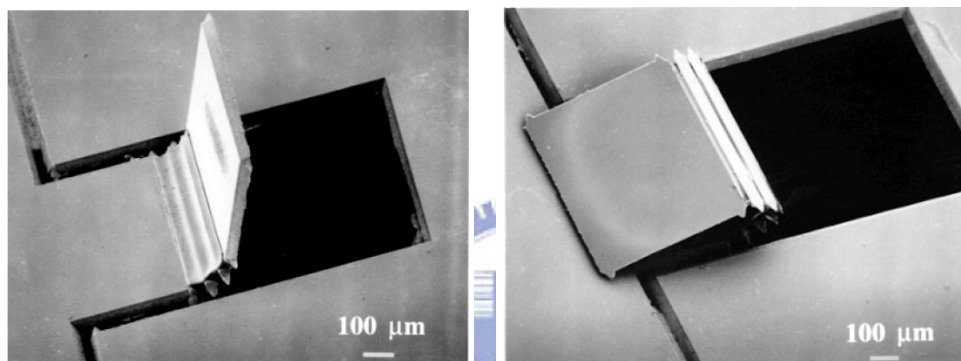


Figure 1-11 Large bending by connecting a series of V-grooves [16].

Surface tension powered self assembly

In surface tension powered self assembly [17], meltable material is patterned on the hinge joint. The plate is flipped up by surface tension when the material is melted. The fabrication process and a fabricated structure are shown in Figure 1-12. The rotation angle of the assembled structures are determined by the geometric features of the meltable material [18].

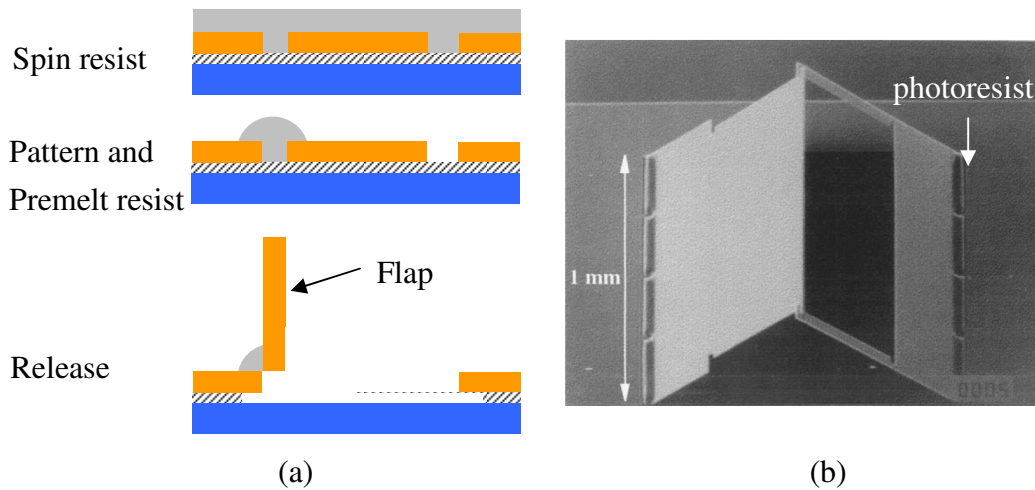


Figure 1-12 (a) Fabrication process for surface tension assembly, (b) self-assembled mirror by surface tension [17].

Stress-induced self assembly

Residual stress of thin film can be used as motive force to assemble 3-D microstructure, as Figure 1-13 shows [19]. The assembly mechanism is composed of stress-induced bimorph beams and locking components. The locking mechanism fabricated in different structure layers is engaged when the micromirror is raised.

Bimorph stress beams can be fabricated by using different materials. However, the stress relaxation is a critical problem. Reliability tests showed that the problem of stress relaxation could be reduced by replacing metal films by dielectric films [20].

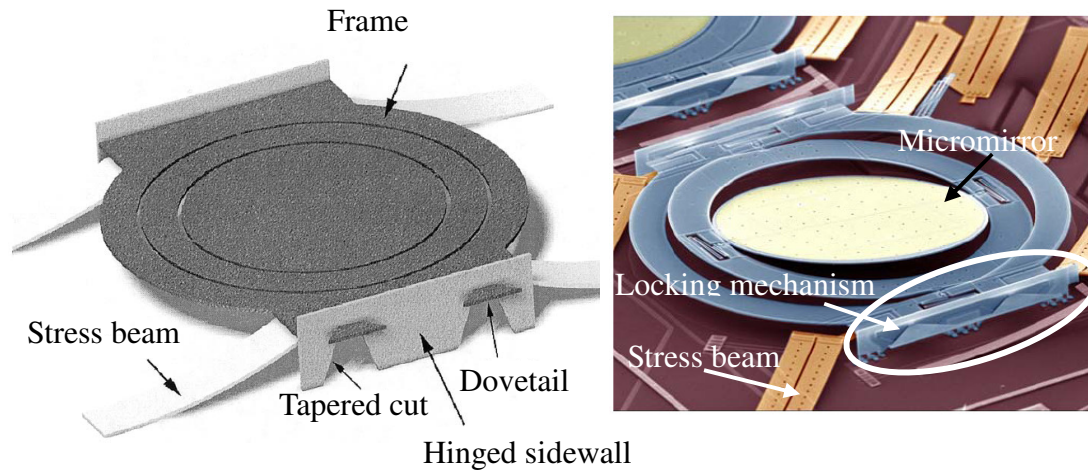
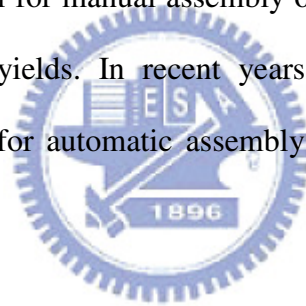


Figure 1-13 (a) Schematic of the structures, (b) assembled structure by combining bimorph beams with locking mechanism [19].

1-2-4 Manual or robotic assembly

Microprobes are the first tool for manual assembly of fabricated micro parts. It is time consuming and has low yields. In recent years, specially designed robotic equipments are also developed for automatic assembly. These assembly techniques are reviewed in this section.



Conventional manual assembly

The conventional manual assembly of a flip-up mirror is illustrated in Figure 1-14. The structure is composed of a mirror plate, two mechanical locks, and a number of hinges. First a microprobe is used to lift up the micromirror to be perpendicular to the substrate. Then the mechanical side locks are picked up by another microprobe while the micromirror is held by the original microprobe. Finally the side locks are folded and locked onto the plate by the V-shaped opening. Precise manipulation of microprobes is needed during the assembly process in this conventional manual assembly.

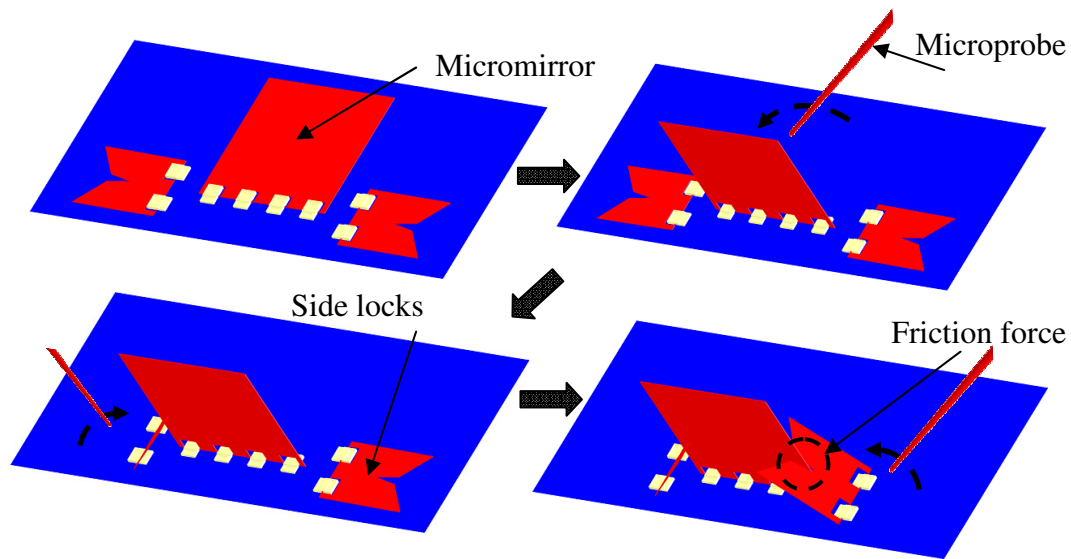


Figure 1-14 Conventional assembly process.

Assembly by microgrippers

Compliant passive microgrippers were proposed to assemble out-of-plane 3-D microstructures [21]. The surface-micromachined microgripper is originally attached to the substrate by tethers, which are weak enough to be pulled apart from the substrate. Figure 1-15 shows the surface micromachined microgripper and the solder bonded microgripper. First, the solder is melt by the heated metal tip which is attached to a robotic arm. Then the metal tip with melt solder on it is aligned and pressed on the solder pad of the microgripper. After cooling, the pad is bonded to the metal tip. The tethers can be easily broken when the arm moves away from the substrate (Figure 1-16 (a)). Next, the microgripper is aligned to the micromachined microparts. The microgripper is inserted into the microparts (Figure 1-16 (b)). After inserting the microparts into the slots on the substrate, the microgripper is released and the assembly is complete (Figure 1-16 (c)). Figure 1-17 shows the SEM figures of the assembled devices.

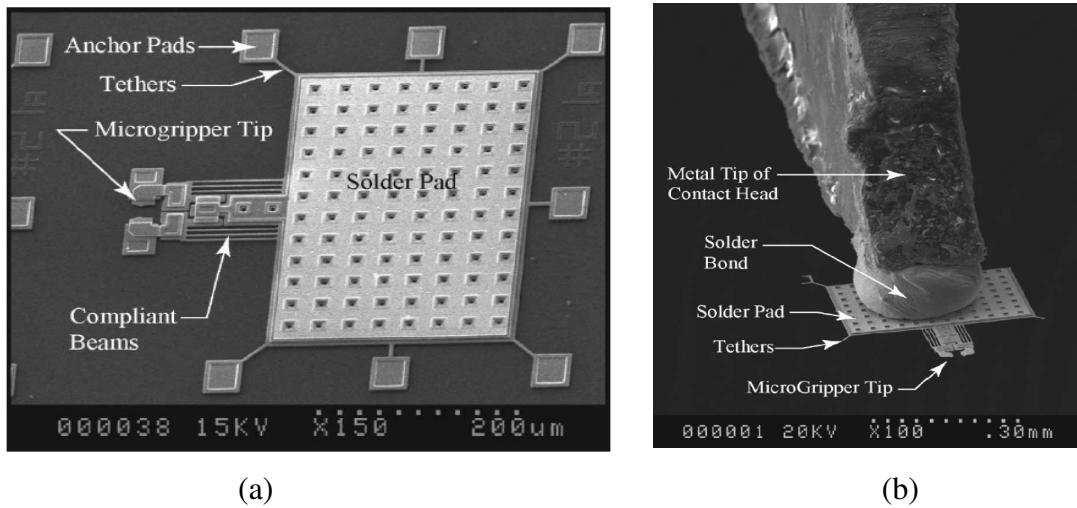


Figure 1-15 (a) Microgripper is attached to substrate by tethers, (b) metal tip bonded to solder pad [21].

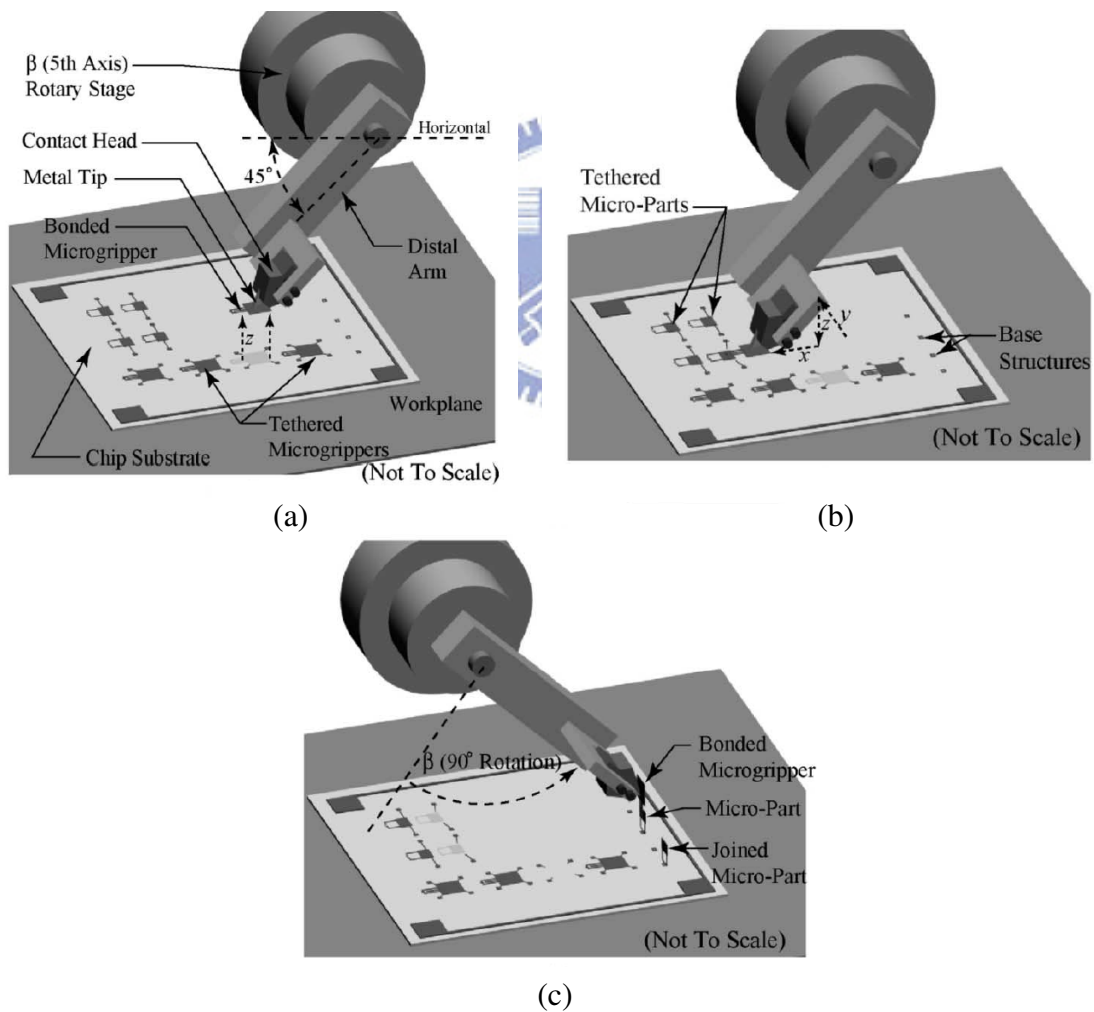


Figure 1-16 (a) Solder bonded metal tip is attached to the pad, (b) the micro-part is grasped by the microgripper, (c) the micro-part is inserted in the slot [21].

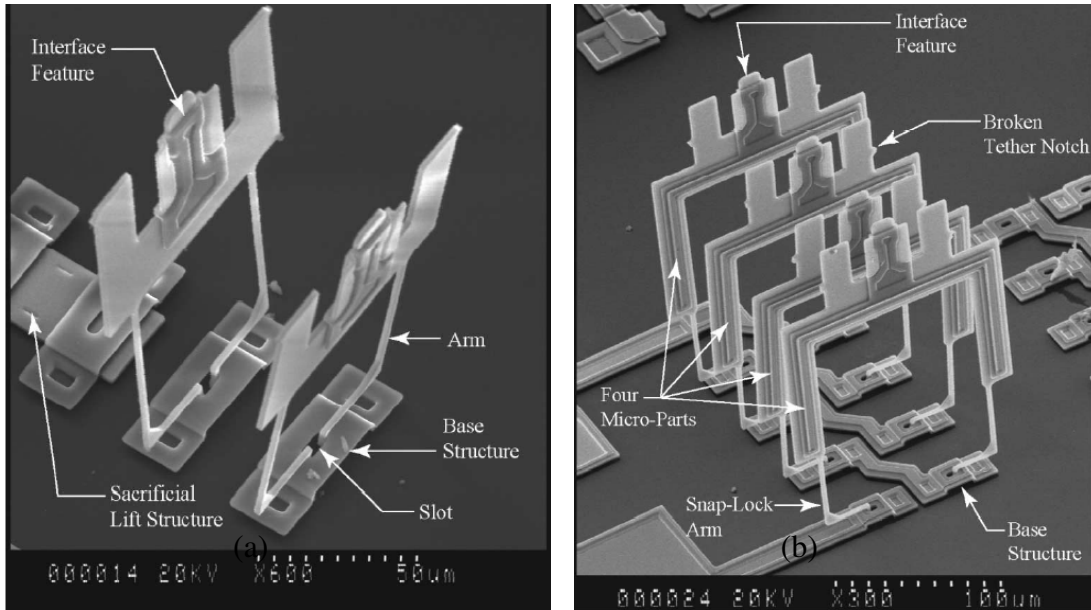


Figure 1-17 SEM of (a) assembled out-of-plane structures, (b) microcoil [21].

Hingeless 90° out-of-plane microstructures

Another novel technique for microassembly is the assembly of hingeless 90° out-of-plane microstructures with the use of automated probing system [22]. Staple hinges are replaced by compliant hinges created using springs or torsion beams, which can produce out-of-plane motion by redirecting lateral displacement into rotation. The structure can be pushed up by a single lateral push. While the conventional springs are compliant in all direction, the serpentine springs are designed to be more compliant in the out-of-plane direction than the in-plane direction, as shown in Figure 1-18. When a lateral force is applied on the actuation pad, the spring is twisted and a 90° out-of-plane motion can be produced. The assembly process is presented in Figure 1-19. The lateral actuation force (F_A) and the restoring force of the springs (F_S) provides an out-of-plane torque after the bottom of the device touches the substrate (Figure 1-19(b)). As the probe moves in lateral direction, the rotational torque (which is associated to F_S) increases because of the deformation of the springs (Figure 1-19(c)(d)). When the plate reaches a particular angle, the spring will begin to

pull the plate until the structure finally reaches the upright position (Figure 1-19(e)(f)). Figure 1-20 (a) shows the manual assembly procedure. Figure 1-20 (b) is an assembled device.

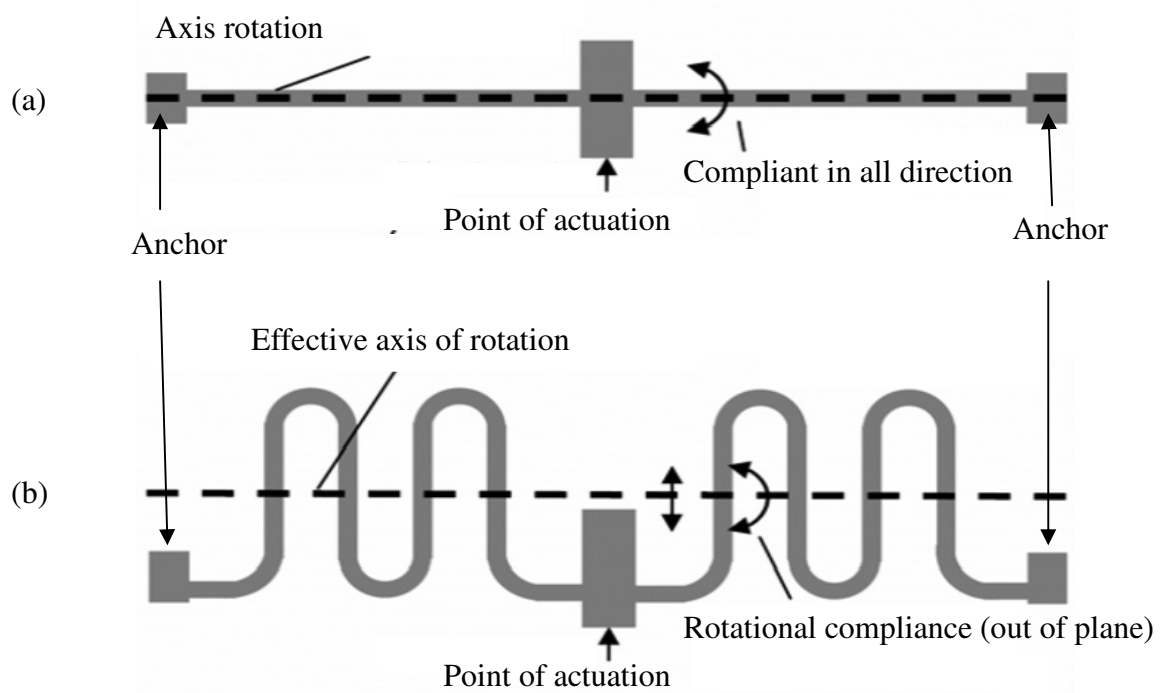


Figure 1-18 Comparison between (a) conventional beam and (b) serpentine spring [22].

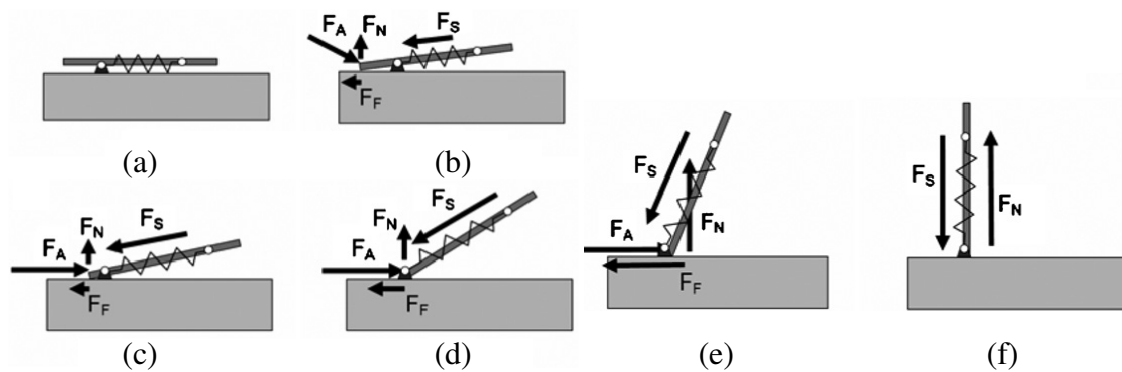


Figure 1-19 Assembly procedure (a) no actuation force, (b) the bottom of the device touches the substrate, (c)(d)(e) the conceptual force diagram when the probe moves in lateral direction, (f) finally the structure is at upright position [22].

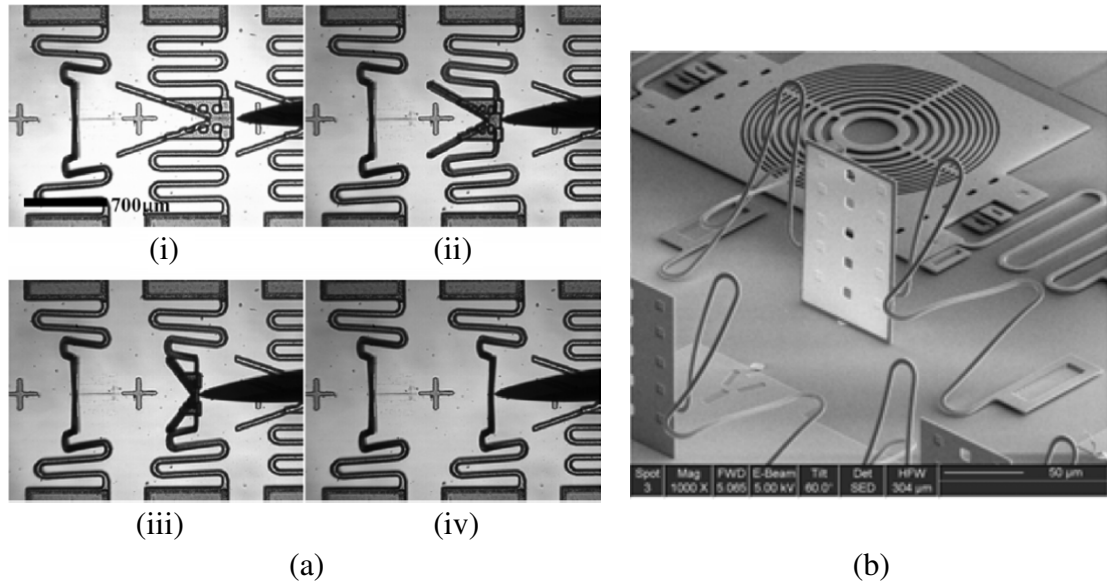


Figure 1-20 (a) Optical microscope view of assembly process, (b) SEM image [22].

1-2-5 Conclusion

Although there are a number of methods for 3-D microstructure assembly, the applications of these methods are limited. Assembly by SDA needs large chip area. Assembly by magnetic or electrostatic force needs materials which are not compatible with IC processes or demands a large electrical field. Parameters of thermal shrinkage of polyimide or surface tension forces are difficult to control. Bimorph stress beams have the problem of stress relaxation. Manual assembly by micromanipulators is time consuming. However, once the steps of manual assembly are simplified enough and automatic equipments can be used, systematic assembly can be achieved.

1-3 Objective and organization of the thesis

In our previous [7], a novel assembly method with one-push operation was proposed to lift up 3-D microstructures. SU-8 was used to fabricate locking mechanism. A novel hinge design was also introduced to improve the positioning accuracy.

Batch assembly in wafer level will be demonstrated in this thesis. The accuracy problem that was found in [7] will be solved. A corner cube reflector is demonstrated based on this method. Furthermore, 45° positioning method needed for optical benches will be introduced. Therefore, the objectives of this thesis are to:

1. demonstrate batch assembly;
2. verify the hinge positioning accuracy;
3. solve the angular accuracy problem;
4. apply the method to a corner cube reflector;
5. demonstrate the assembly method for arbitrary angles.

The basic principles and simulation of the proposed microstructures and assembly method are presented in Chapter 2. The fabrication processes and process issues are discussed in Chapter 3. The experiment and measurement results of the fabricated and assembled devices are showed in Chapter 4. Conclusion and future work are presented in Chapter 5.

Chapter 2 Principle and Design

The major difficulty in the manual assembly of out-of-plane structures is the precise control of microprobes. First, the microprobe must be inserted into the gaps between the released structure and the substrate. Then the microprobe is maneuvered in different directions with precise position control to lift up the microstructure. In our previous study [7], the operation of the probe is simplified to a single push in the proposed one-push method. The advantage of the proposed method is the large probe positioning tolerance in both vertical and lateral directions.

The proposed method was verified in a SOI/SU-8 process developed in our laboratory [23]. The major advantage of the SOI wafer is the better surface smoothness of the single-crystal-silicon (SCS) device layer compared to the surface micromachined polysilicon layer. This is especially important in optical demands. The SU-8 photoresist is used as the second structural layer. The low temperature process is more compatible with circuits than the polysilicon process. Furthermore, the Young's modulus of SU-8 is smaller than silicon [24, 25]. Therefore SU-8 is suitable to fabricate springs or restoring force components.

2-1 One-push assembly process

The concept of the proposed one-push operation is shown in Figure 2-1. In Figure 2-1 (a), the substrate is the 400- μm -thick handle layer of the SOI wafer. The micromirror is defined in the 5- μm -thick device layer, whereas the locking mechanisms are fabricated using SU-8 photoresist. The through-wafer hole provides the operation space for the probes during the assembly procedure. The assembly process is shown in Figure 2-2. When a probe pushes the pad down through the

through-wafer hole, the mirror is flipped up and contacts the bottom of the side latches made of the SU-8 photoresist (Figure 2-2 (a)). The out-of-plane force from the mirror plate will simultaneously drive the flexible side latches to rotate out of the plane (Figure 2-2 (b)). When the mirror plate rotates close to 90°, it will slide into the V-shaped slot of the flexible side latches (Figure 2-2(c)). The V-shaped slot and the downward restoring force of the side-latch spring will firmly lock the mirror plate in place after the probe moves away (Figure 2-2 (d)). The manual assembly process is reduced to a single push motion.

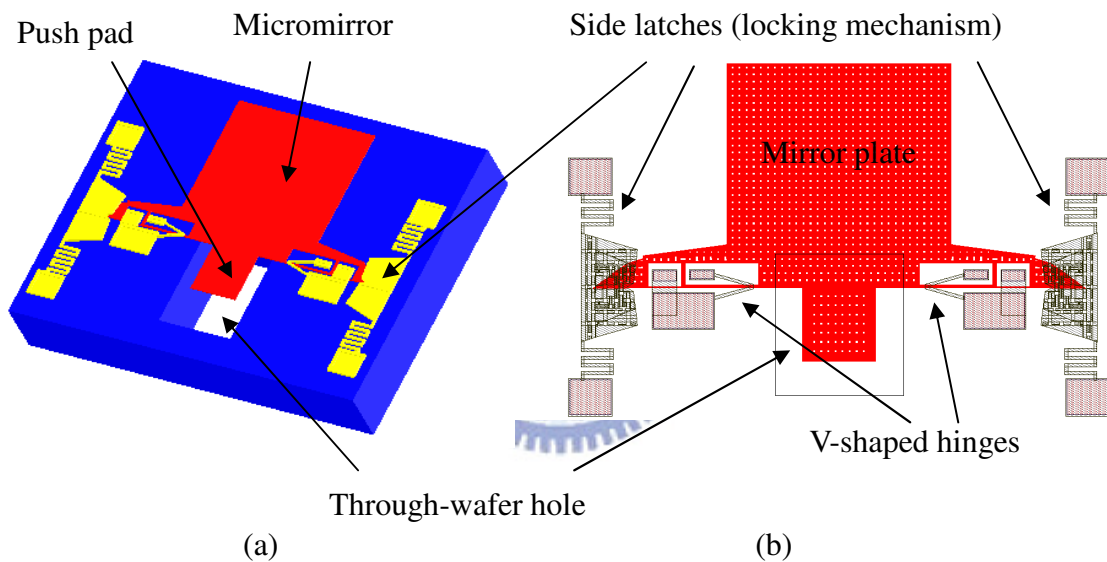


Figure 2-1 (a) 3-D model, (b) layout design for one-push method [7].

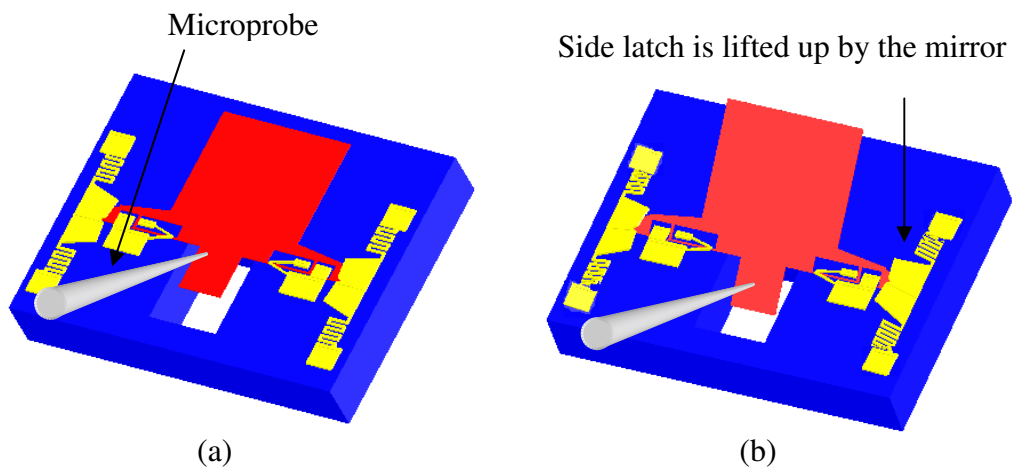


Figure 2-2 Assembly process of one-push method [7].

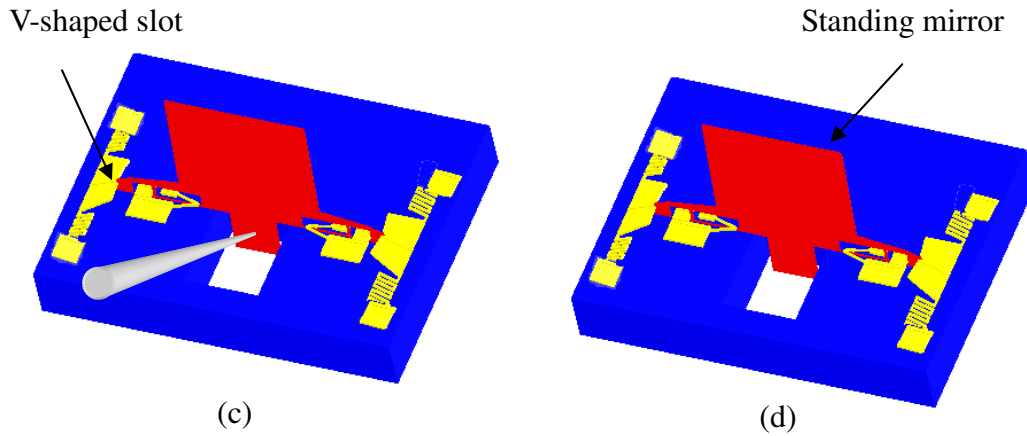


Figure 2-2 Assembly process of one-push method [7] (continued).

2-1-1 V-shaped hinge

3-D mirrors are usually fixed to the substrate by staple hinges. For conventional hinges, play space in the staple is needed for the hinge pins to rotate. However, the play can cause an offset of the pin position during assembly that will affect the final angular accuracy. In our previous study [7], a novel V-shaped hinge with less hinge play was proposed, as shown in Figure 2-3. The restoring force of the V-shaped beams eliminates the vertical play and fixes the hinge pin on the substrate. Furthermore, the hinge pin is locked by the geometry of the V-shaped hinge when the mirror is in the upright position, as shown in Figure 2-3(c). Therefore, the offset of the hinge pins due to the transverse play during assembly can be reduced.

2-1-2 Improvement and extension of previous work

In our previous demonstration [7], the average angle of the assembled 90° micromirrors was $89.2 \pm 0.3^\circ$. The cause and solution of this problem are investigated in this thesis. In this thesis, the batch assembly of more than one device will be demonstrated to reduce the assembly time on the wafer level. Finally, V-shaped hinges are used to fix the position of the flip-up structures without conventional hinges or side latches.

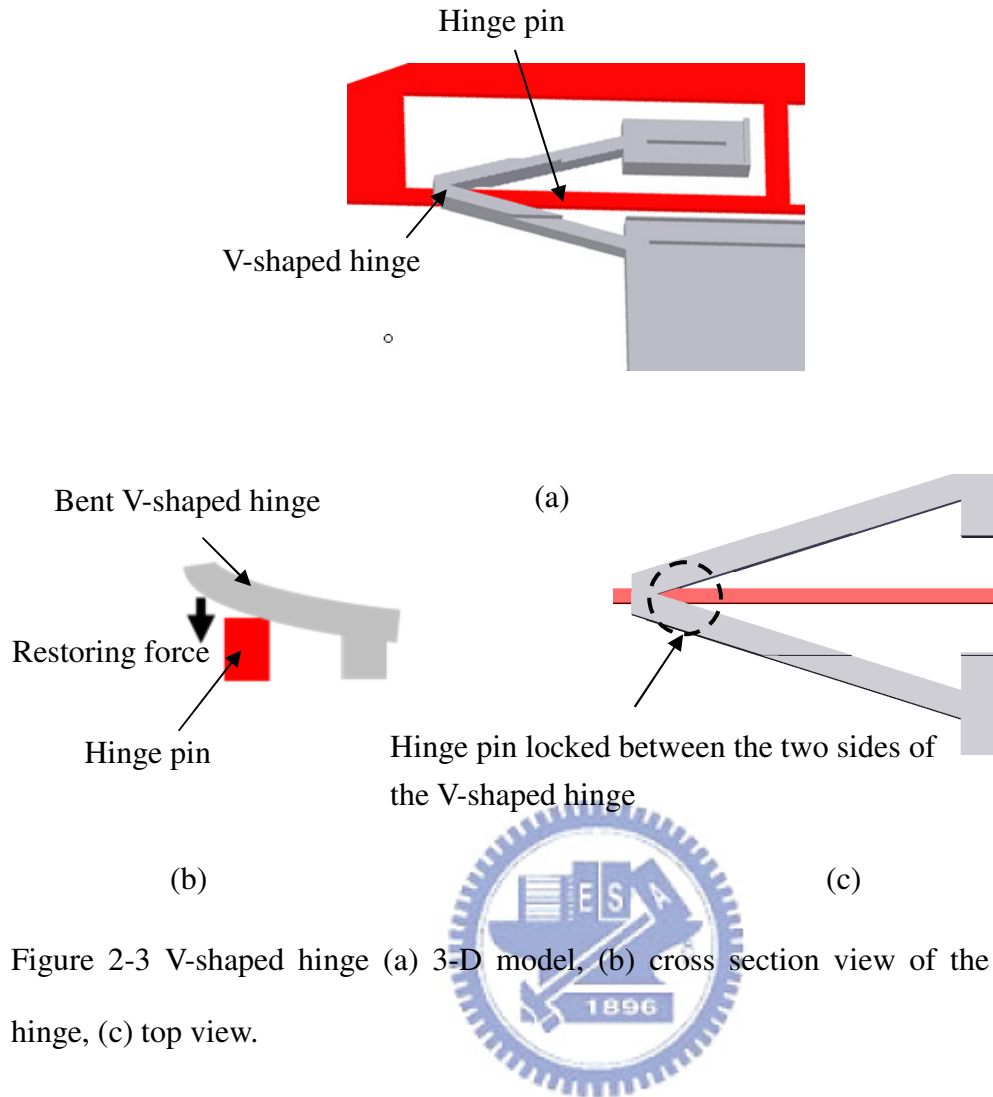


Figure 2-3 V-shaped hinge (a) 3-D model, (b) cross section view of the v-shaped hinge, (c) top view.

2-2 Device design

Batch assembly is realized by three mirrors and an array of microprobes. Several side latches for 90° structures are designed to investigate the offsets on the angular accuracy. A corner cube reflector is designed as another application of the one push assembly method. Mechanisms for 45° and 135° device assembly are proposed and designed.

2-2-1 Batch assembly

The schematic of batch assembly is shown in Figure 2-4. An array of microprobes

are connected to a micropositioner to push an array of the micromirrors simultaneously. The distance of the microprobes is the same as the distance of the push pads, which is 2 mm. The sizes of the mirror plate and the push pad are $(760 \mu\text{m})^2$ and $(250 \mu\text{m})^2$, respectively.

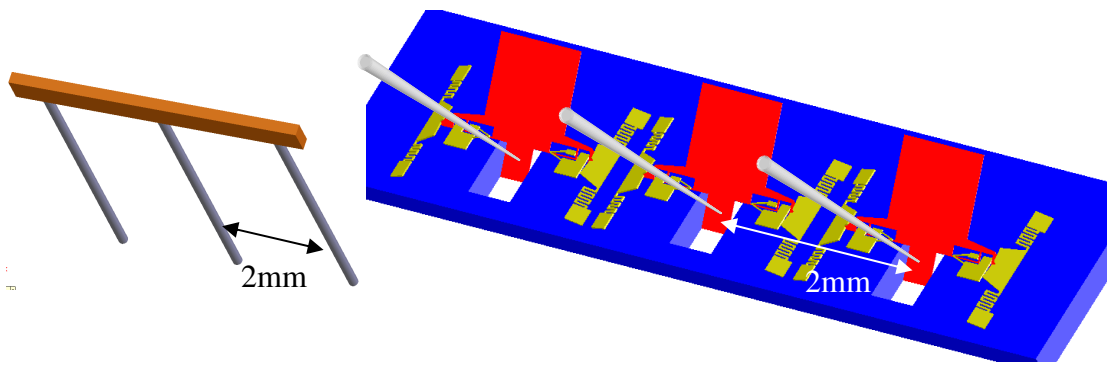


Figure 2-4 (a) Array of microprobes, (b) schematic of batch assembly.

2-2-2 V-shaped hinge

Axis positioning accuracy is compared between a V-shaped hinge and a conventional hinge, as shown in Figure 2-5. The V-shaped hinge in Figure 2-5 (b) is the same as in [7]. The axis offsets of the two designs will be measured and discussed in Chapter 4. The width of the hinge pin of the V-shaped hinge is $15 \mu\text{m}$ and the deposited oxide is $3 \mu\text{m}$ thick. A mirror without side latch is also designed to test the robustness of the V-shaped hinge.

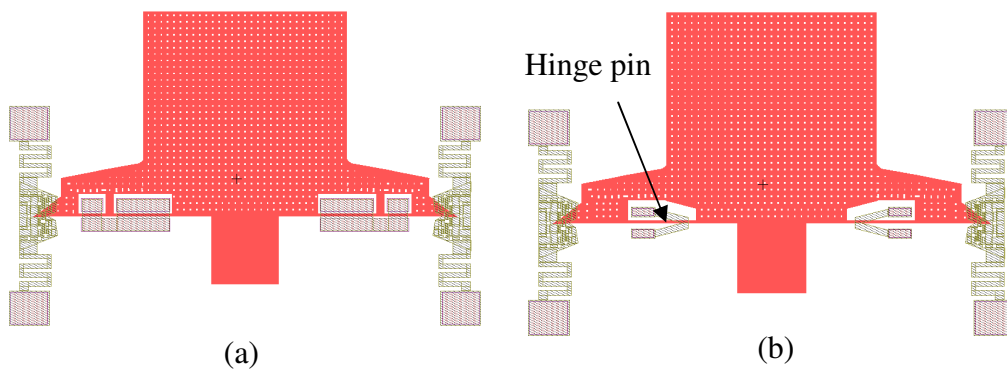


Figure 2-5 (a) Conventional hinge, (b) V-shaped hinge.

2-2-3 Side latch

Side latches are used to lock the side plates of the mirror plates. The locking height affects the robustness of the assembled structure. For lower locking height, the same offset at locking point should result in greater angular deviation. However, the friction force between the silicon and the SU-8 photoresist affects the locking position. As Equation 2-1 shows, F is the friction force, μ is the coefficient of friction, and F_N is the normal force exerted on the surfaces. A larger flip-up angle of the side latch will result in a large F_N due to the increased restoring force from the spring (Figure 2-6).

$$F = \mu \cdot F_N \quad (2-1)$$

The side latch spring is designed to be rigid in the out-of-plane direction in order to lock the mirror plate. The geometric design of three locking angles is shown in Figure 2-7, where A is the locking height and B is the projection on the substrate of the locking position to the end of the side latch plate. The flip-up angle of the side latch is 10° , 20° , and 40° in Figures 2-7 (a), (b), and (c), respectively.

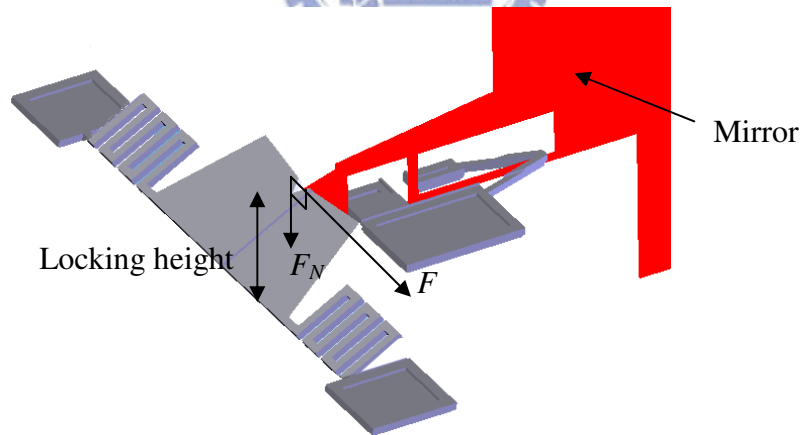


Figure 2-6 Locking height of the side latches.

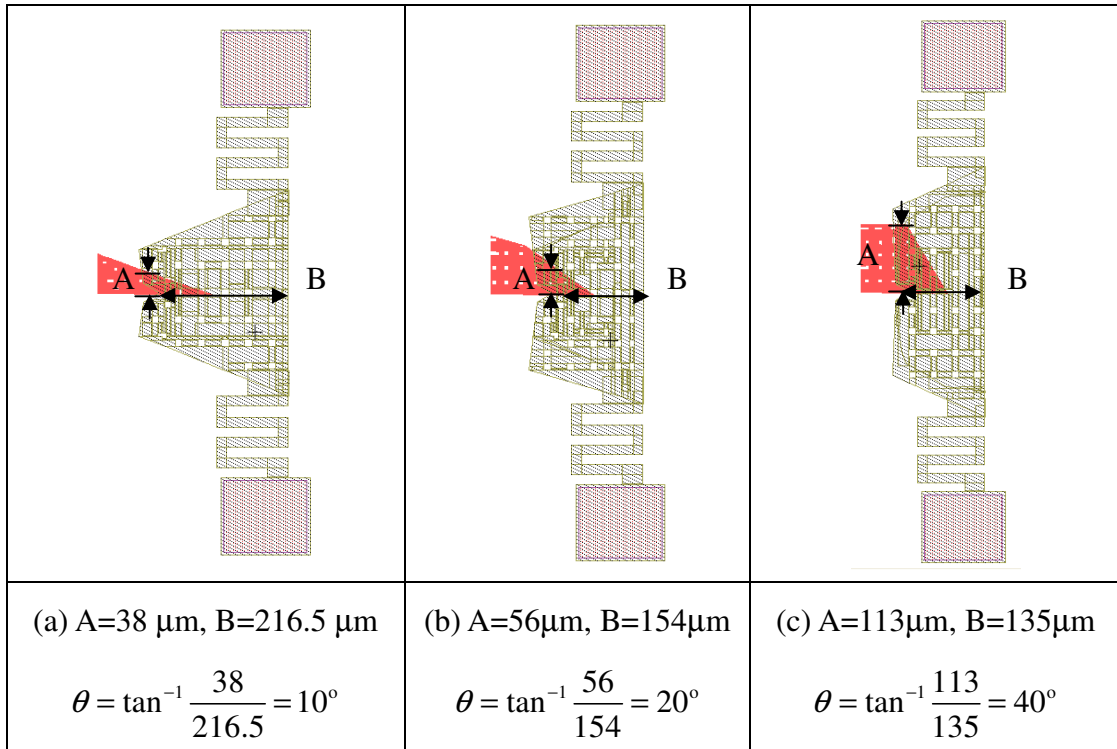


Figure 2-7 Different locking angles of the side latches.

2-2-4 Corner cube reflector

The corner cube reflector is composed of two 90° mirrors, as shown in Figure 2-8. The three reflecting surfaces are the front side of Mirror 1, back side of Mirror 2, and the surface of substrate underneath Mirror 2, as shown in Figure 2-8 (b). The reflecting zone is $(760 \mu\text{m})^3$.

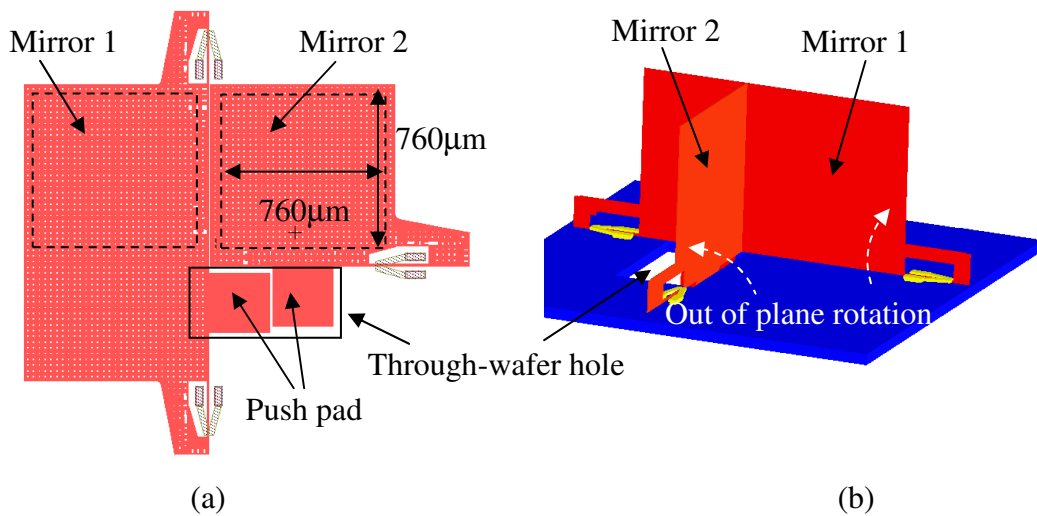


Figure 2-8 (a) Illustration of a corner cube reflector, (b) 3D schematic.

2-2-5 45° mirror design

In this section, two 45° structures are proposed. The difference between the two devices is that Device 1 utilizes SU-8 as the supporting structures and restoring force beams for the 45° SCS device, whereas Device 2 only utilizes the SCS layer on the SOI wafer to fabricate the structures.

2-2-5-1 Device 1

As shown in Figure 2-9, the 45° mirror consists of a mirror plate, V-shaped hinges, restoring force beams, and side supports. The mirror structure is in the SCS layer of the SOI wafer and the side supports are made of SU-8 photoresist. The rectangular SU-8 is attached to the side supports instead of the mirror plate.

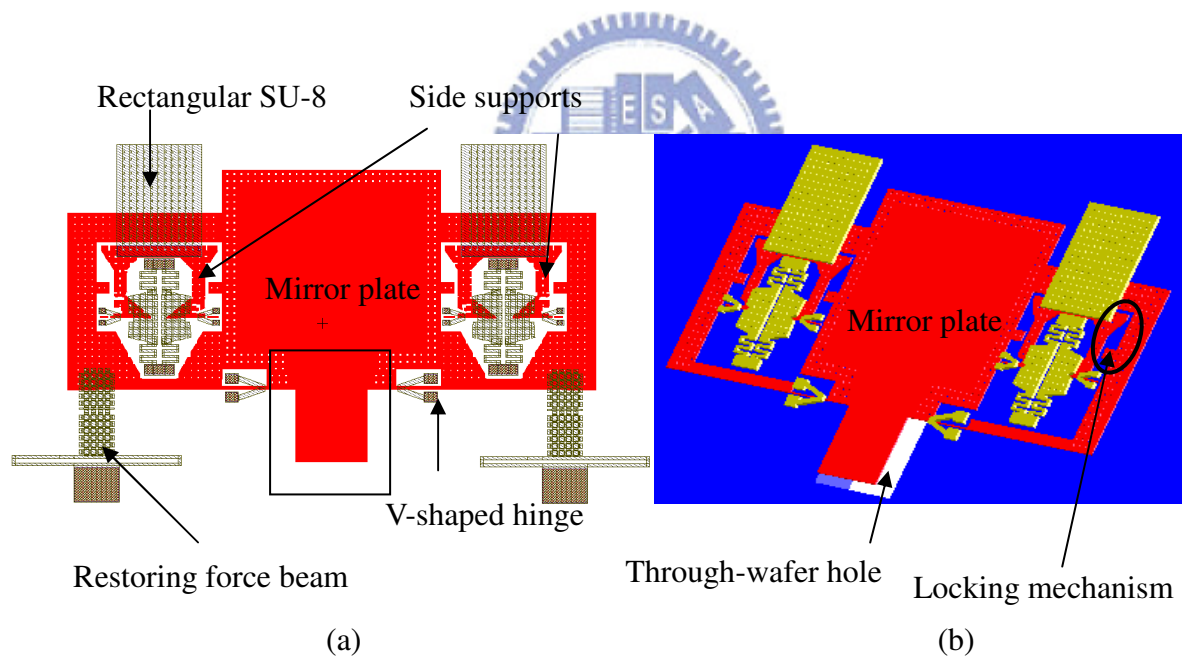


Figure 2-9 (a) Layout design of Device 1, (b) 3-D solid model.

The assembly procedure of device 1 is shown in Figure 2-10. First the microprobe is aligned to the push pad (Figure 2-10 (a)). Once the mirror rotates out of the plane when the probe pushes the pad, the mirror plate contacts the SU-8 layer. Then the

rectangular SU-8 attached on the side supports are pushed upward due to the upward force from the main mirror structure (Figure 2-10 (b)). As the side supports are pulled to 90°, it is locked at 90° by the side latches (Figure 2-10 (c)). Once the probe is removed, the mirror plate will lie back on the side supports due to the restoring force beams and fixed by the designed latches (Figure 2-10 (d)).

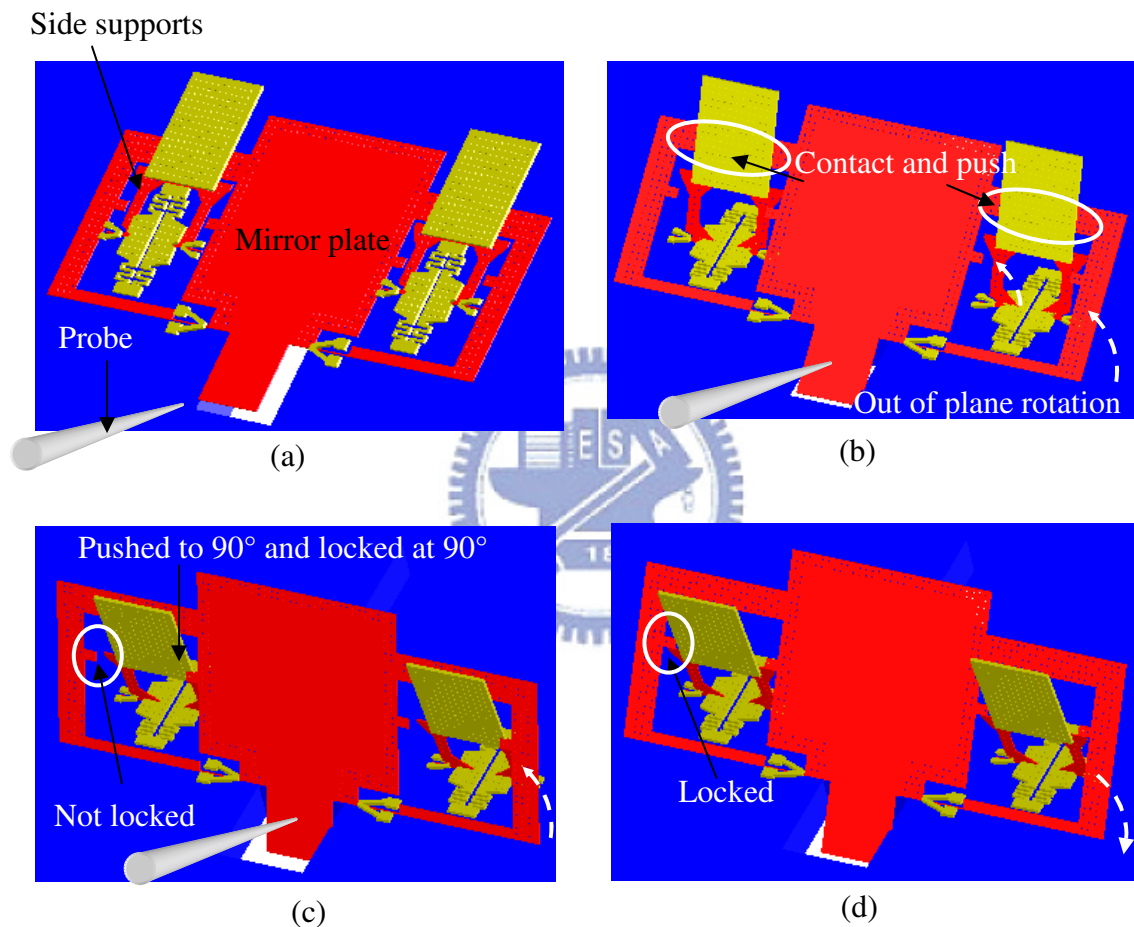


Figure 2-10 Assembly procedure of the device 1 with only one-push operation.

2-2-5-2 Device 2

In consideration of the complex structures in Device 1, Device 2 is designed without SU-8, but with only the SCS layer. However, two microprobes are needed in the push operation for this design. In Figure 2-11, the mirror and the support are in the

device layer of the SOI wafer, whereas the substrate provides the space for pushing. The layout and 3-D solid model are shown in Figure 2-10. Compared to Device 1, this design has a simplified structure. The mirror plate is $(760 \mu\text{m})^2$. The length of the support beam is $800 \mu\text{m}$ and the width is $120 \mu\text{m}$.

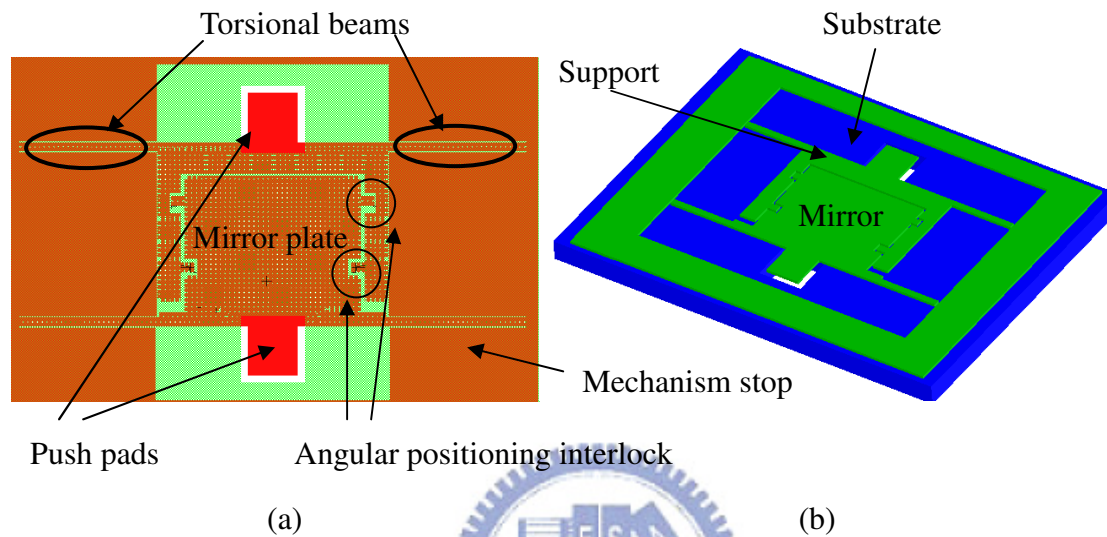


Figure 2-11 (a) Layout design of device 2, (b) 3-D model.

The assembly process of Device 2 is shown in Figure 2-12. First Probe 1 pushes the support to over 65° (Figure 2-12 (a)). Then Probe 2 pushes the mirror plate to $45^\circ\sim 55^\circ$ with Probe 1 held in position (Figure 2-12 (b)). Subsequently Probe 1 is removed and the torque from the torsional beams drives the support to lie on the mirror plate (Figure 2-12 (c)). After Probe 2 is removed, the downward force of the mirror plate also drives the mirror plate to lie on the support. Finally, the support and the mirror plate are interlocked (Figure 2-12 (d)).

Torsional beams

The torsional beams are used to provide restoring force. The design of the torsional beams is similar to [26]. For a 45° mirror, the twist angle of the torsional

beams is 45° . However, during the assembly process the support is needed to be twisted to over 80° . Thus the twist angle of 80° is adopted in this design. The torsional beam design is based on the torsion formula of a beam with a rectangular cross section [27],

$$\theta = \frac{\Gamma L}{KG}, \quad (2-2)$$

$$K = ab^3 \left[\frac{16}{3} - 3.36 \frac{b}{a} \left(1 - \frac{b^4}{12a^4} \right) \right], \quad (2-3)$$

$$\tau_{\max} = \frac{3\Gamma}{8ab^3} \left[1 + 0.6095 \frac{b}{a} + 0.8865 \left(\frac{b}{a} \right)^2 - 1.8023 \left(\frac{b}{a} \right)^3 + 0.9100 \left(\frac{b}{a} \right)^4 \right], \text{ for } a \geq b, \quad (2-4)$$

where θ is the angle of twist, Γ is twisting moment, L is beam length, K is a constant depending on the geometry of beam, G is shear modulus, τ_{\max} is the maximum shear stress at the midpoint of the longer side compared between a and b , a and b is half of the longer and shorter sides of the cross section of the beam, respectively (Figure 2-13).

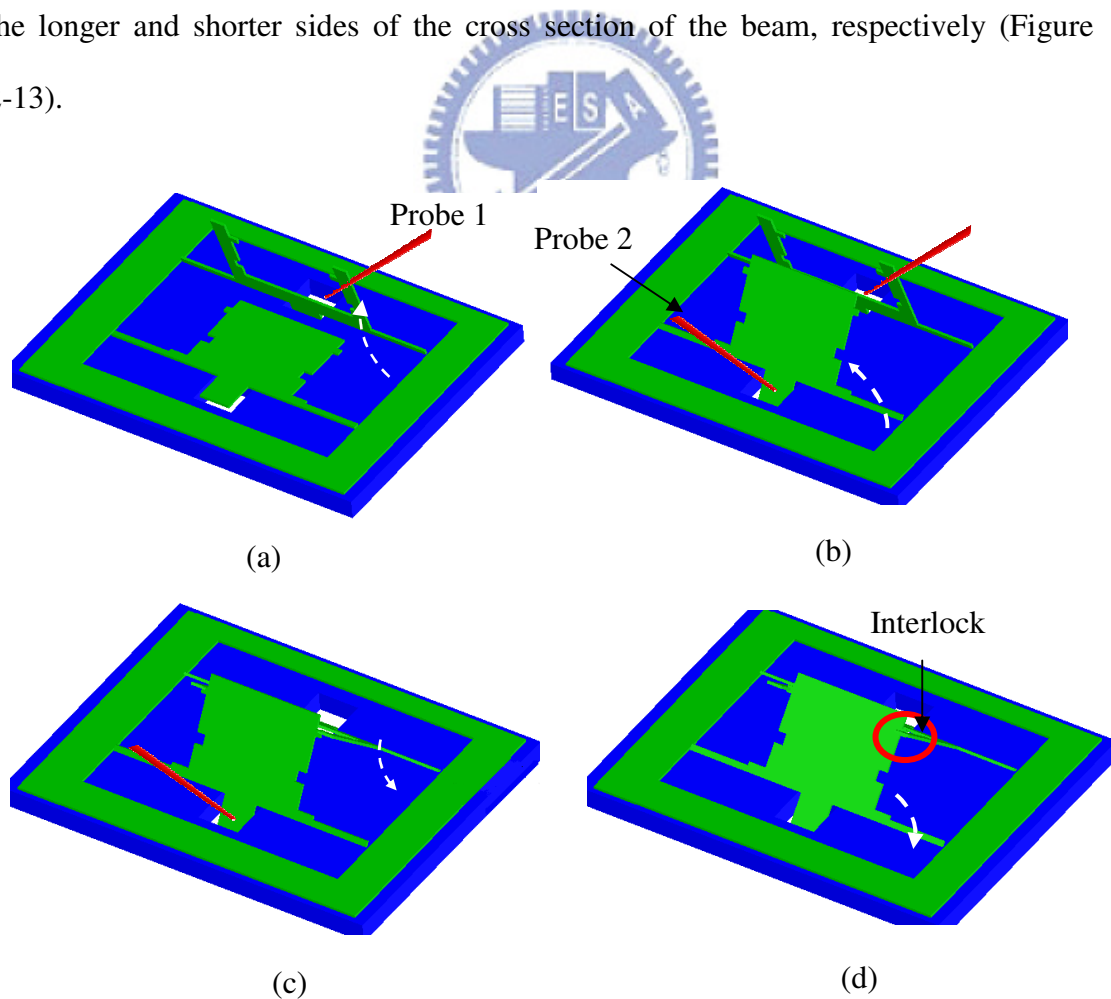


Figure 2-12 Assembly process of the device 2.

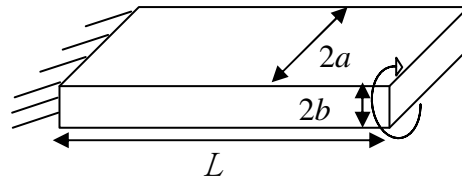
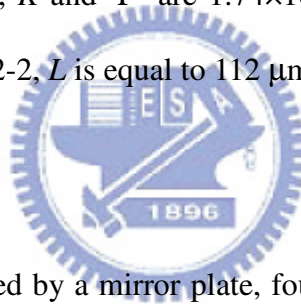


Figure 2-13 Form and dimensions of cross sections.

The device layer of the SOI wafer is $5\ \mu\text{m}$ and therefore a is $2.5\ \mu\text{m}$. The width of the beam is $45\ \mu\text{m}$ and therefore b is $22.5\ \mu\text{m}$. The shear modulus of single-crystal silicon is $79.9\ \text{GPa}$ [28] and the yield strength of single-crystal silicon is $7\ \text{GPa}$ [26]. The maximum shear stress (τ_{max}) in this structure when $\theta=80^\circ$ must be smaller than the yield strength and $\tau_{\text{max}} = 5\ \text{GPa}$ is used in the design. By substituting these values into Equations 2-2, 2-3, and 2-4, K and Γ are $1.74 \times 10^{-21}\ \text{m}^4$ and $1.74 \times 10^{-6}\ \text{N} \cdot \text{m}$, respectively. From the Equation 2-2, L is equal to $112\ \mu\text{m}$.



2-2-6 135° mirror design

The 135° mirror is constructed by a mirror plate, four restoring force beams, and two 90° supports, as shown in Figure 2-14. The fabrication process of the 135° structure is the same as Device 1 in the 45° design. Two push operations are needed in the assembly process. The 90° supports, which are similar to the 90° mirrors in [7], are first pushed up. Then the mirror plate is pushed to 135° and fixed on the two 90° supports by the downward force from the restoring force beams, as shown in Figure 2-14 (b).

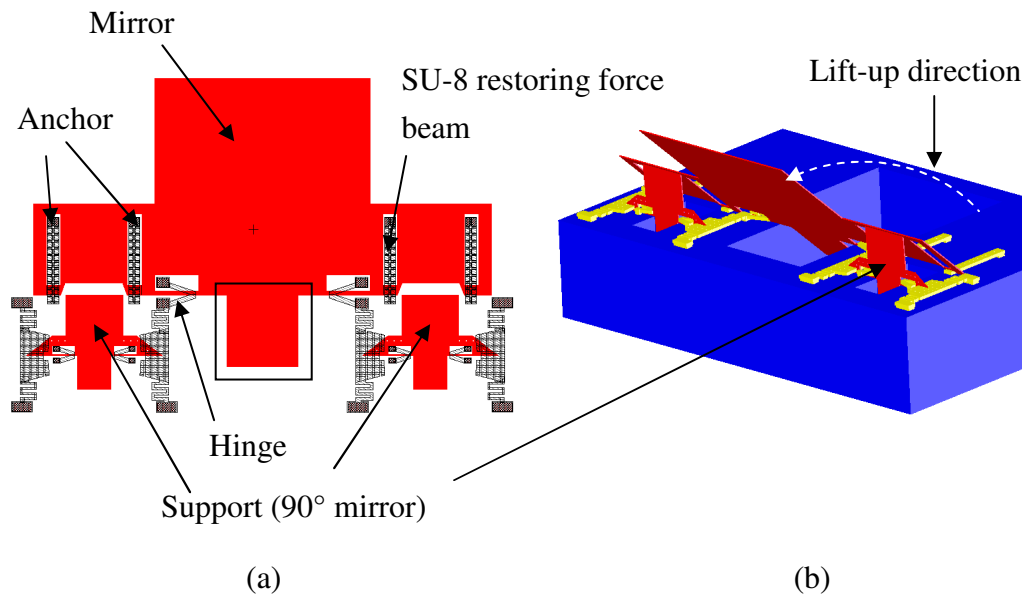


Figure 2-14 (a) Illustration of 135° structure, (b) 3D schematic.

2-3 Summary

Three mirrors and an array of microprobes are designed to demonstrate the batch assembly. Different locking angles of the side latches are used to test the positioning angular accuracy. Two 90° mirrors are used to construct a corner cube reflector. The 45° and 135° structures and their locking mechanisms are designed for its feasibility. In Chapter 3, the fabrication is discussed.

Chapter 3 Fabrication Process

In this chapter, a surface micromachining-like fabrication process is described. The SU-8 photoresist is used with silicon-on-insulator (SOI) wafers to simplify the process flow. The SOI wafer is chosen with its flat surface characteristic of single crystal silicon. Using SOI wafers can also reduce the complexity of the process. SU-8 photoresist is used as a structure layer. Compared to the use of polysilicon as the structure layer, SU-8 photoresist can reduce the process complexity. Another advantage of using SU-8 is that the process temperature is low, which is more compatible with IC processes. However, the Young's modulus of SU-8 is about 4 GPa, while that of polysilicon is about 160 GPa. Therefore the deformation of SU-8 is larger than polysilicon under the same stress. Therefore, SU-8 structures should be well designed for angular positioning, as discussed in Chapter 2. The process of integration of SOI wafer with SU-8 photoresist is described in the following. The fabrication parameters are listed and some issues are discussed.

3-1 Process flow

As described in Chapter 2, SU-8 photoresist is used as a structure layer for angular positioning in Device 1. Therefore, the fabrication process includes both SOI wafers and SU-8 photoresist. In contrast to Device 1, the device layer of the SOI wafer is used for angular positioning in Device 2. Consequently, the fabrication process is simpler in Device 2 without using SU-8 photoresist.

3-1-1 Device 1

The fabrication process of Device 1 is shown in Figure 3-1. The device was fabricated in the Nano Facility Center at National Chiao Tung University. The SOI wafers have a device layer of 5 μm , buried oxide layer of 2 μm , and handle layer of 400 μm .

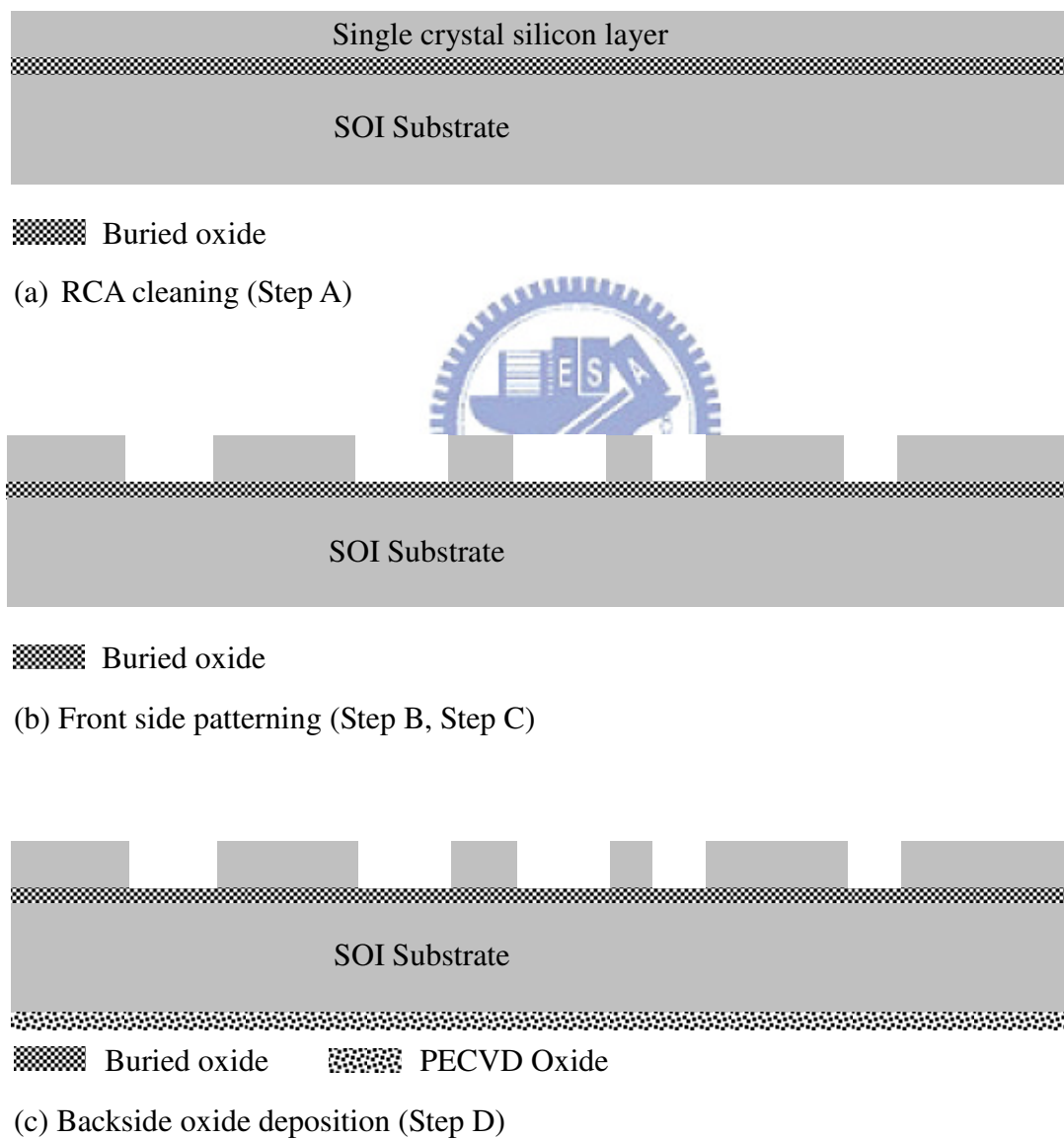
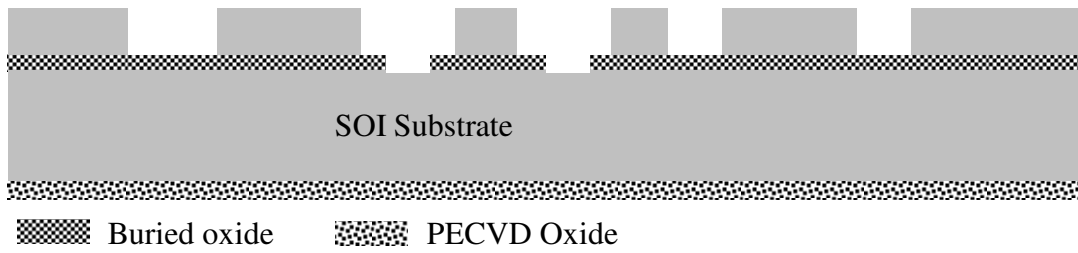
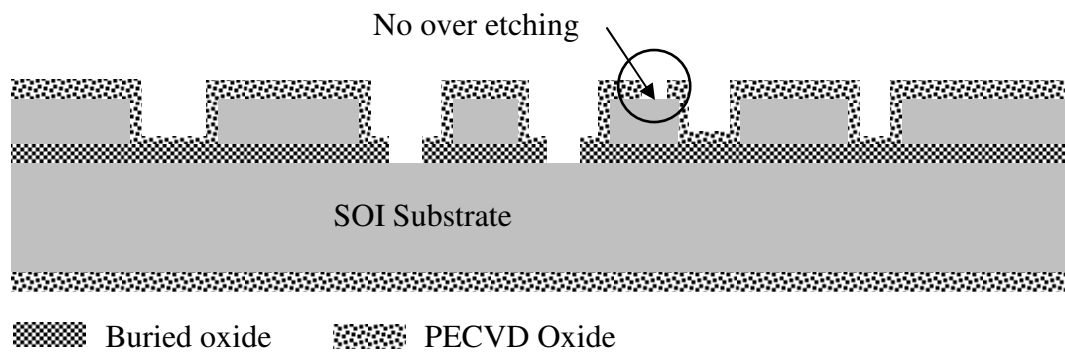


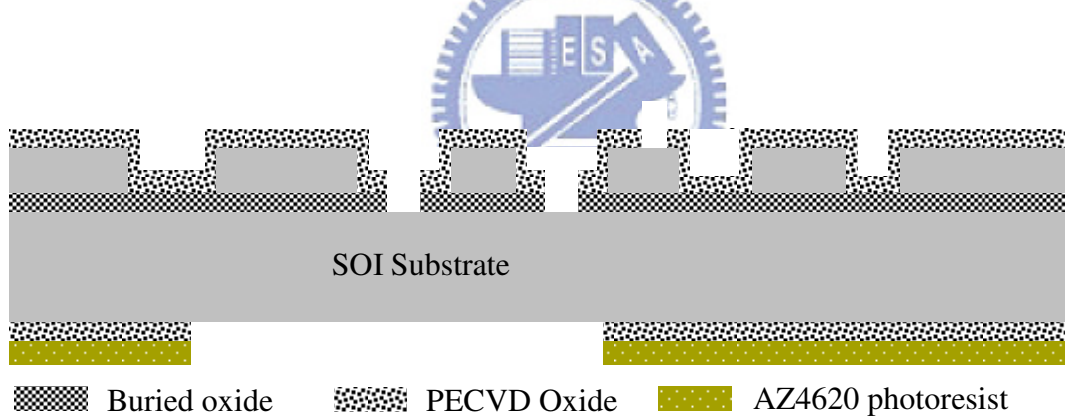
Figure 3-1 Fabrication process (Device 1).



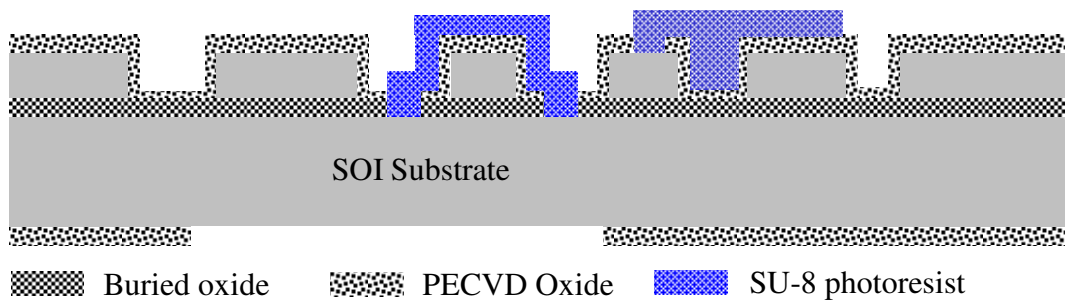
(d) Anchor definition (Step E, Step F)



(e) Oxide deposition, anchor patterning (Step G, Step H, Step I)

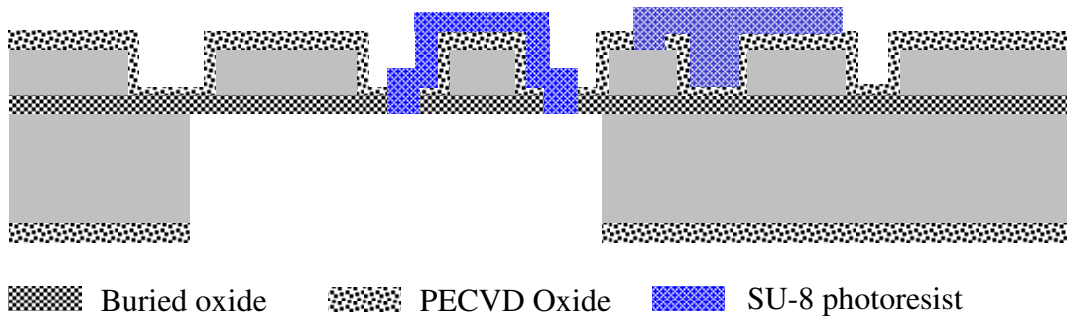


(f) Backside oxide definition (Step J, Step K)

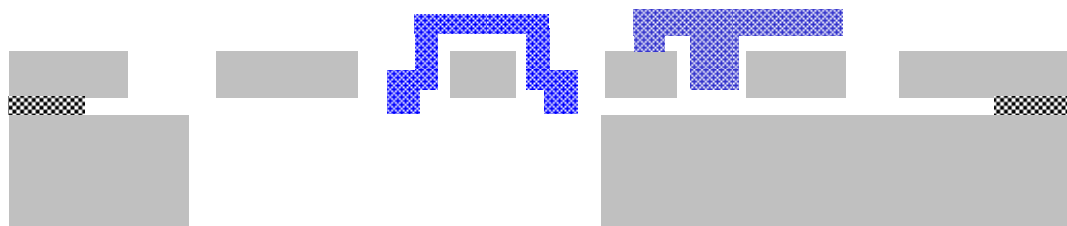


(g) SU-8 coating (Step L)

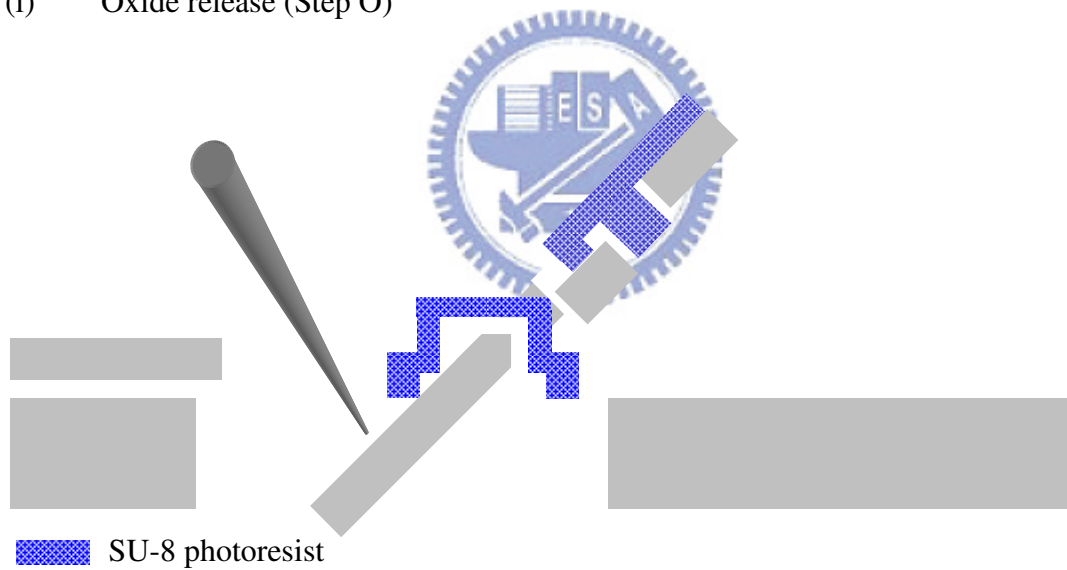
Figure 3-1 Fabrication process (Device 1) (continued).



(h) Backside ICP etching (Step N)



(i) Oxide release (Step O)



(j) Push (Step P)

Figure 3-1 Fabrication process (Device 1) (continued).

Step A: RCA cleaning

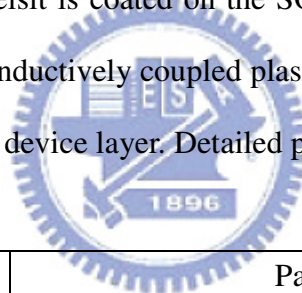
A standard RCA clean process was first performed on the bare SOI wafer. The process will remove the organic contaminants, the native oxide layer, and the ionic

contaminants. Detailed parameters are shown below. In consideration of the buried oxide in the SOI wafer, the chemical oxide removal process is reduced to 30 seconds. Between each step is de-ionized water rinse.

Step	Parameters
0	D. I. water Rinse (5 min)
1	$\text{H}_2\text{SO}_4 : \text{H}_2\text{O}_2 = 3 : 1$ (10~15 min, 75° C ~85 ° C)
2	$\text{HF} : \text{H}_2\text{O} = 1 : 100$ (30 sec, room temperature)
3	$\text{NH}_4\text{OH} : \text{H}_2\text{O}_2 : \text{H}_2\text{O} = 1 : 4 : 20$ (10~15 min, 75° C ~85 ° C)
4	$\text{HCL} : \text{H}_2\text{O}_2 : \text{H}_2\text{O} = 1 : 1 : 6$ (10~15 min 75° C ~85 ° C)
5	$\text{HF} : \text{H}_2\text{O} = 1 : 100$ (30 sec, room temperature)

Step B: Photolithography – Device layer definition (Mask1)

The FH6400 positive photoreisit is coated on the SOI wafer as the etching mask for defining the device layer by inductively coupled plasma (ICP). Mask 1 defines the main structure on the 5- μm -thick device layer. Detailed parameters are listed as below



Step	Description	Parameters
0	Photoresist	FH6400
1	HMDS coating	Vapor prime oven
2	Coating (spread cycle)	1000 rpm 10 sec
	Coating (spin cycle)	2000 rpm 35 sec
3	Soft bake	90° C hotplate 150 sec
4	Exposure	Karl Suss MJB-3 mask aligner (3.2 mW/cm ²) for 90 sec
5	Development	Developer FHD-5 for 55 sec
6	Rinse	D.I. water 1 min
7	Hard bake	120° C hotplate 30 min

Step C: Inductively coupled plasma silicon etching

Inductively coupled plasma (ICP) is used to etch the 5- μm -thick silicon device

layer with the mask defined in Step B. This process is performed by the ICP etching service of ITRC (Instrument Technology Research Center) and NTU (National Taiwan University). The parameters of the ICP etching at NTU (STS MESC multiplex ICP) are listed below.

Description	Etch phase parameters	Passivation phase parameters
Time per cycle	11.5 seconds	7.0 seconds
SF ₆ flow rate	130 sccm	0 sccm
C ₄ F ₈ flow rate	0 sccm	85 sccm
O ₂ flow rate	13 sccm	0 sccm
Coil RF power	600 W	600 W
Platen RF power	11.5 W	0 W
Process pressure	APC position = 81.2 % Base pressure = 0.3 mtorr	
Helium backside cooling	Helium backside pressure = 10 torr Maximum helium leak up rate = 20 mtorr/min	
Etch rate	0.6-0.7 μm per cycle depending on pattern	

Step D: Backside silicon oxide deposition

Silicon oxide is deposited by a BR-2000LL plasma enhanced chemical vapor deposition (PECVD) system on the backside of the handle layer. The deposited oxide layer with a thickness of 4.5 μm will be used as a hard mask for 400 μm ICP etching process. The thickness of the oxide layer is determined according to the 1:100 selectivity between the oxide and the silicon in the ICP process.

Description	Parameters
SiH ₄ flow rate	5 sccm
N ₂ O flow rate	90 sccm
Process pressure	400 mTorr
Process temperature	350° C
RF power	11 W
Deposition time	Two 35-minute deposition for 2.25 μm each

Step E: Photolithography – Anchor definition (Mask 2)

The anchor pattern is defined with Mask 2 in AZ4620 positive photoresist. The 2- μm -thick buried oxide layer of the SOI wafer is then etched by RIE. The selectivity between buried oxide and the AZ4620 photoresist is about 1:2 in the RIE process. Therefore, 5- μm -thick photoresist is coated in this step.

Step	Description	Parameters
0	Photoresist	AZ4620
1	HMDS coating	Vapor prime oven
2	Coating (spread cycle)	1000 rpm 10 sec
	Coating (spin cycle)	2500 rpm 30 sec
3	Soft bake	90° C hotplate 25 min
4	Exposure	Karl Suss MJB-3 mask aligner (3.2 mW/cm ²) for 350 sec
5	Development	Developer AZ-300 for 4 min 35 sec
6	Rinse	D.I. water 1 min
7	Hard bake	120° C hotplate 60 min

Step F: Polysilicon reactive ion etching (Poly-Si RIE) – Buried oxide etching

The buried oxide layer exposed in Step E is etched by RIE (SAMCO RIE-10N). The 2- μm -thick oxide in the anchor areas is removed in this step to ensure the contact and adhesion between the SU-8 and the silicon.

Description	Parameters
SF ₆ flow rate	30 sccm
CHF ₃ flow rate	10 sccm
Helium backside cooling	about 15 sccm
Process pressure	50 mtorr
RF power	100 W
Etch rate	20 min for 2 μm buried oxide

Step G: Front side silicon oxide deposition

The sacrificial oxide layer between the SU-8 and the silicon device layer of the SOI wafer is deposited on the front side in this step by PECVD. The buried oxide and the silicon oxide deposited in this step provide the hinge pin rotation space after releasing. The deposition thickness is 3 μm .

Description	Parameters
SiH ₄ flow rate	5 sccm
N ₂ O flow rate	90 sccm
Process pressure	400 mTorr
Process temperature	350° C
RF power	11 W
Deposition time	Two 23-minute deposition for 1.5 μm each

Step H: Photolithography – Anchor definition (Mask 3)

Similar to Step E, anchor is defined again in this step. The oxide deposited in the previous step will be etched in the next step with the pattern defined in this step. Since the selectivity between PECVD oxide and AZ4620 photoresist is about 1:1.7 in the RIE process, a 7- μm -thick photoresist of AZ4620 is coated on the wafer.

Step	Description	Parameters
0	Photoresist	AZ4620
1	HMDS coating	Vapor prime oven
2	Coating (spread cycle)	1000 rpm 10 sec
	Coating (spin cycle)	2000 rpm 30 sec
3	Soft bake	90° C hotplate 28 min
4	Exposure	Karl Suss MJB-3 mask aligner (3.2 mW/cm ²) for 350 sec
5	Development	Developer AZ-300 for 4 min 35 sec
6	Rinse	D.I. water 1 min
7	Hard bake	120° C hotplate 60 min

Step I: High density plasma reactive ion etching (HDP-RIE) – PECVD oxide etching

This step defines the contact between the silicon device layer and the SU-8 layer. About 3- μm -thick oxide deposited by PECVD is etched. To prevent etching of the silicon device layer, HDP-RIE is used for its good selectivity between the silicon and oxide in this step. Thus the 5- μm -thick silicon will not be etched, as marked in Figure 3-1 (e). The prolonged etching time can ensure the complete removal of the oxide on the silicon device layer and silicon substrate.

Description	Parameters
Ar flow rate	40 sccm
CHF ₃ flow rate	40 sccm
Helium backside cooling	Open
Process pressure	10 mtorr
ICP RF power	750W
Bias RF power	120 W
Etch rate	1 μm per 500 sec

Step J: Photolithography on backside silicon oxide (Mask 4)

The wafer through hole is defined in this step as the space for pushing. The oxide layer is deposited in Step D. This step patterns the oxide by AZ4620 photoresist. The patterned oxide will be used as the hard mask for etching the 400 μm silicon on the backside of the SOI wafer. An EV620 double side aligner at National Tsing Hua University (NCTU) is used for the photolithography process. About 8 μm photoresist is coated in this step.

Step	Description	Parameters
0	Photoresist	AZ4620
1	HMDS coating	Vapor prime oven
2	Coating (spread cycle)	1000 rpm 10 sec

	Coating (spin cycle)	2000 rpm 40 sec
3	Soft bake	90° C hotplate 27 min
4	Exposure	EV620 mask aligner (10 mW/cm ²) for 12 sec
5	Development	Developer for 1 min 15 sec
6	Rinse	D.I. water 1 min
7	Hard bake	120° C hotplate 60 min

Step K: Polysilicon reactive ion etching (Poly-Si RIE) – Backside oxide etching

The patterned 4.5 μm oxide is etched in this step. Over etching is also needed to ensure complete removal of the oxide on the silicon. The selectivity between the PECVD oxide and the AZ4620 photoresist is 1:1.8.

Description	Parameters
SF ₆ flow rate	30 sccm
CHF ₃ flow rate	10 sccm
Helium backside cooling	about 15 sccm
Process pressure	50 mtorr
RF power	100 W
Etch rate	18 min for 2 μm PECVD oxide

Step L: SU-8 photolithography (Mask 5) – SU-8 structure layer definition

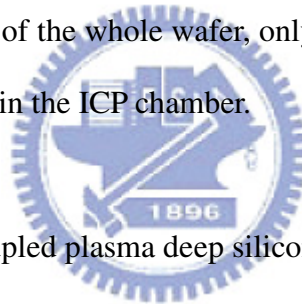
The 13- μm -thick SU-8 negative photoresist is deposited as a structure layer by Mask 5 in this step. This step is important for angular accuracy of the device. However the aligner used to fabricate the devices has a alignment accuracy of 2 μm , so the accuracy for the final device may be limited.

Step	Description	Parameters
0	Photoresist	SU-8 2010
1	Native oxide remove	BOE 10 sec (etching rate: 1000 $\text{\AA}/\text{min}$)
2	Pre-bake	150° C hotplate 20min
3	Coating (spread cycle)	500 rpm 10 sec

	Coating (spin cycle)	3000 rpm 30 sec
4	Pre-exposure bake	25° C to 65° C hotplate, 65° C for 1 min 65° C to 95° C hotplate, 95° C for 2 min 95° C to 25° C, rate: 1° C/min
5	Exposure	K-310P-100S mask aligner (35 mW/cm ²) for 4 sec
6	Post-exposure bake	25° C to 65° C hotplate, 65° C for 1 min 65° C to 95° C hotplate, 95° C for 2 min 95° C to 25° C (Rate: 1° C/min)
7	Development	SU-8 Developer for 3 min
8	Rinse	IPA 1 min
9	Hard bake	200° C hotplate for 30 min

Step M: Wafer dicing

The wafer is then diced into individual device chips. Since the subsequent ICP etching depth is nearly the depth of the whole wafer, only chips are used to reduce the risk of breaking the whole wafer in the ICP chamber.



Step N: Backside inductively coupled plasma deep silicon etching

The diced chips are bonded to a carrier wafer with thermal grease before the ICP etching. Thermal grease was used to cover all sides of the chip to prevent the front side of the chip from being etched by the plasma leaking through the uncovered gap between the chip and the carrier wafer. Oxide is deposited on the carrier wafer as the shield during ICP process. The 400- μ m-thick silicon substrate is then etched. The diced device bonded to the carrier wafer will change the helium cooling conditions and affect the vertical profile of the etched side wall. However, the etched through hole is only used for the next assembly process, so its vertical profile is not critical. Hence identical etching parameters as in Step C are used in this step. The process is done by the ICP etching service of ITRI and NTU.

Step O: Device release

The final step of the fabrication process is to etch the oxide layer to suspend the structure. This step is very important since the large mirror plate can easily stick to the substrate in conventional releasing process with HF solution. Vapor HF releasing is generally acknowledged as the method to solve the problem of stiction without using aqueous HF etching and DI water rinsing [29].

The parameters of the vapor HF releasing are shown in Table 3-1, and the schematic of the apparatus is shown in Figure 3-2. The apparatus consists of a light bulb, two polymer (such as polypropylene) cups, of which the inside one is hollow in the bottom, one polymer net, and one polymer cover. The components can be obtained with low cost. Before starting this step, the temperature is measured on the polymer net by a thermometer for 5 minutes, as shown in Figure 3-3. Since vapor HF etching has a rapid etching rate between 35° C and 40° C, hence the most important experimental parameter is the temperature on the chip. However, the temperature on the chip increases with the time during etching, so the initial temperature of etching is set at 35° C by adjusting the distance between the bulb and the chip in the setup (Figure 3-3).

Step P: Assembly

Finally, the released device is pushed by a microprobe.

Table 3-1 Parameters of vapor HF release

Description		Parameters
Light bulb		60 W
Distance	chip to HF vapor	1 cm
	light bulb to ground	10 cm
	chip to light bulb	5 cm
Initial temperature on the chip		35° C

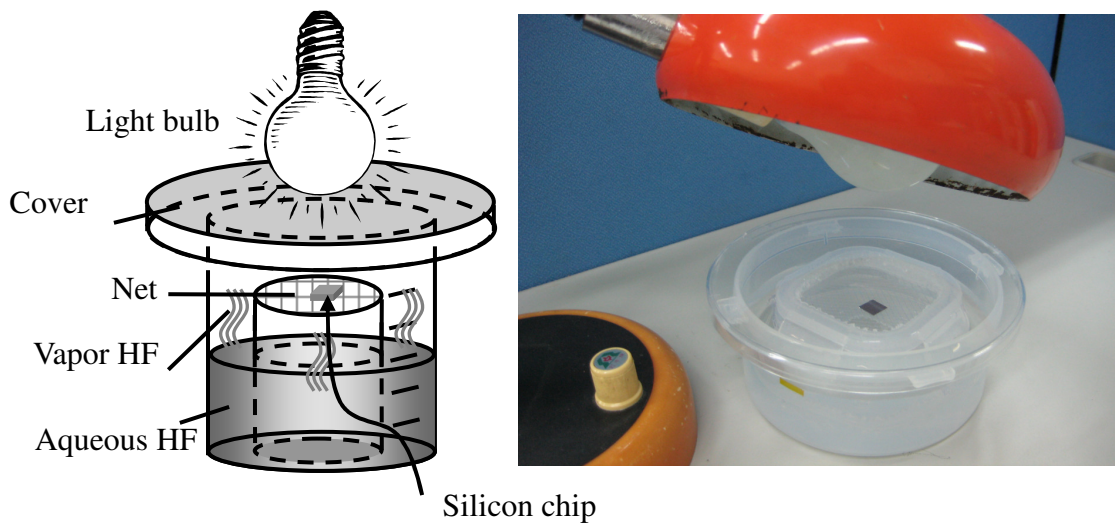


Figure 3-2 Schematic of the vapor HF release setup.

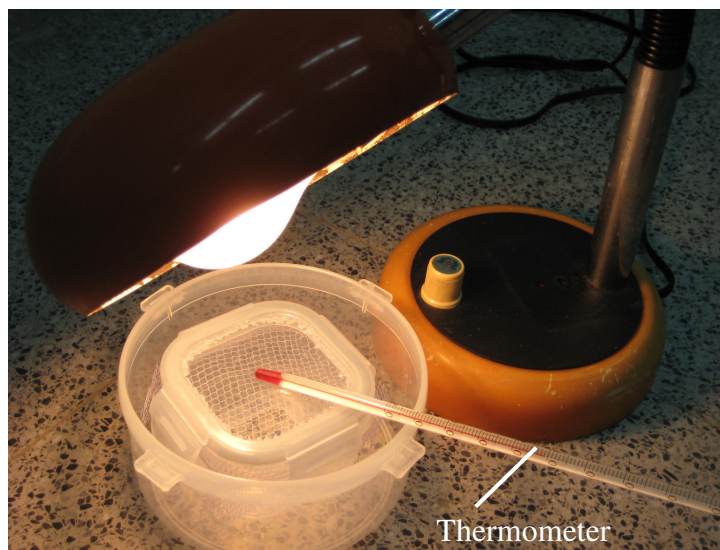


Figure 3-3 Temperature measurement before vapor HF release

3-1-2 Device 2

The fabrication process of Device 2 is simpler because the SU-8 photoresist is not used compared to Device 1. The process parameters are the same as for Device 1. The illustration is shown in Figure 3-4. Since SU-8 is not used in Device 2, anchor definition and SU-8 coating processes are not needed (Step E, F, G, H, I, L in Device 1).

Step A: RCA cleaning

(Step A in Device 1)

Step B: Photolithography – Device layer definition (Mask1)

(Step B in Device 1)

Step C: Inductively coupled plasma silicon etching – Silicon of device layer etching

(Step C in Device 1)

Step D: Backside silicon oxide deposition

(Step D in Device 1)

Step E: Photolithography process on backside silicon oxide (Mask 2)

(Step J in Device 1)

Step F: Polysilicon reactive ion etching (Poly-Si RIE) – Backside oxide etching

(Step K in Device 1)

Step G: Wafer dicing

(Step M in Device 1)



Step H: Backside inductively coupled plasma deep silicon etching

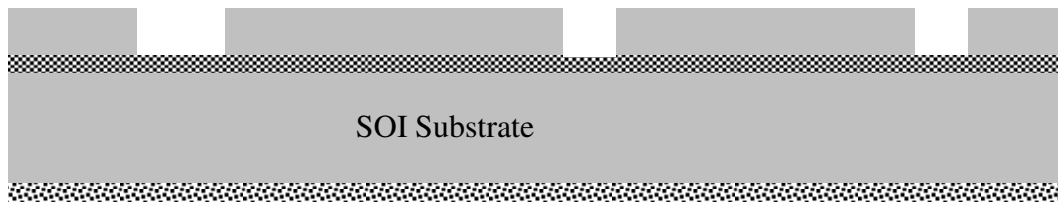
(Step N in Device 1)



Step I: Device release

(Step O in Device 1)

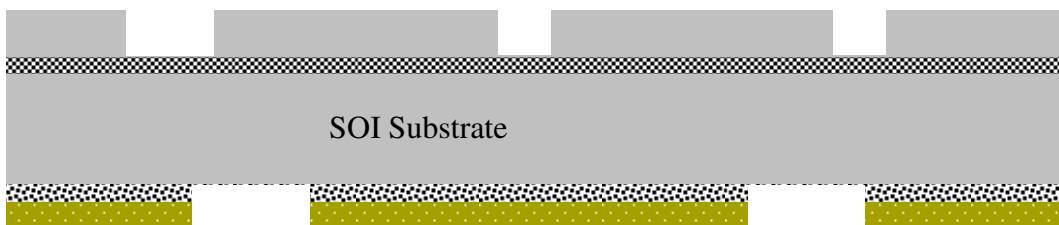
Step J: Assembly

(Step P in Device 1)



 Buried oxide
  PECVD Oxide

(a) Structure layer patterning and backside oxide deposition (Step A, Step B, Step C StepD)



 Buried oxide
  PECVD Oxide
  AZ4620 photoresist

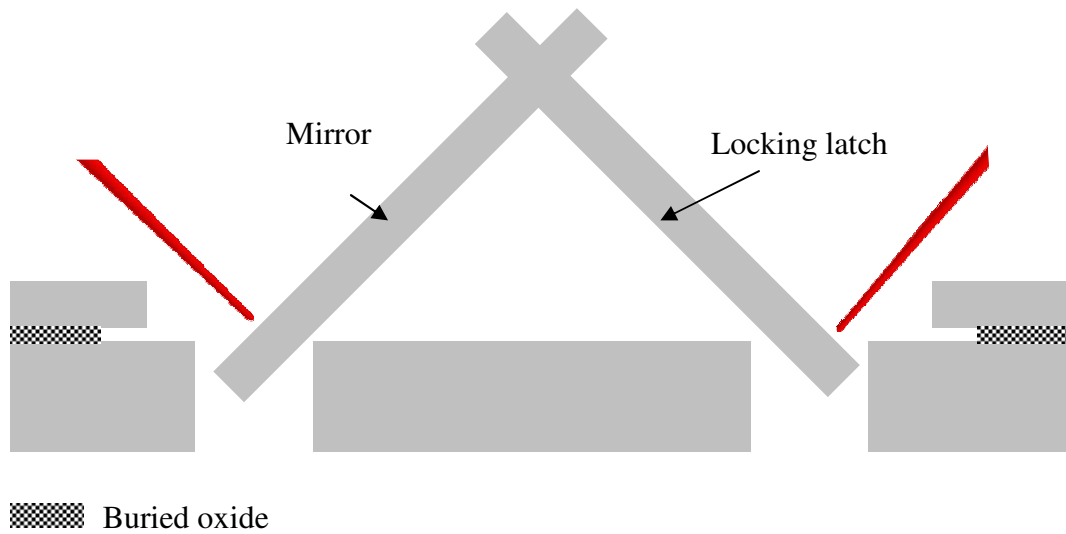
(b) Backside oxide definition (Step E, Step F)



 Buried oxide

(c) Backside ICP etching and oxide release (Step H, Step I)

Figure 3-4 Fabrication process (Device 2).



(d) Microprobe assembly (Step J)

Figure 3-4 Fabrication process (Device 2) (continued).

3-2 Fabrication issues and solutions

Adhesion and stiction problems were encountered in our previous study [7]. Adhesion problems between SU-8 and silicon were solved by immersing the wafer in the buffered oxide etchant (BOE) for 5 seconds before SU-8 coating to remove the native oxide. However, vapor HF releasing still resulted in stiction. These fabrication problems and their solutions are presented in this section.

3-2-1 Structure patterning

The ICP process provides a vertical etching for the structure layer. However, Poly-RIE can also be used to etch the 5- μm -thick silicon. A test was performed by using poly-RIE. Because the FH6400 photoresist was not thick enough as the etching mask for Poly-RIE, AZ4620 photoresist was used. In order to etch the 5- μm -thick silicon device layer, 5- μm -thick AZ4620 photoresist was needed with the etching selectivity of 1:1. Nevertheless, the shape of the AZ4620 photoresist would change after the long baking, as illustrated in Figure 3-5. As the structure layer, the vertical

side wall is very important for it will affect the angular accuracy after the structure is lifted up. The test showed that ICP is still a better solution for the structure patterning.

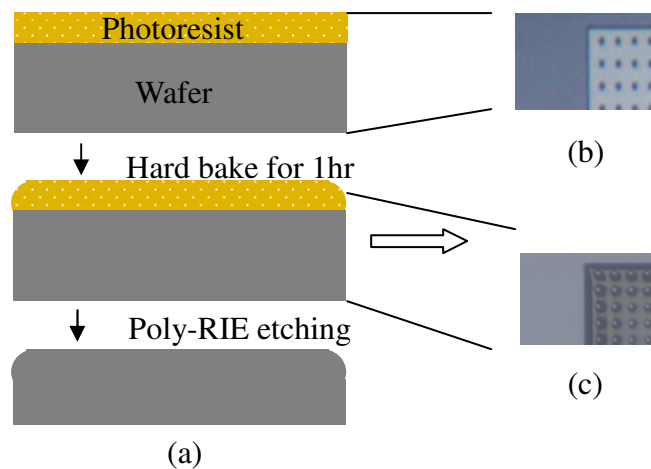


Figure 3-5 (a) Illustration of AZ4620 photoresist as the etching mask, (b) before baking, (c) after baking.

3-2-2 Oxide etching

In step I, the oxide was first etched by Poly-RIE in Device 1. However, it was difficult to control the etching parameters to obtain uniform etching across the entire wafer by Poly-RIE. The residual oxide will result in problems with SU-8 adhesion. Therefore, Poly-RIE was replaced by HDP-RIE, which has a better selectivity between oxide and silicon. Over etching was used to ensure complete removal of the oxide without etching the silicon device layer too much. In other words, process control could be improved by using HDP-RIE.

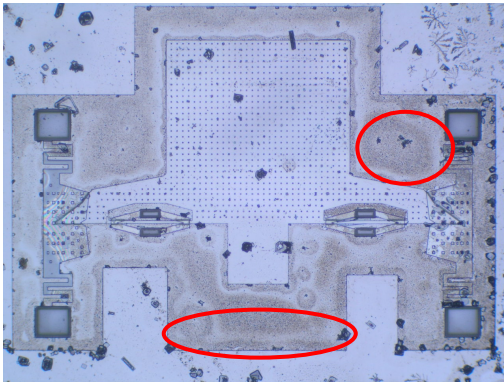
3-2-3 Vapor HF release

The most important step of the fabrication process is the release of the structure. Vapor HF is a common solution to reduce possibility of stiction. The most important parameter in this step is the temperature of the chip. Due to the variation of the ambient condition in the laboratory, the measurement of the temperature before the

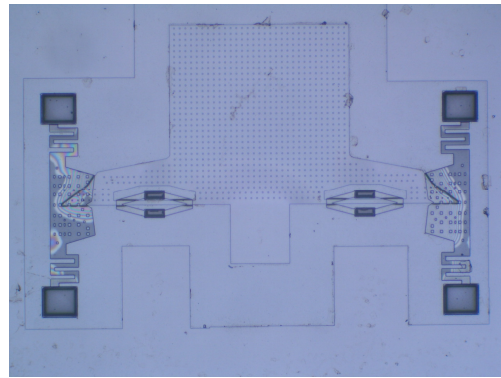
process was needed. Temperature over 35° C would not result in stiction. Temperature under 40° C would result in water stains on the chip, as Figure 3-6 shows. Temperature over 40° C would not result in any water stains but the etching rate was slow. Fortunately, the stains could be eliminated by baking for 5 minutes. Observation shows that the stains were much more easily produced in PECVD oxide etch than the buried oxide. Another notice is that the temperature of the chip was unstable at the beginning of the etch and the ambient mist would result in stiction. So the release process was divided into two steps and the parameters are shown in the following table. In Table 3-2, Step 2 was used for etching PECVD oxide and Step 5 was used for etching buried oxide. The baking in Step 3 to remove water stains from PECVD oxide etch could increase the etching rate in Step 5. The increased release time for the buried oxide etch could ensure complete removal of the sacrificial oxide in the structure. The temperature would increase continuously during the release process due to the heating by the light bulb before equilibrium was reached. The measured temperature was about 40° C after one hour. The increased release time would not damage the structure.

Table 3-2 Modified parameters of vapor HF release

Step	Description	Parameters
1	Temperature measurement	10 min (37° C ~40° C)
2	Release	40 minutes (PECVD oxide etching)
3	Hotplate baking	200° C, 5 min
4	Temperature measurement	10 min (37° C ~40° C)
5	Release	90 minutes (buried oxide etching)
6	Hotplate baking	200° C, 5 min



(a)



(b)

Figure 3-6 (a) Water stains on the chip after vapor HF etching, (b) after baking.



3-3 Summary

The fabrication processes and problems were presented. The parameters of vapor HF release were tuned to the best condition to avoid the problem of stiction. The ratio of stiction decreased from 40% to 5%. Some SEM photographs of the fabricated structures are showed in Figure 3-7. In the next chapter, the assembly procedure and assembled devices will be presented.

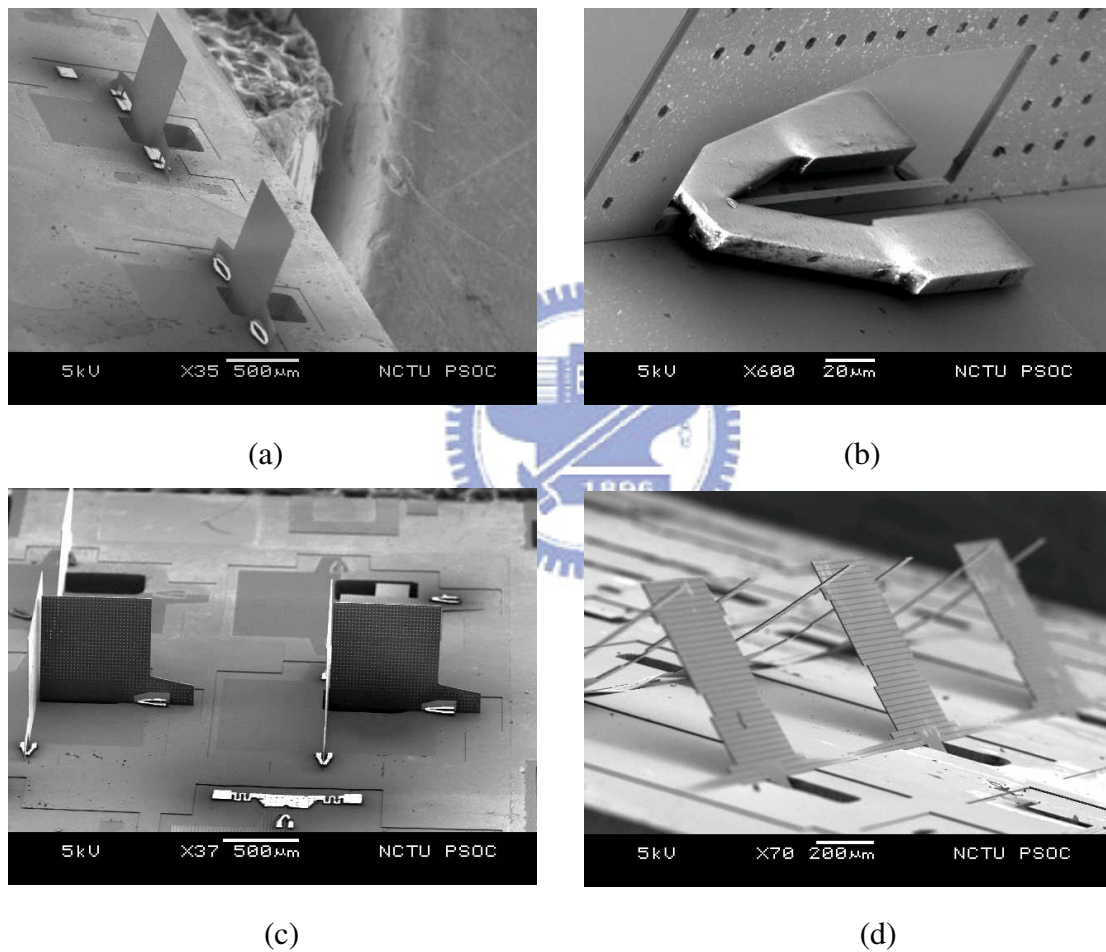


Figure 3-7 Fabricated devices, (a) 90° device without side latch, (b) close-up view of the V-shaped hinge, (c) corner cube reflectors, (d) 45° device.

Chapter 4 Measurement and Results

The fabrication and measurement results are presented in this chapter. The batch assembly of 90° devices is demonstrated, followed by the discussion of the angular deviation of the assembled devices. 90° devices fixed by V-shaped hinges only without traditional hinges are also tested. A corner cube reflector based on this concept is fabricated and tested. Finally, the positioning and angular accuracy of 45° devices are presented.

4-1 Batch assembly

Three microprobes were connected as an array by vacuum tape to push an array of 90° mirrors. The microprobe has a 10 μm diameter precision tip connected to a 4-cm-long shaft. The push pads are $250 \times 250 \mu\text{m}^2$ and mirror plates of $760 \times 760 \mu\text{m}^2$. The microprobe array was operated by a micropositioner, as shown in Figure 4-1. The distance of the microprobes was the same as the distance of the push pads, which was 2 mm.

The demonstration of batch assembly is shown in Figure 4-2. The different tip positions of the handmade microprobe array affected the respective assembly of each mirror. The problem can be easily solved by the make-to-order microprobes. After the microprobe array was pushed down, the middle mirror was first assembled (Figure 4-2 (b)). Then the other two mirrors were assembled successively as the pushing depth of the microprobes was increased (Figure 4-2 (c)(d)). After the microprobes were removed, the mirrors were assembled successfully (Figure (e)). The assembly time of three mirrors was 40s. Compared to 25s of a single mirror, the assembly time was reduced by 46%.

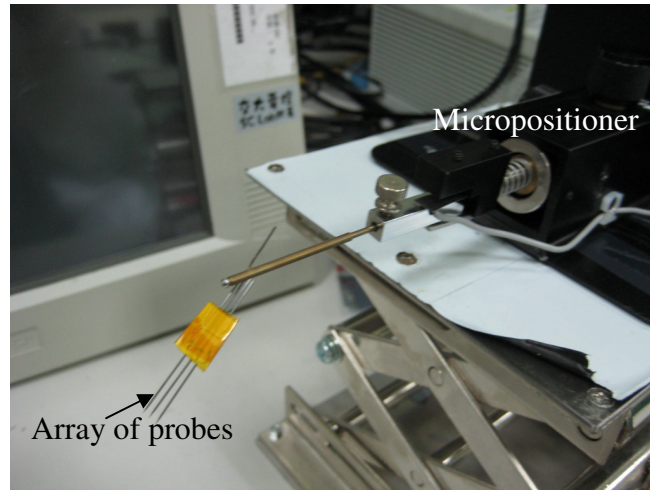


Figure 4-1 Setup for batch assembly.

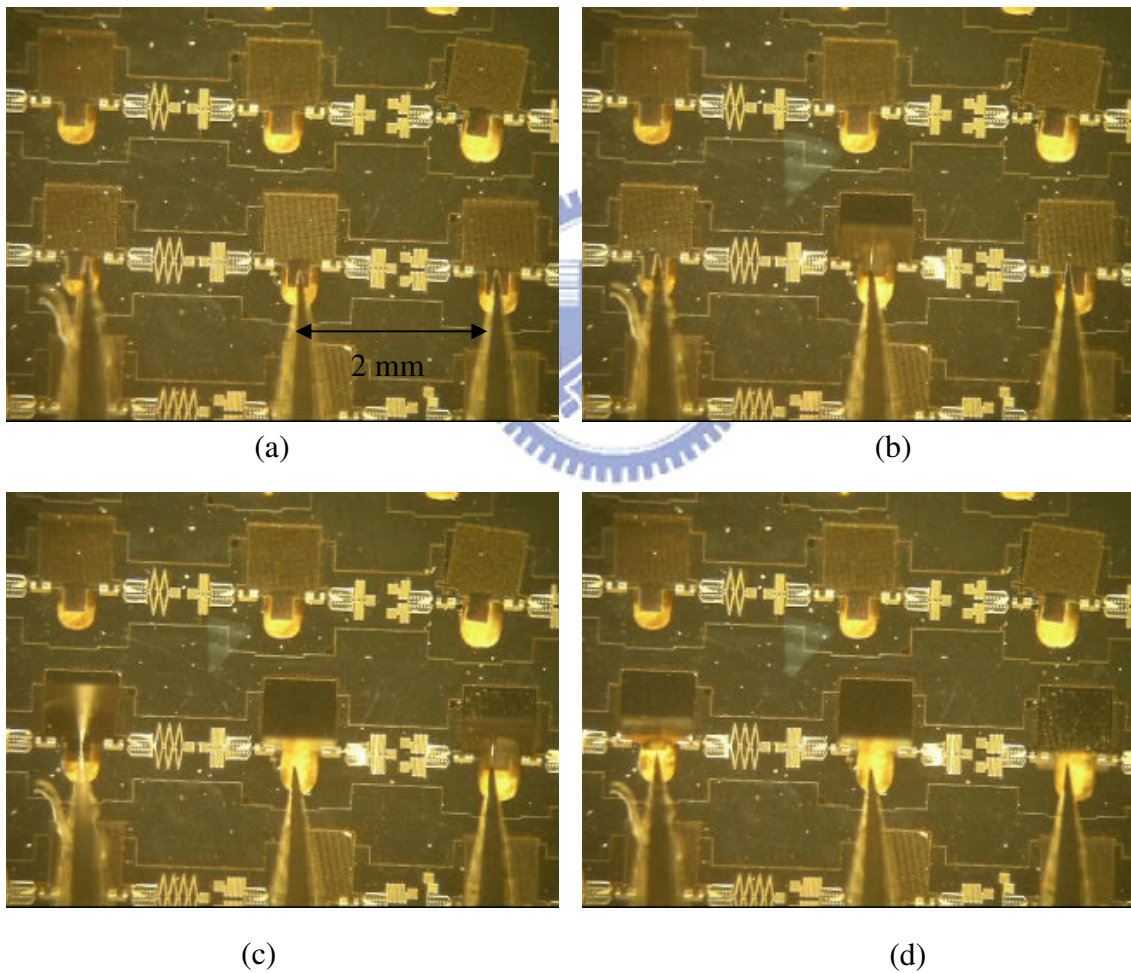


Figure 4-2 Sequence of batch assembly of three mirrors, (a) probes are aligned to the push pads, (b) the middle mirror was pushed up first, (c) other mirrors were assembled subsequently, (d) mirrors were assembled at 90°.

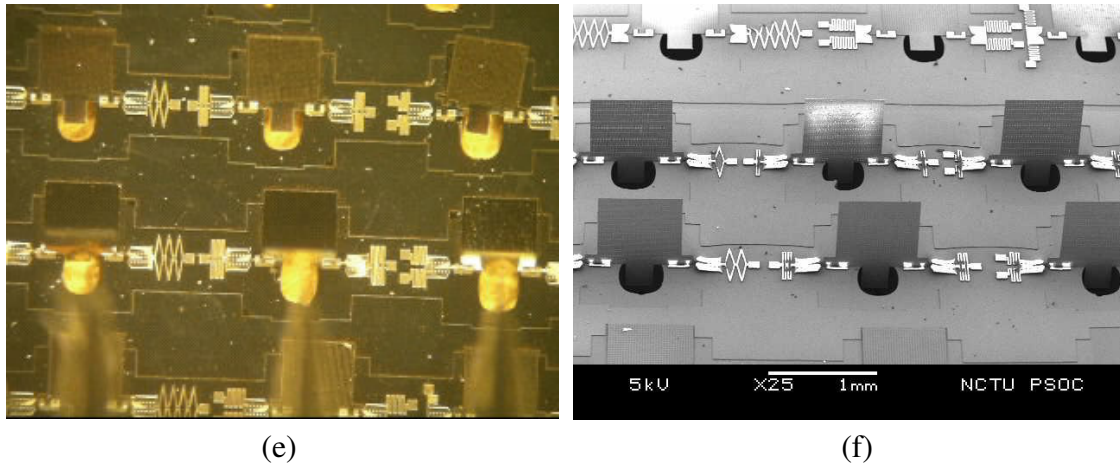


Figure 4-2 Sequence of batch assembly of three mirrors (continued), (e) the probes were moved away (f) SEM of assembled mirrors.

4-1-1 Problems

In the assembly process, the three mirrors and the three tips form two lines. If the two lines are not aligned to each other, batch assembly may fail. This is important for batch assembly on the wafer level. Figure 4-3 is an example of unsuccessful assembly of three mirrors. The right-hand side mirror was not assembled due to this problem (Figure 4-3 (d)). For batch assembly of three mirrors, 1° misalignment of the two lines results in $70\ \mu\text{m}$ deviation of the microprobes in x axis. Although the one push operation has large positioning tolerance due to the large push pad area ($250 \times 250\ \mu\text{m}^2$), the displacement due to the misalignment is magnified, especially for more than 3 mirrors.

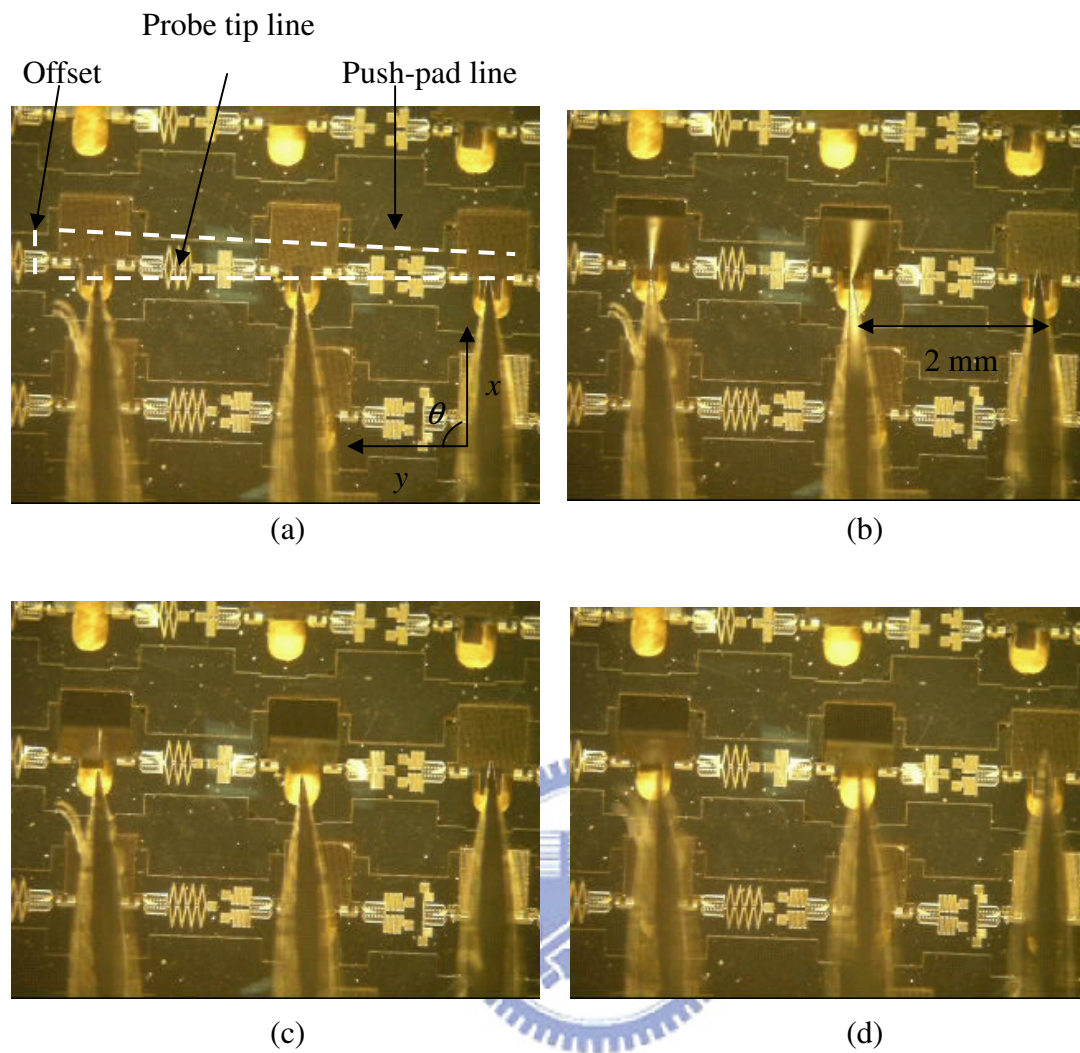


Figure 4-3 Sequence of a failed batch assembly, only two samples were pushed up.

4-2 Reflective coating

A reflective coating might be applied to the mirror. The residual stress in the coated metal will result in a curved mirror that will induce aberrations. Increasing the rigidity of the mirror by using a thicker mirror plate can solve the problem. An aluminum-coating experiment was conducted to measure the residual stress of aluminum, as shown in Figure 4-4.

If an isotropic stress is assumed and the thickness of the film is much smaller than that of the substrate, the stress can be expressed as [30],

$$\sigma = \frac{E_s \cdot d_s^2 \cdot \Delta\delta}{3r^2(1-\nu_s)d_f} \quad (4-1)$$

where σ is the intrinsic compressive stress, $\Delta\delta$ is difference in bowing of the substrate before and after, r is the radius of the substrate, E_s is the Young's Modulus of the substrate, ν_s is the Poisson's ratio of the substrate, d_s and d_f are the thickness of the substrate and the film, respectively. In Figure 4-4 (b), the aluminum is 1000 Å thick. The radius of the substrate is 760 μm. The result shows that the residual stress of aluminum is compressive. The intrinsic compressive stress can be calculated as 0.68×10^8 Pa, which is comparable to the value 1.5×10^8 Pa in literature [31]. By substituting the stress into Equation 4-1, the thickness of the SOI device layer should be increased to 50 μm so that the bowing is small than $\lambda/10 = 0.043 \mu\text{m}$

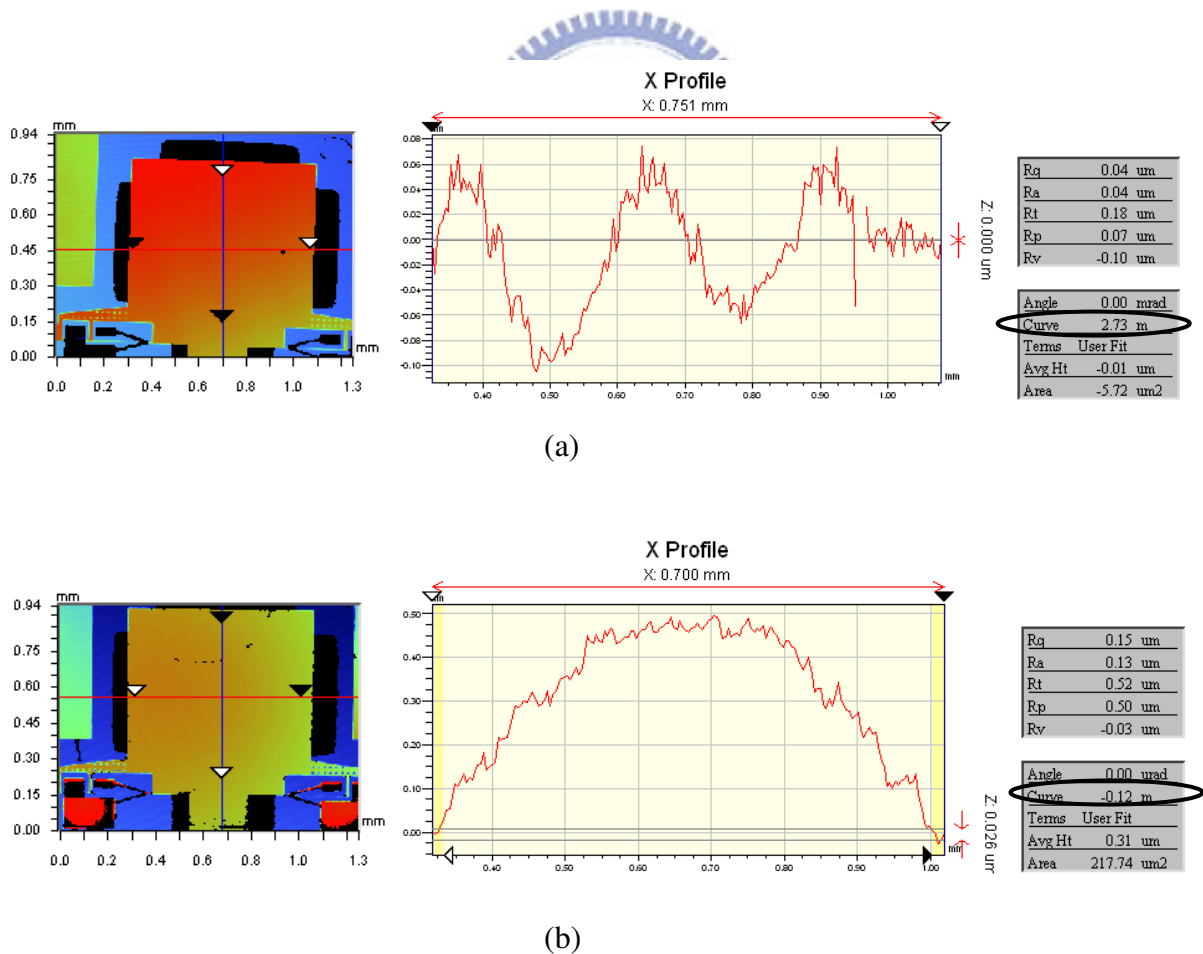


Figure 4-4 (a) Mirror before coating (b) mirror after coating.

4-3 V-shaped hinge

Positioning accuracy of the conventional and the V-shaped hinges are compared. As shown in Figure 4-5 (a), the hinge pin of the conventional hinge is at the center of the rotational axis. Figures 4-5 (b) and (c) show the right and left sides of the hinge pin after assembly. The two gaps should be both 10 μm if the hinge pin is at the center of the rotational axis. In Figures 4-5 (b) and (c), the gaps are about 13 μm and 7 μm , respectively. About 3 μm offset of the hinge pin position was measured.

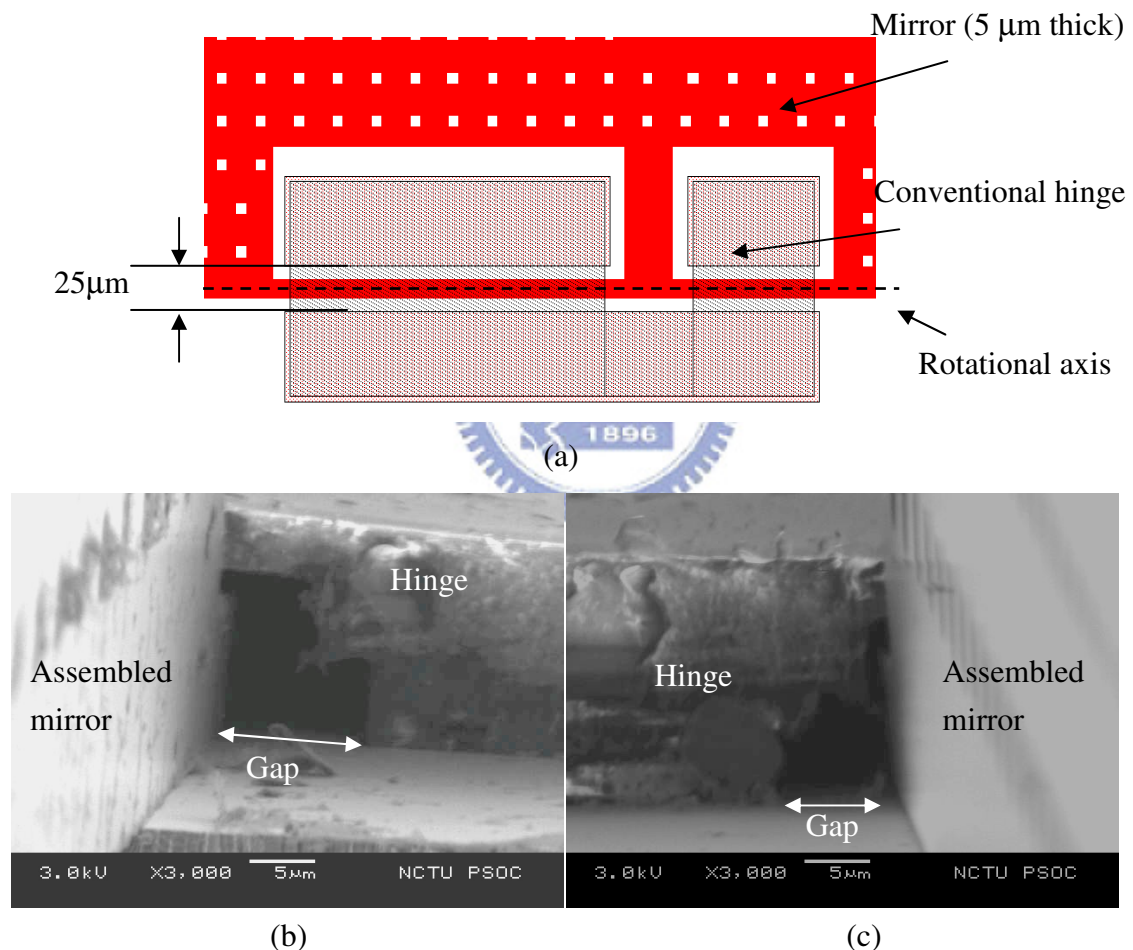


Figure 4-5 (a) Layout of the conventional hinge, (b) right side, (c) left side.

Compared to the conventional hinge, the SEM photographs in Figure 4-6 show the locking accuracy of the V-shaped hinge. In Figure 4-6 (a), the distances from the rotational axis to the two sides of the hinge pin are 2.5 μm and 8.5 μm , respectively.

Since the thickness of silicon is 5 μm , the distance between the hinge pin and the two sides of the SU-8 should be 0 μm (Gap 1) and 6 μm (Gap 2), respectively, after assembly. In Figure 4-6 (c), Gap 2 is broader than the 5- μm -thick hinge pin. Thus the axis deviation is less than 1 μm in the V-shaped hinge.

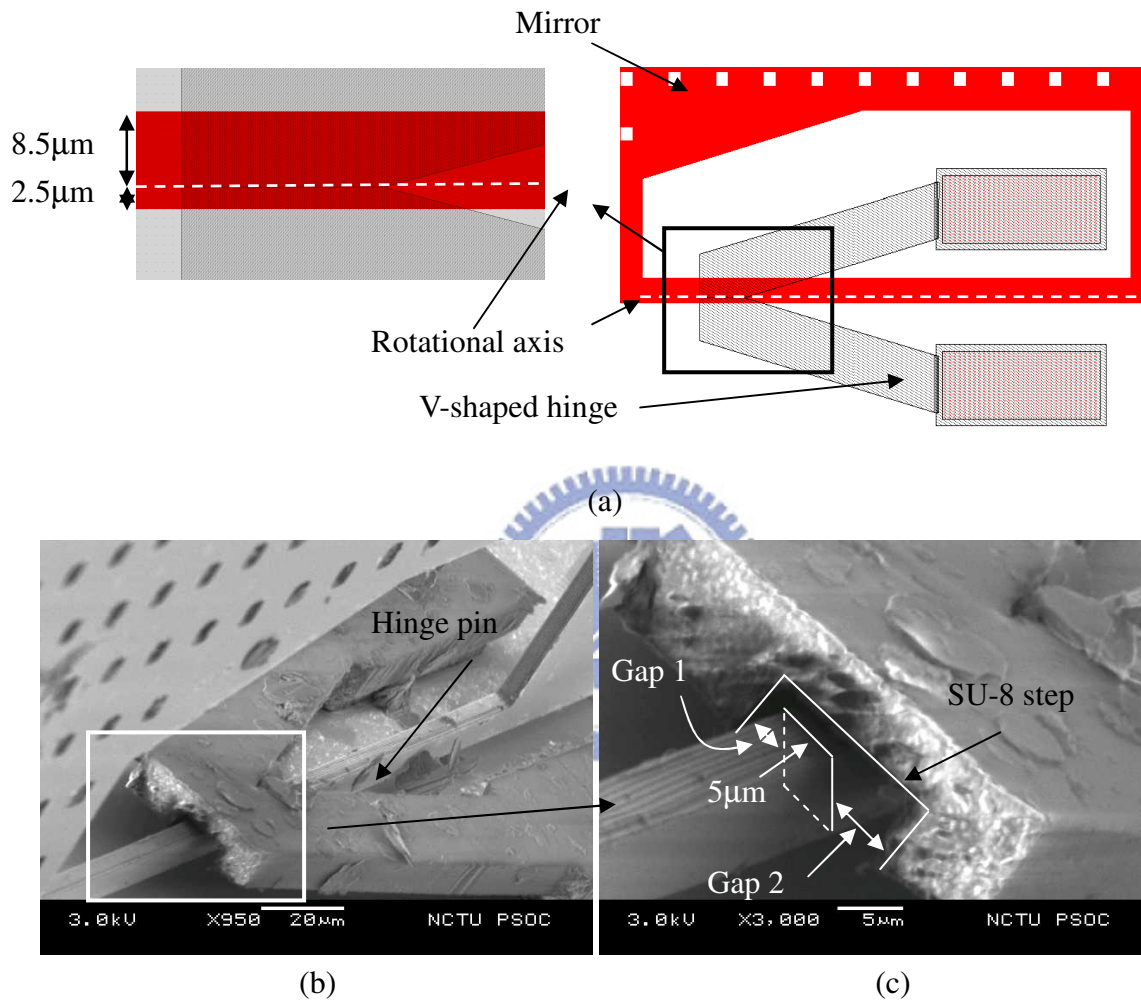


Figure 4-6 (a) Layout of the V-shaped hinge, (b) SEM photograph of the V-shaped hinge, (c) zoom in of the V-shaped hinge.

4-3-1 Strength of the V-shaped hinge

The assembled 90° mirror without side latches but with only V-shaped hinge is shown in Figure 4-7 (a). Figures 4-7 (b) and (c) show the SEM of the same sample taken in two different measurements. The mirror was measured at different angles because it was affected by the air flow of the pumping procedure in SEM. Although the V-shaped hinge can position the axis more precisely than the conventional hinge, the robustness of the assembled devices still needs to be improved.

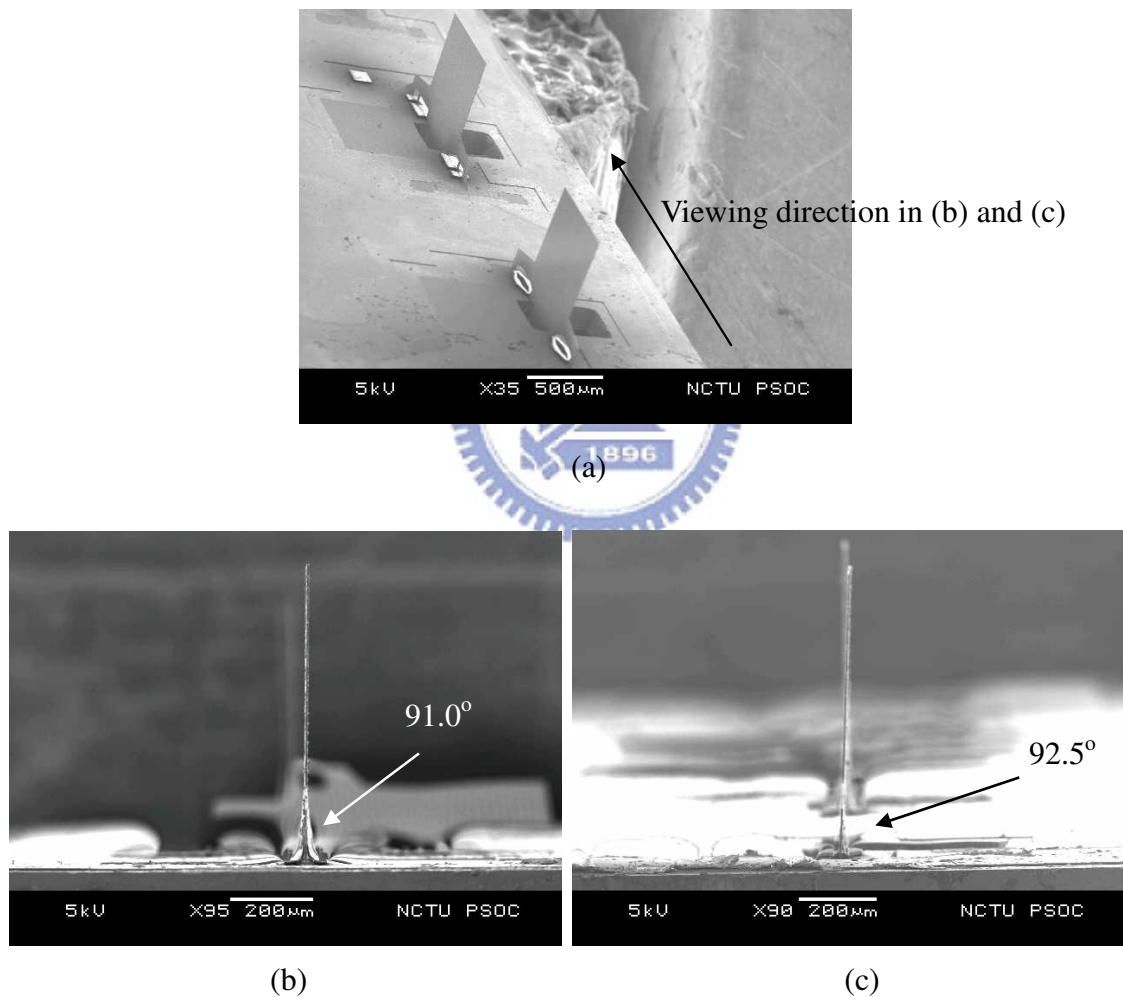


Figure 4-7 (a) SEM photograph of 90° mirror without side latch, (b) and (c) the same sample taken at two measurements.

4-4 Angular accuracy of 90° mirrors

The causes for angular inaccuracy are discussed in the following. The possible causes are listed and their effects are discussed.

Step in the SU-8 photoresist

Because the oxide deposition process in Step G is not a planar process, a step is formed in the bottom of the SU-8 photoresist and structure that affects mirror angle after assembly, as shown in Figure 4-8. Figure 4-8 (a) shows the layout design. Figure 4-8 (b) shows the cross section of the SU-8 step after assembly. Since the step locked the mirror at the rotational axis, the angles of the assembled devices are all less than 90° [7].

The step can be removed by polishing after the oxide deposition process. Another easy solution of this problem is to change the location of the step in the layout design, as shown in Figure 4-9. Because the mirror plate is not anchored after releasing, the offset of the SU-8 layer is not related to the angle of the flip-up mirror. The offset of the SU-8 layer can change the location of the SU-8 step. The separation between the locking point of the V-shaped side latch and the SU-8 step can solve the problem.

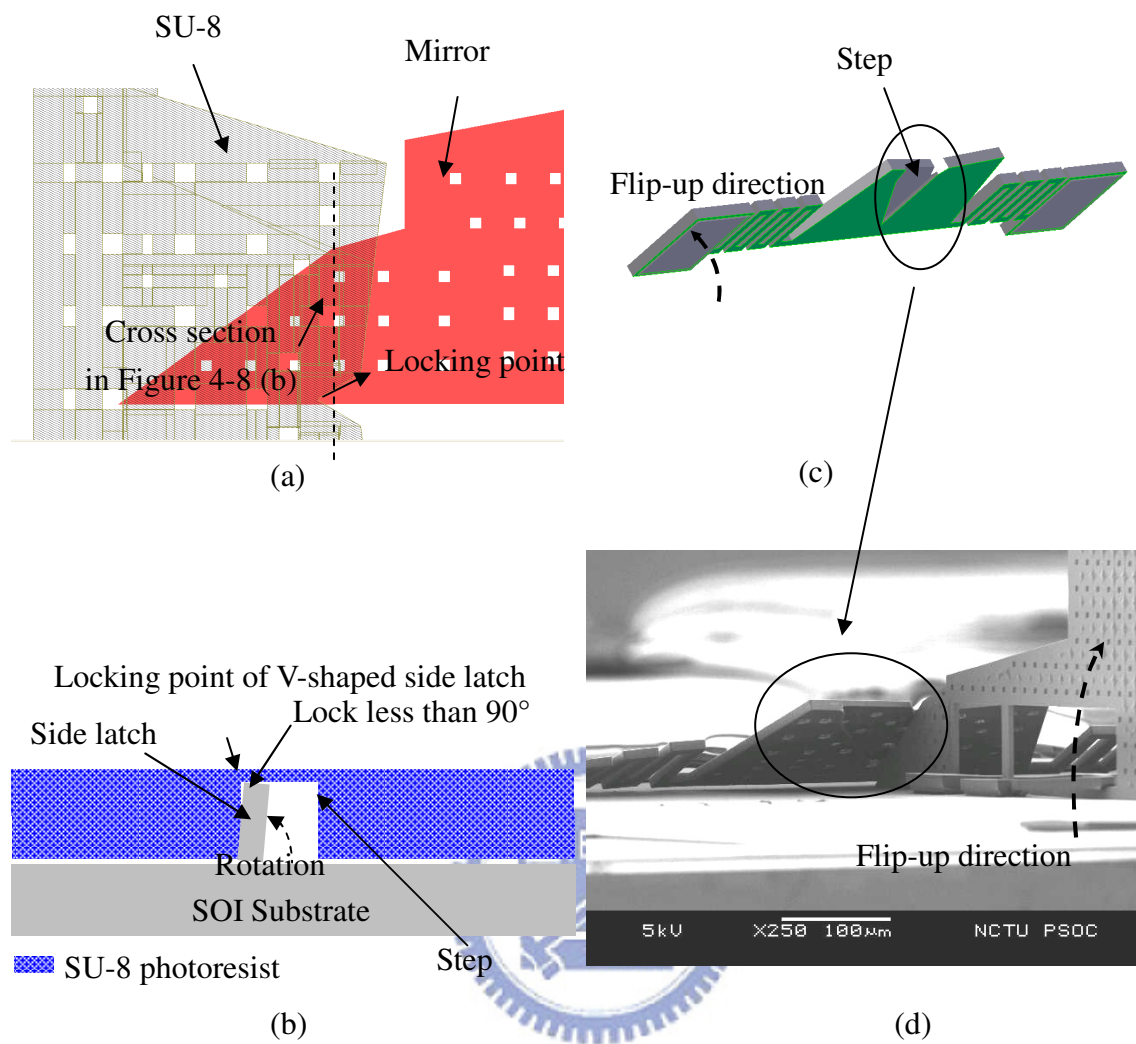


Figure 4-8 Step in the SU-8 photoresist, (a) layout design (b) cross section, (c) schematic, (d) SEM photograph of the SU-8 step [7].

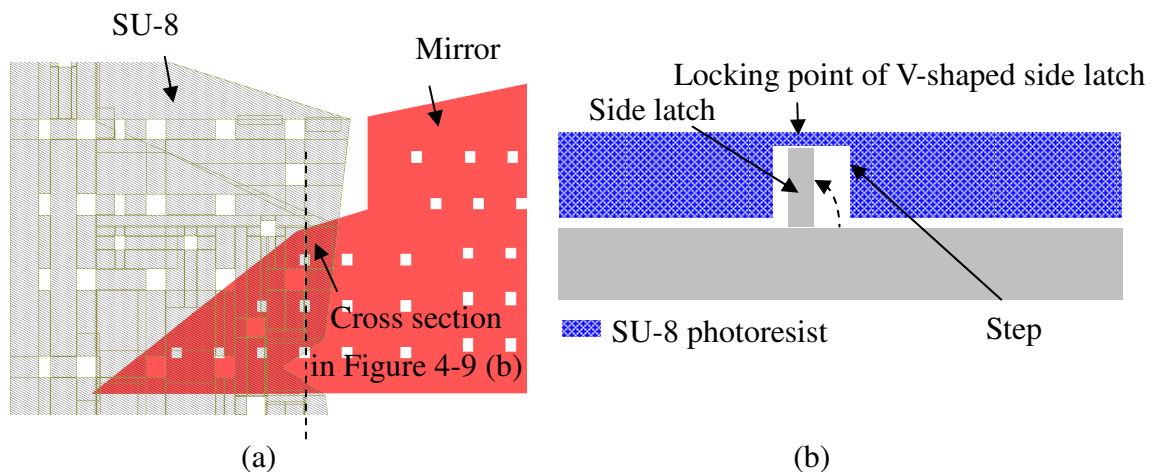


Figure 4-9 Changing the SU8 step position, (a) layout design, (b) cross section.

Side latches

Another reason that results in angular deviation is the side latches. As Figure 4-10 shows, the mirror plate was not locked into the center of the V-shaped opening. The main reasons are the spring and the friction force between the silicon and the SU-8 photoresist. The lifted-up angle of the side latches affects the angular accuracy. Figure 4-11 shows the SEM of different angles of the flip-up side latches and Figure 4-12 shows the statistics of the comparison. The angles were calculated by measuring the offset of the top of the mirror compared to the bottom using the ruler in an optical microscope. The magnification of the object lens and the eyepiece are 50 and 10, respectively. The resolution of the ruler is 1 mm. Thus the measurement resolution is $\frac{1 \text{ mm}}{50 \times 10} = 2 \mu\text{m}$. The height of the mirror is $760 \mu\text{m}$. Thus the angle resolution is $\sin^{-1} \frac{2 \mu\text{m}}{760 \mu\text{m}} = 0.15^\circ$. The sample was held on the microscope stage by a vacuum pump. In Figure 4-12, the structures are fabricated at average $89.8 \pm 0.3^\circ$, $89.7 \pm 0.4^\circ$, and $89.4 \pm 0.4^\circ$, which are 10° , 20° , and 40° structures, respectively. The angles of the mirrors with 10° side latches are more exact than that with 20° and 40° side latches. The reason was that the friction force of the 20° and 40° devices was greater than the 10° devices, as describe in Chapter 2. The restoring force of the side latches parallel to the x direction can not drive the mirror to the desired locking position effectively.

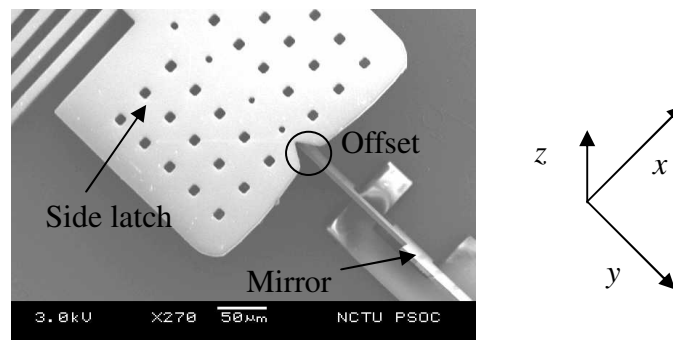


Figure 4-10 Offset of the mirror plate.

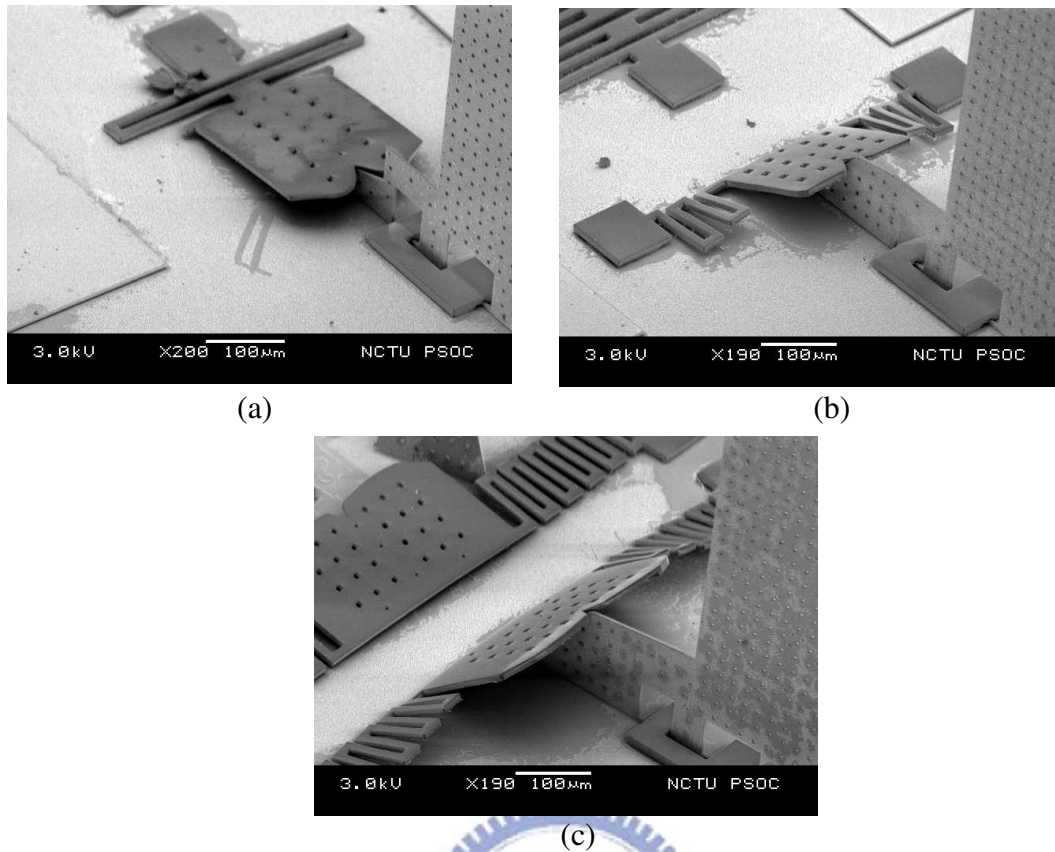


Figure 4-11 Side latches with different flip-up angles, (a) 10°, (b) 20°, (c) 40°.

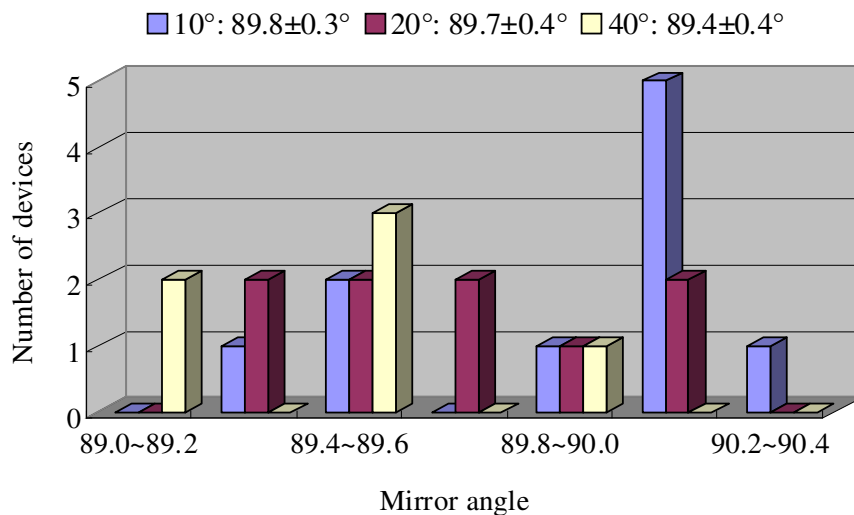


Figure 4-12 Measured angle of mirrors with different side latches angles.

4-5 Corner cube reflector

A corner cube reflector was assembled by the one-push method. The optical micrographs are shown in Figure 4-13 and the SEM photographs are shown in Figure 4-14. As Figure 4-14 shows, the corner cube reflector is constructed by two 90°

mirrors. The reflecting zone of the corner cube reflector is $(760\mu\text{m})^3$. The three reflecting surfaces are the front side of Mirror 1, backside of Mirror 2, and the surface of substrate underneath Mirror 2. The angles of the corner cube reflector surfaces measured by an optical microscope were 89.9° between Mirror 1 and substrate, 89° between Mirror 2 and substrate, and 90° between Mirror 1 and Mirror 2, with a measurement resolution of 0.15° . The deviation from the Mirror 2 and substrate needs to be improved. The deviation can be solved by adding locking mechanism between Mirror 1 and Mirror 2.

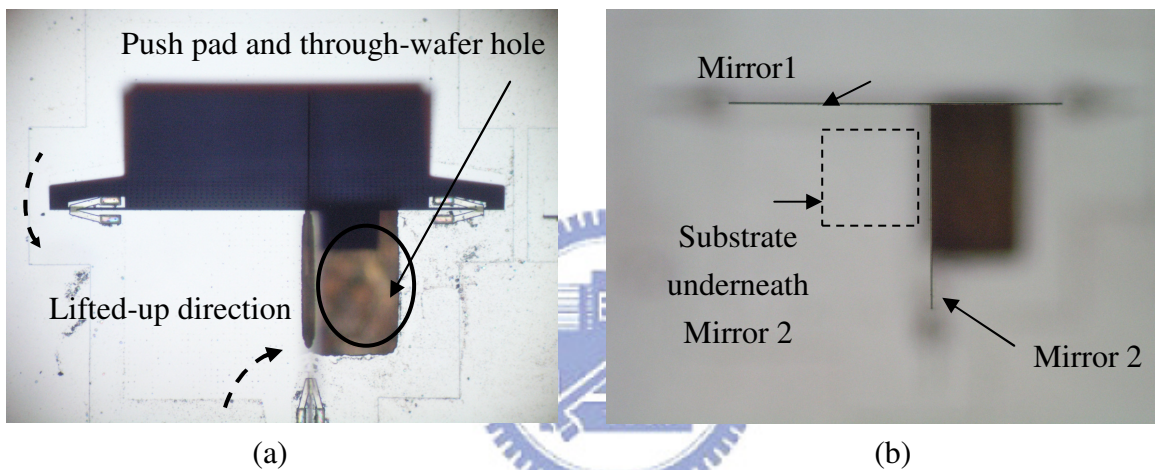


Figure 4-13 (a) Assembled corner cube reflector, (b) surfaces of the corner cube reflector.

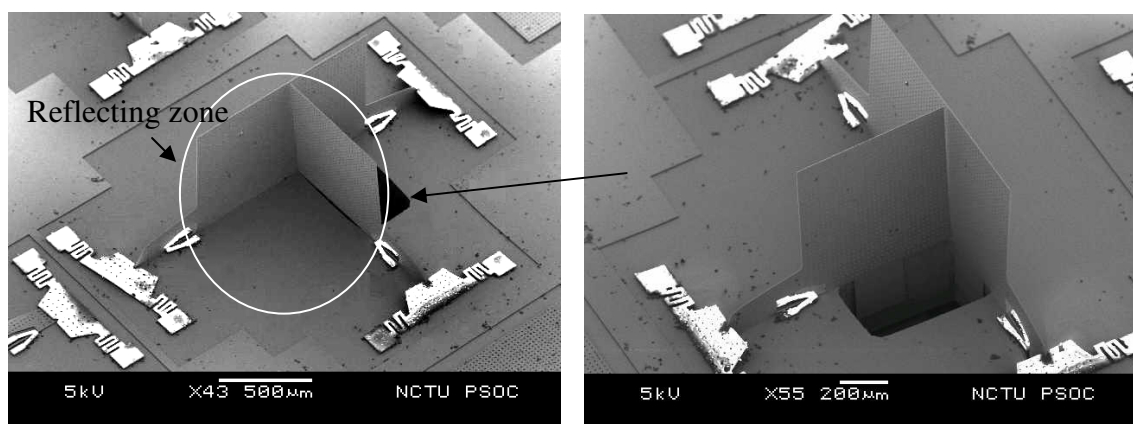


Figure 4-14 SEM photograph of the fabricated corner cube reflector.

4-5-1 Optical measurement

Light reflected from the corner cube reflector was measured optically as shown in Figure 4-15. The laser beam was first weakly focused by a lens with a focal length of 10 cm. The focused light was then divided by the beam splitter. The dotted line in Figure 4-15 is the reflected light by the beam splitter whereas the solid line is the transmitted light. The reflected light was reflected again by the inner surface of the beam splitter and projected onto the screen. The transmitted light was reflected by the corner cube and then projected onto the screen. The distance between two projected spots was measured to derive the angle of the corner cube reflector. The experimental setup is shown as Figure 4-16.

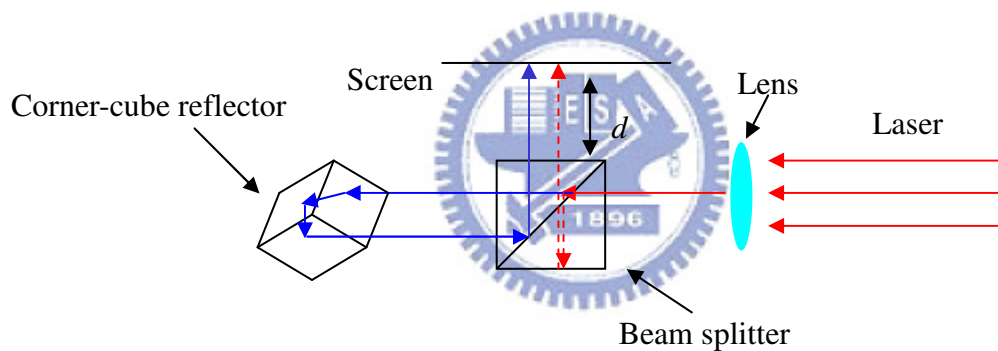


Figure 4-15 Illustration of the optical measurement.

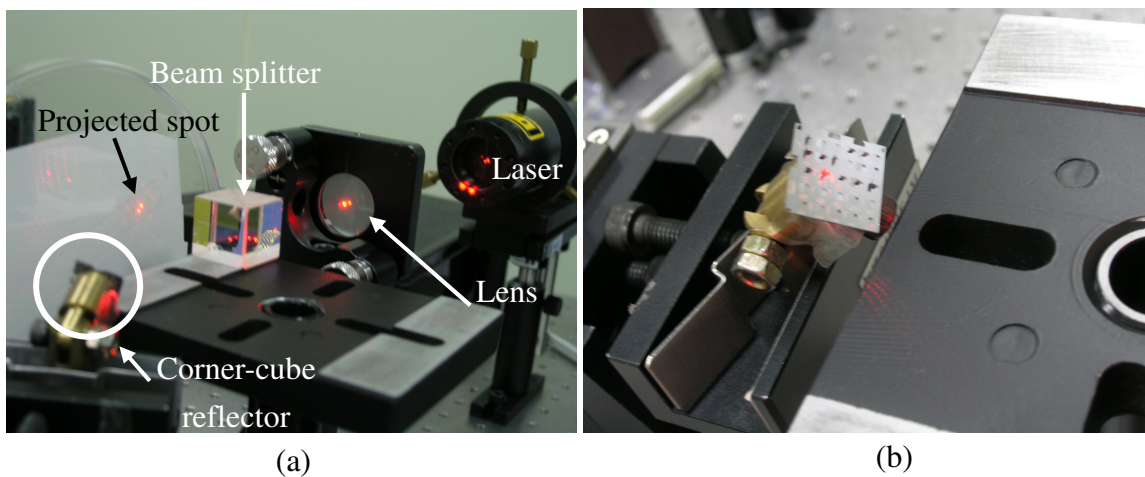


Figure 4-16 (a) Experimental setup, (b) highlight of the corner cube reflector.

Before the measurement, the optical path is aligned two steps. First the laser beam is aligned to be parallel to the optical table (Figure 4-17 (a)). Then the beam splitter and the lens are placed orthogonal to the laser beam (Figure 4-17 (b)), which can be obtained from the overlap between the reflected optical spot from the beam splitter and the emission aperture of the laser.

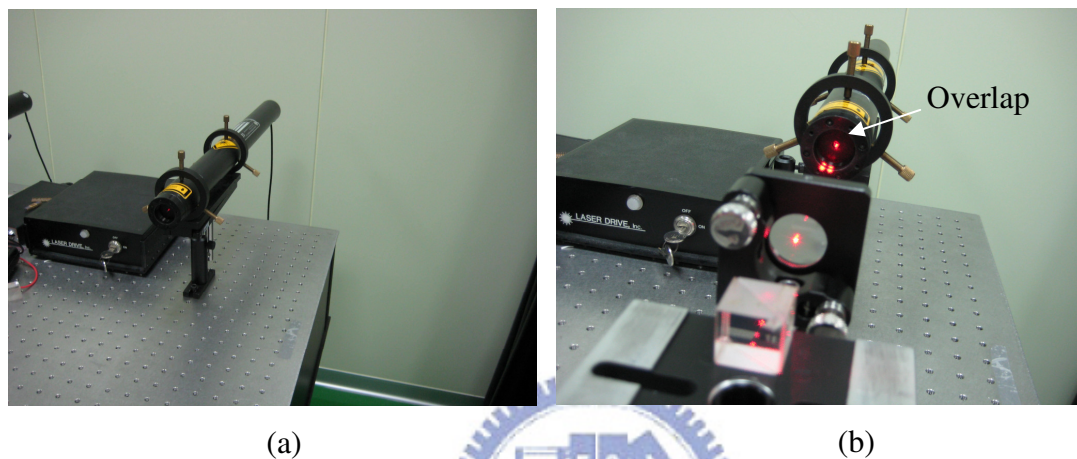


Figure 4-17 Optical path alignment, (a) laser beam alignment, (b) lens and beam splitter alignment.

Figure 4-18 shows the projected spots on the screen placed at $d = 10$ mm and 60 mm away from the beam splitter. The scale of the grid paper is 0.1 mm/div. The calculation of the deviation angle θ is shown in Figure 4-19. The distance between the screens in Figures 4-19 (a) and (b) is 50mm. The distance between the two spots is increased by 1 mm. The angle θ can be calculated as $\theta = \tan^{-1} \frac{3 \text{ mm} - 2 \text{ mm}}{50 \text{ mm}} = 1.15^\circ$.

The corner cube is rotated by various angles and the result is shown in Table 4-1.

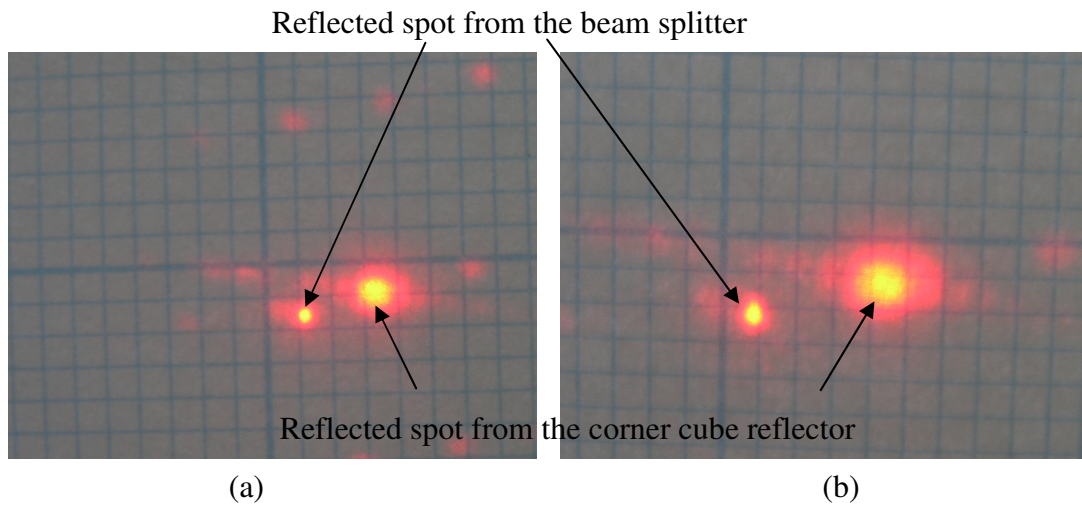


Figure 4-18 Reflected spots on the screen placed at (a) 10 mm, (b) 60 mm away from the beam splitter.

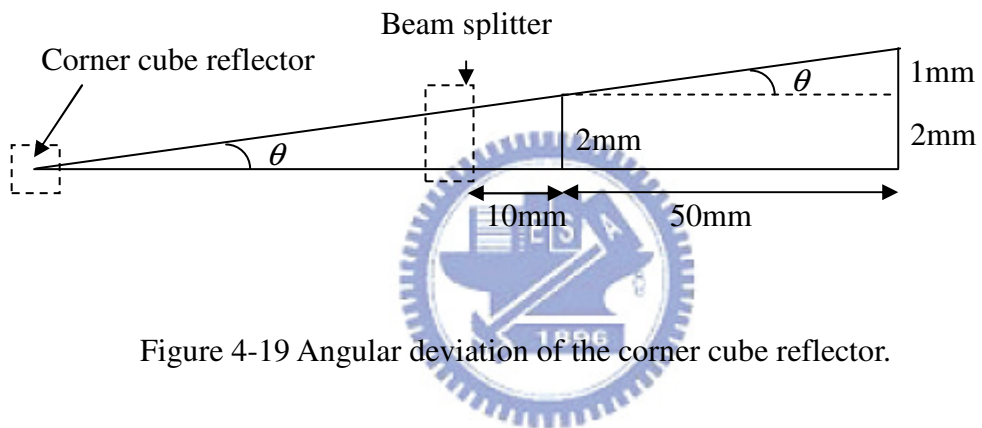


Figure 4-19 Angular deviation of the corner cube reflector.

Table 4-1 Angular deviation with various corner cube reflector orientations.

Measurement No.	Deviation
1	1.15°
2	0.92°
3	1.03°
4	1.60°
5	1.26°
6	1.15°
Average deviation	1.19° ± 0.4°

4-6 45° structures

Two types of 45° structures were designed in Chapter 2. The fabricated devices are presented in the following sections. The problems encountered in the assembly process will also be discussed.

4-6-1 Device 1

The SEM of the fabricated Device 1 are shown in Figure 4-20. Figure 4-20 (a) shows a 45° device before assembly. Figure 4-20 (b) shows the highlight of the support structure. Figure 4-20 (c) shows a 135° device. Figure 4-20 (d) shows the close-up view of the support structure.

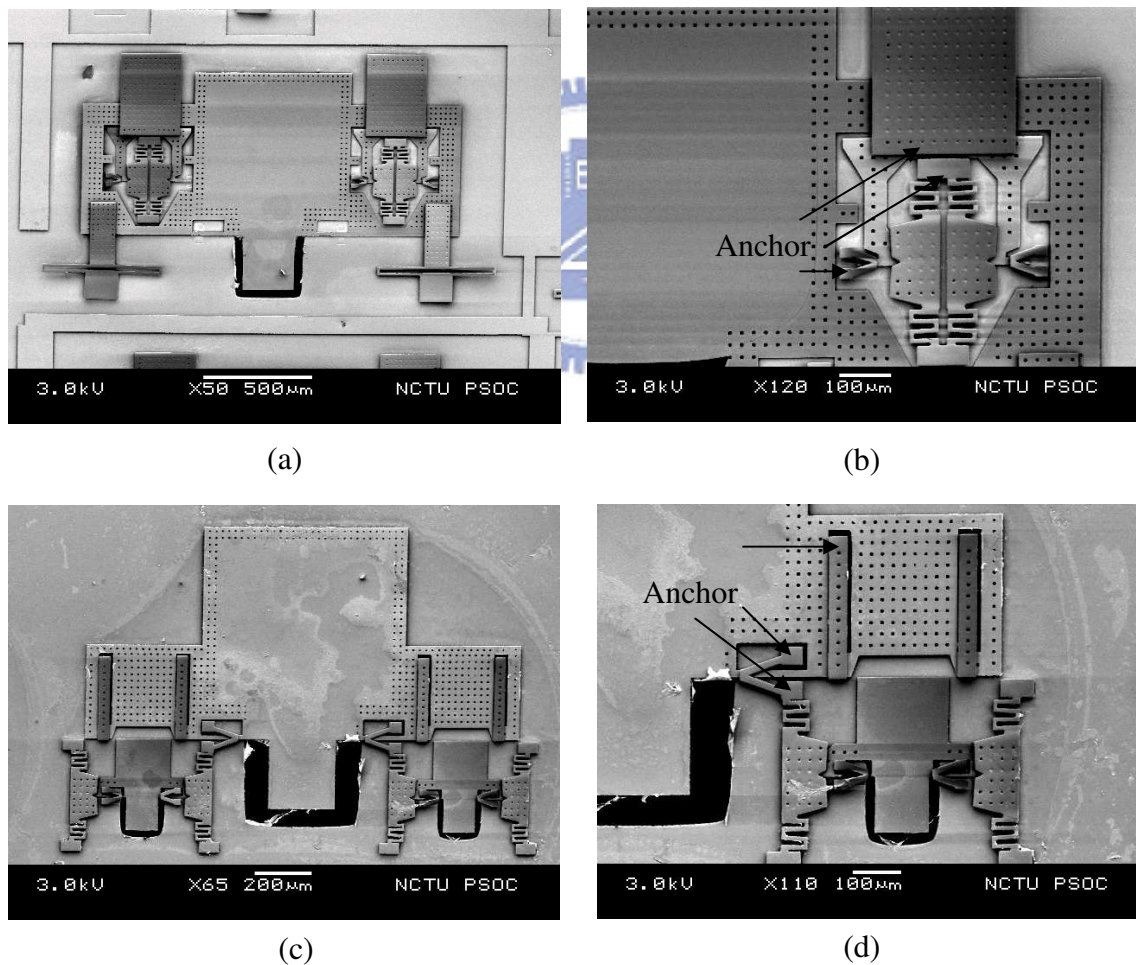


Figure 4-20 Fabricated Device 1, (a) 45° structure, (b) support of 45° structure (b) 135° structure, (d) support of 135° structure.

However, the assembly process failed due to a step in the bottom surface of the SU-8 structures, as shown in Figures 4-21 and 4-22. Because the oxide deposition process is not a planar process, the subsequently coated SU-8 will have a mechanical step in the bottom surface, which will result in the locking phenomenon during assembly. The associated photographs of the optical microscope are shown in Figure 4-21. Figure 4-22 is the cross section of Figure 4-21. The assembly process failed eventually. Figure 4-23 shows the SEM of a 135° device. In Figure 4-23 (a), a 135° device is assembled without the restoring force beams. However, the angle of the device without restoring force beams is unknown because the restoring force beams take no effect. In Figure 4-23 (b), the hinge pin was locked by the mechanical step and not on the axis because the imbalance of the force on the hinge pin since the restoring force beams on other side has been broken.

Cross section line in Figure 4-22

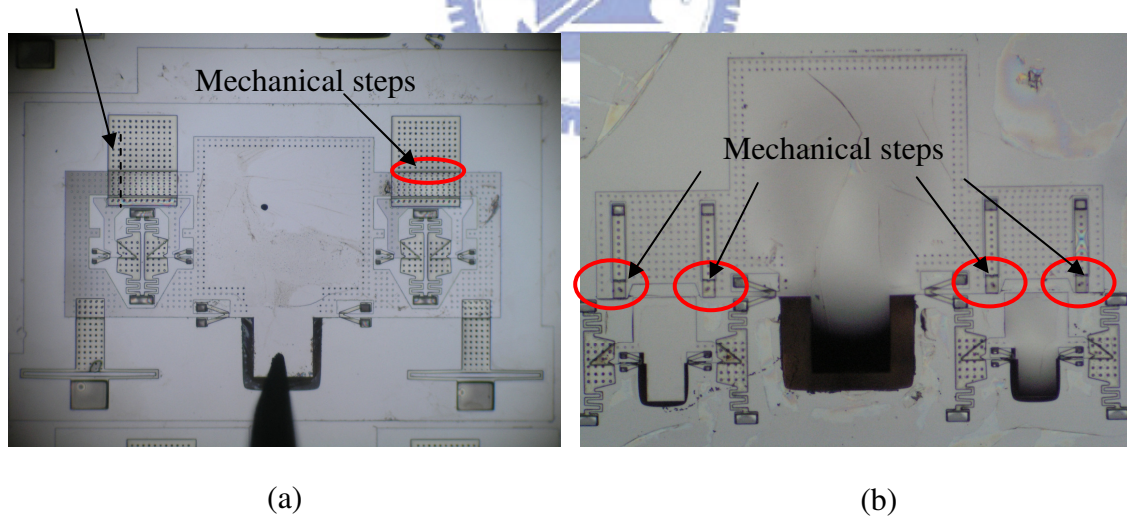


Figure 4-21 Mechanical steps in SU-8, (a) 45° device, (b) 135° device.

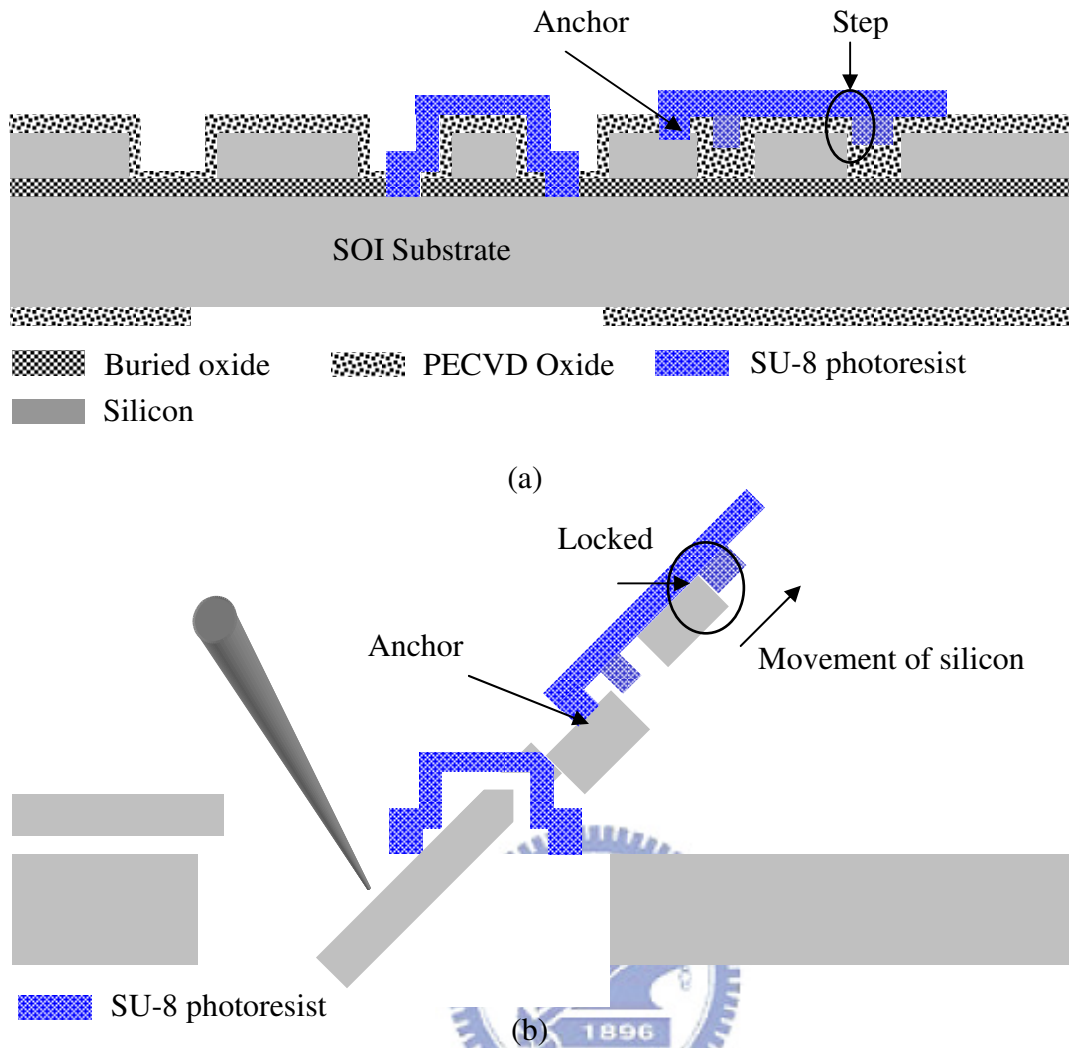


Figure 4-22 Cross sectional view, (a) After SU-8 process. (b) problem of the assembly process.

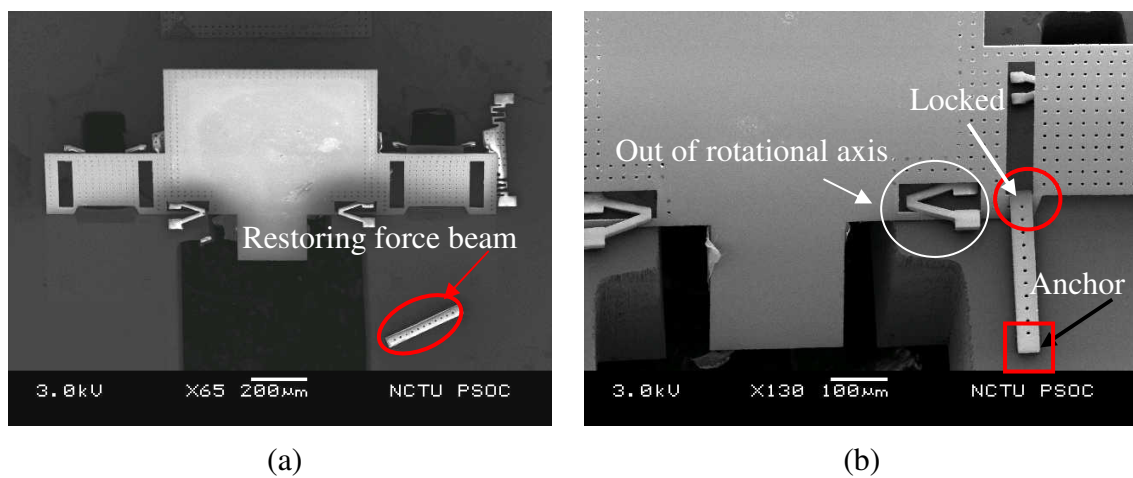


Figure 4-23 SEM of 135° devices, (a) restoring force beam was destroyed due to the step, (b) the step lock the structure out of rotational axis.

4-6-2 Device 2

Mirrors without SU-8 hinges and supports were also assembled to verify the feasibility of the proposed concept. Figure 4-24 shows the assembly process of the fabricated structure. Probe 1 was aligned with the push pad of the mirror (Figure 4-24 (a)). The mirror was pushed over 65° and Probe 1 stayed on the push pad (Figure 4-24 (b)). Then Probe 2 pushed the push pad of the support to $45\sim 55^\circ$ (Figure 4-24 (c)). As Probe 1 was removed from the mirror, the mirror lay firmly on the support due to the torsional beams of the mirror (Figure 4-24 (d)). Probe 2 was removed subsequently and then the support also lay on the mirror due to the torsional beams of the support (Figure 4-24 (e)). Finally the mirror and the support were interlocked at the desired angle.

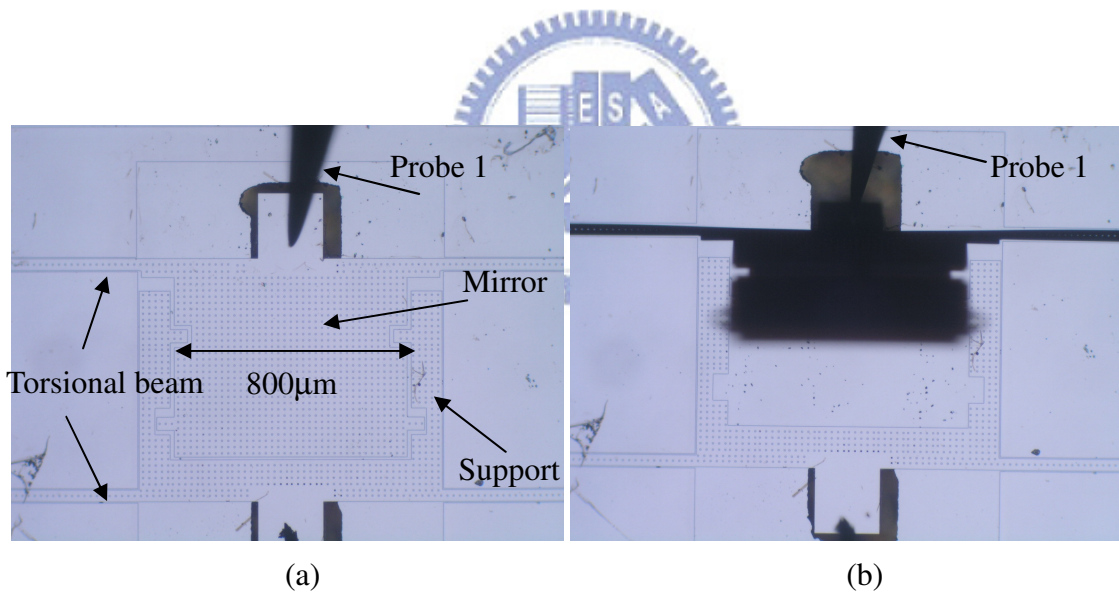


Figure 4-24 Assembly process of a 45° mirror without SU-8, (a) before assembly, (b) the mirror was first aligned and pushed up by Probe 1.

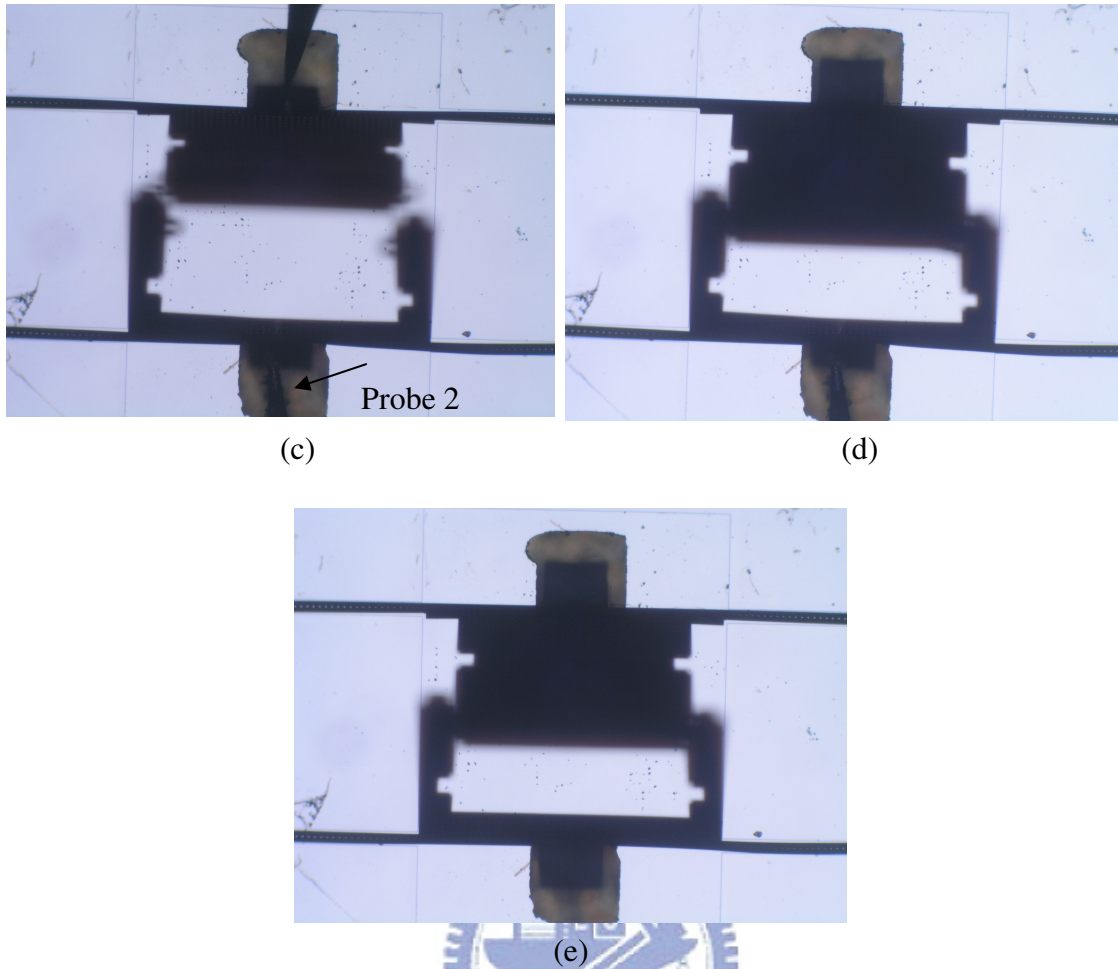


Figure 4-24 Assembly process of a 45° mirror without SU-8 (continued), (c) the support was pushed up by Probe 2, (d) Probe 1 was removed. (e) probe 2 was removed.

The SEM photographs of the assemble mirror are shown in Figure 4-25. Figure 4-25 (a) shows an assembled 45° mirror, whereas Figure 4-25 (b) shows the side view. Figure 4-25 (c) shows the angular interlock components. Figure 4-25 (d) shows the torsional beam and the mechanical stop which is used to prevent offset of the torsional beam.

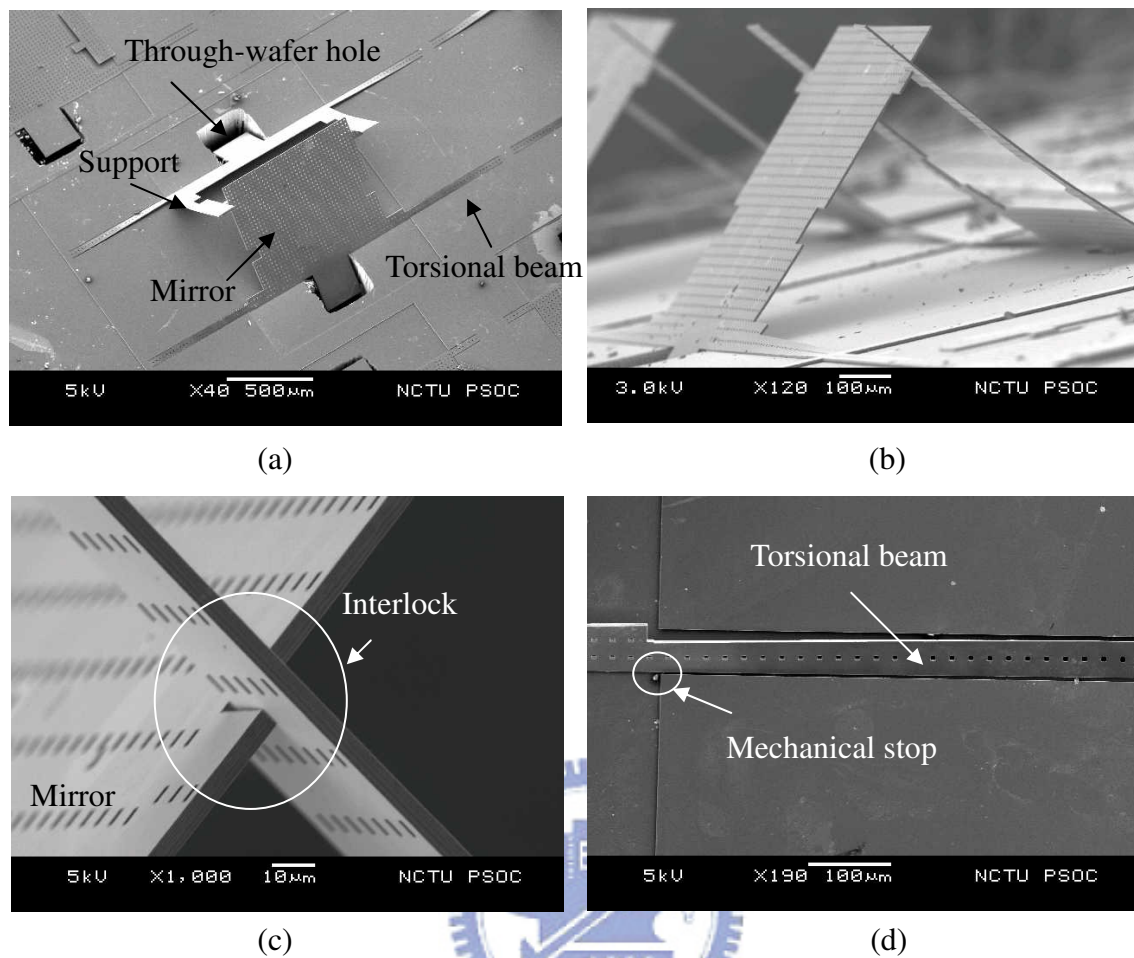


Figure 4-25 (a) An assembled 45° device, (b) side view of 45° device, (c) Highlight of the locking mechanism, (d) torsional beam and mechanical stop (continued).

4-6-2-1 Angle measurement

The angles of the assembled devices are defined by the layout design and should be 45°. The angles of the fabricated and assembled devices were measured by using SEM photographs. The resolution of the measured angle is 0.2°. The resolution is limited by the pixel of the SEM figures. Figure 4-26 shows the SEM photograph of an assembled sample and the geometric scale. The angle was calculated as 45.8°. Table 4-2 lists the angle measurement results of 7 samples. The average angle of them was $45.89^\circ \pm 0.2^\circ$.

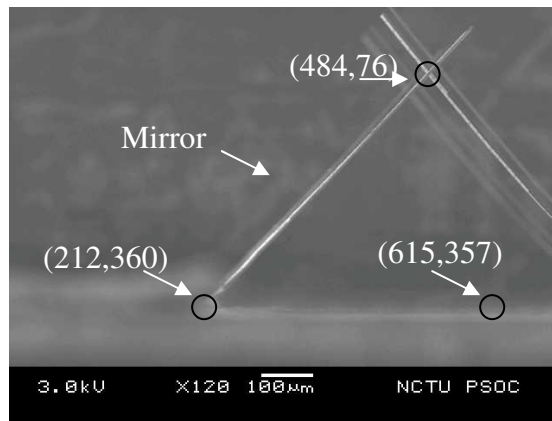


Figure 4-26 An assembled mirror at 45.8°.

Table 4-2 Angle measurement (resolution: 0.2°)

Sample number	Measured angle
1	45.9°
2	45.8°
3	46.0°
4	45.9°
5	45.8°
6	46.1°
7	45.7°
Average angle	45.89° ± 0.2°

The reason for the deviation from 45° is the bending of the supports. As the Figure 4-27 shows, the bent supports influence the assembled angle. Additionally, the thickness of the device layer was neglected in the angular calculation and it results in 0.4° deviation.

The deformation of the bent supports was measured by a WYKO NT1100 interferometer. Figure 4-28 (a) shows the 3-D profile of the bent supports. Figure 4-28 (b) shows the 2-D profile of the AB cut in Figure 4-28 (a). A finite element simulation is shown in Figure 4-29. Figure 4-29 (b) shows the simulated side view of the support.

From 4-28 (b), the bending occurs where the support structure has a smaller width, thus a weaker mechanical strength. In Figure 4-29 (b), the bending is observed in the same region. Therefore the torsional beam design needs to be improved. The bending can be eliminated by increasing the width of the support. A simulation with 50 μm wider support is shown in Figure 4-30. The support in Figure 4-30 is straight and the deviation due to the support can be solved.

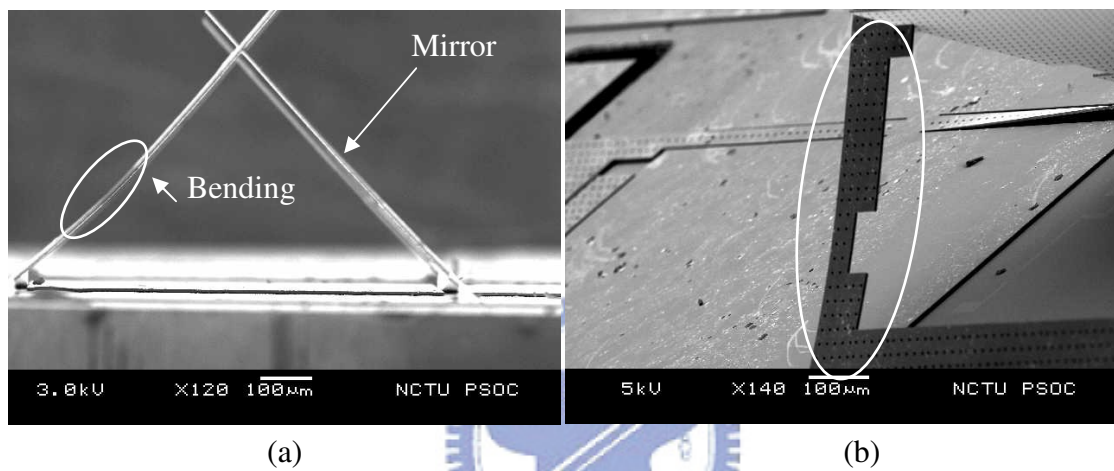


Figure 4-27 The bent supports, (a) side view, (b) perspective view.

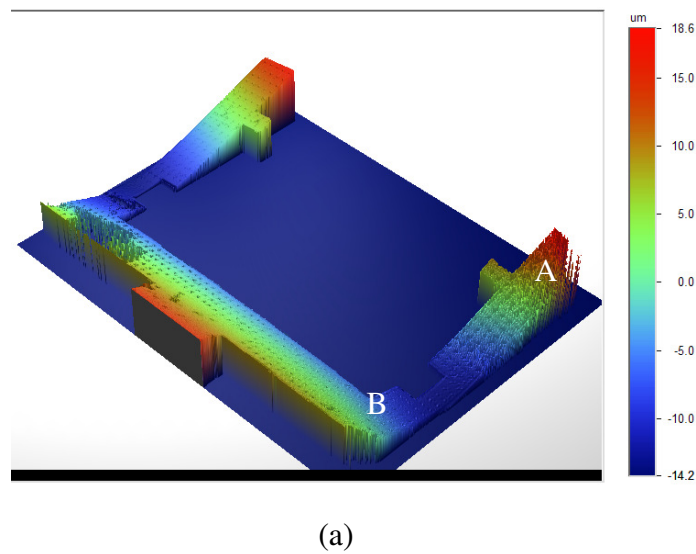


Figure 4-28 Bending of the supports after assembly, (a) 3-D profile.

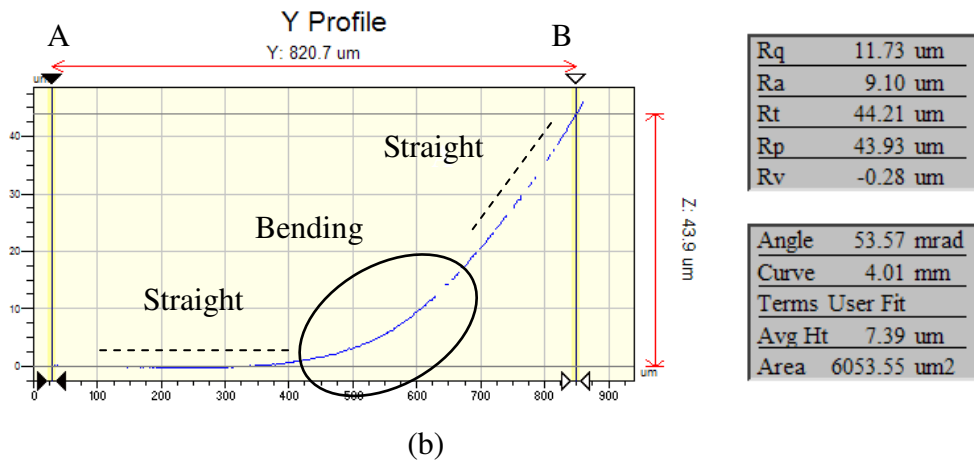


Figure 4-28 Bending of the supports after assembly, (b) 2-D analysis.

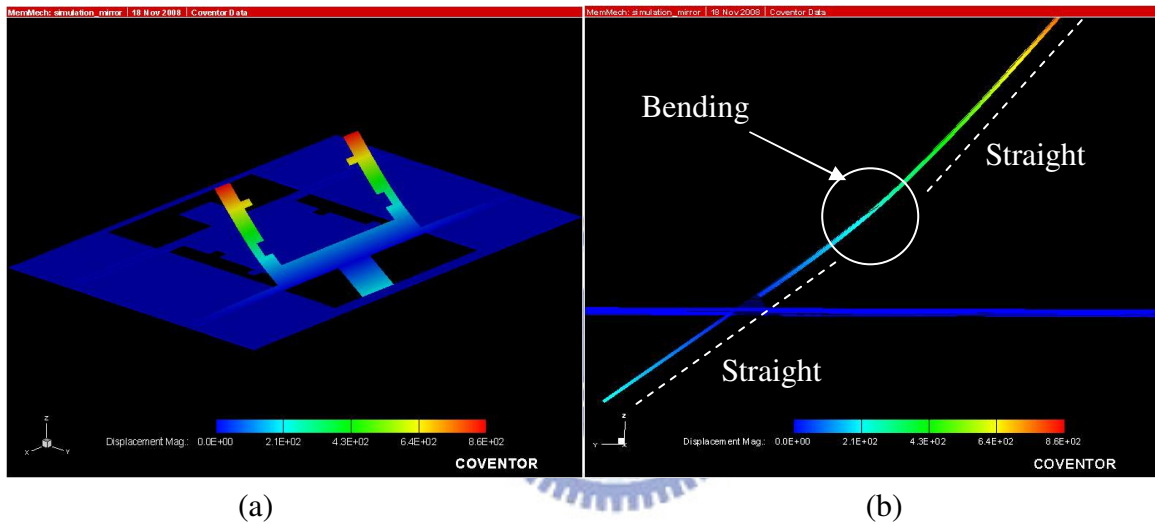


Figure 4-29 (a) Simulation of the support, (b) side view.

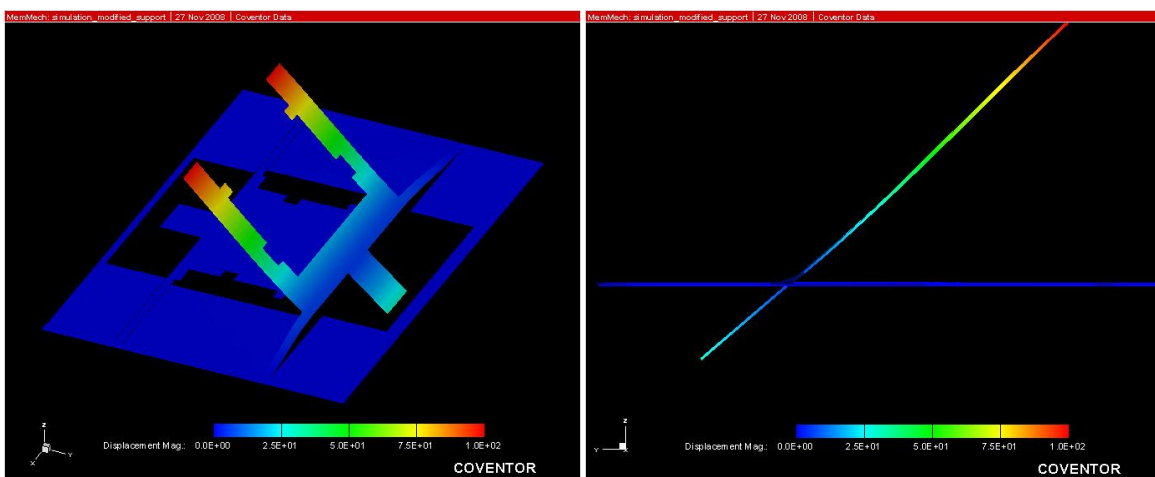


Figure 4-30 (a) Simulation of a thicker support, (b) side view.

4-6-2-2 Discussion

In assembly experiments, short torsional beams (e.g. 112 μm long) were easily broken during assembly procedure, as shown in Figure 4-31. Long beams (e.g. longer than 400 μm) were soft enough to avoid breaking. The maximum shear stress τ_{max} in a 400- μm -long torsional beam at $\theta = 80^\circ$ can be calculated by Equation 2-2 to be 1.2 GPa. Compared to the yield strength of 7 GPa, the safety factor is 5.8. Therefore the original design for a safety factor of 1.4 ($\tau_{\text{max}} = 5$ GPa in a 112- μm -long beam) is too aggressive. However, long beams with less restoring force may not drive the support and mirror to interlock firmly due to the friction force and result in more angular deviation. The trade-off between the two factors needs to be considered more carefully in the future.

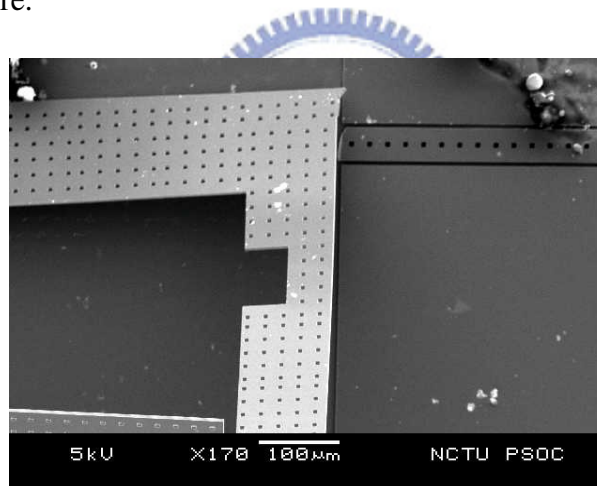


Figure 4-31 Broken torsional beam.

4-7 Summary

Batch assembly of more than one 90° devices was demonstrated and verified. It can reduce the assembling time on the wafer level. The V-shaped hinge was compared with the conventional hinge and the function of the V-shaped hinge was verified. The angular accuracy of the corner cube reflector was measured optically. The deviation is $1.19^\circ \pm 0.4^\circ$ and needs to be improved. The reasons of angular inaccuracy were discussed. The 90° device was improved to average $89.8 \pm 0.3^\circ$, compared to our previous study, $89.2 \pm 0.3^\circ$ [7]. The 45° devices were assembled at average $45.9 \pm 0.2^\circ$. The 45° devices need to be improved.



Chapter 5 Conclusion and Future work

5-1 Conclusion

Batch assembly of 90° devices was realized in this thesis. It can reduce the assembly time greatly on the wafer level. Furthermore, the problems of angular deviation of 90° devices were discussed and the angular inaccuracy were improved to average $89.8\pm 0.3^\circ$. For 90° devices, the function and the drawback of the V-shaped hinges were demonstrated. A corner cube reflector was fabricated and measured optically. The assembly method of the 45° structures was verified and demonstrated based on the one-push method.

5-2 Future work

Some of the problems encountered in this thesis need to be considered more carefully in the future. The thickness of the SOI device layer should be increased to 50 μm to increase the stiffness after reflective coating. The thickness of the SU-8 structural layer and the width of the hinge pin should be modified in the layout design. Since the thickness of the SU-8 should be increased with a thicker device layer, the SU-8 process with high aspect ratio needs to be considered, especially when the SU-8 release hole is only $(6\mu\text{m})^2$. The bending problem of the 45° structure can also be solved by a thicker device layer. However, the length and the geometry for the torsional beam needs to be redesigned for appropriate restoring force. The restoring force of the torsional beam is related to the bending problem of the support and the friction force on the interlock. For the beam problem in Section 4-6-2-2, the yield strength in different directions of the anisotropic silicon crystal lattice should be considered. The yield strength of 7 GPa used as the maximum sustainable shear stress in the current design is lack of consideration.

The assembly method can be used to fabricate an optical bench in the future, as shown in Figure 5-1. The laser beam is first emitted from the laser diode (LD) bonded on the SOI substrate. After the laser beam is reflected from Mirror 1, the light is focused on the disk by the objective lens. The reflected light from the disk is diffracted from the hologram optical element (HOE) on Mirror 1. The diffracted light is reflected from Mirror 2 and then detected by the photo detector (PD) on the substrate.

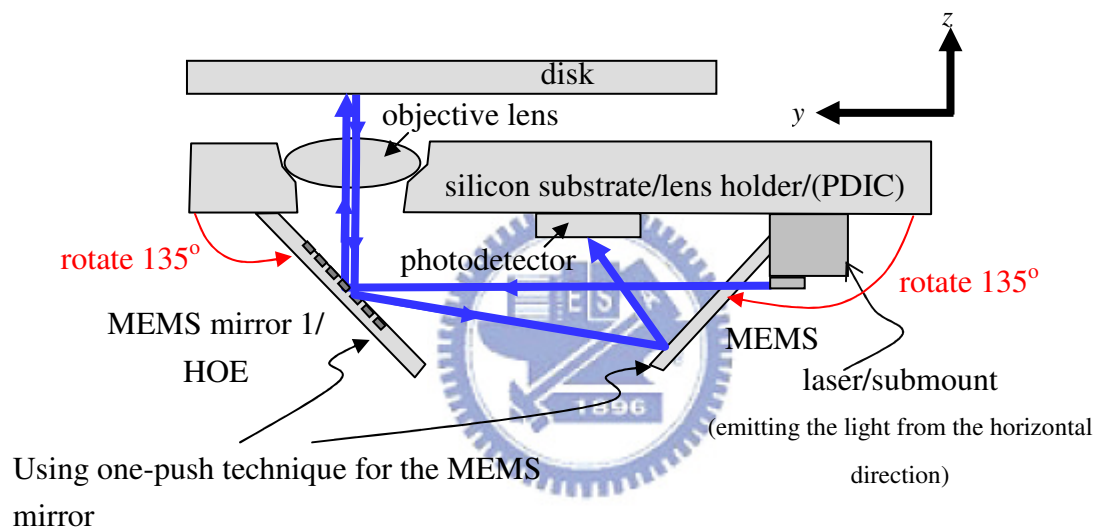


Figure 5-1 Micro optical bench.

The proposed fabrication process of the bench in Figure 5-1 is shown in Figure 5-2. The released structure is shown in Figure 5-2 (a). After the PD and LD are bonded on the substrate, they are wire bonded to the pads (Figure 5-2 (b)). Then the mirror is assembled by pushing the pads (Figure 5-2 (c)). Then a spacer such as silicon is bonded on the substrate to prevent destroying the structure in the next step (Figure 5-2 (d)). Finally the objective lens is bonded on the backside of the substrate and the optical bench is completed (Figure 5-2 (e)).

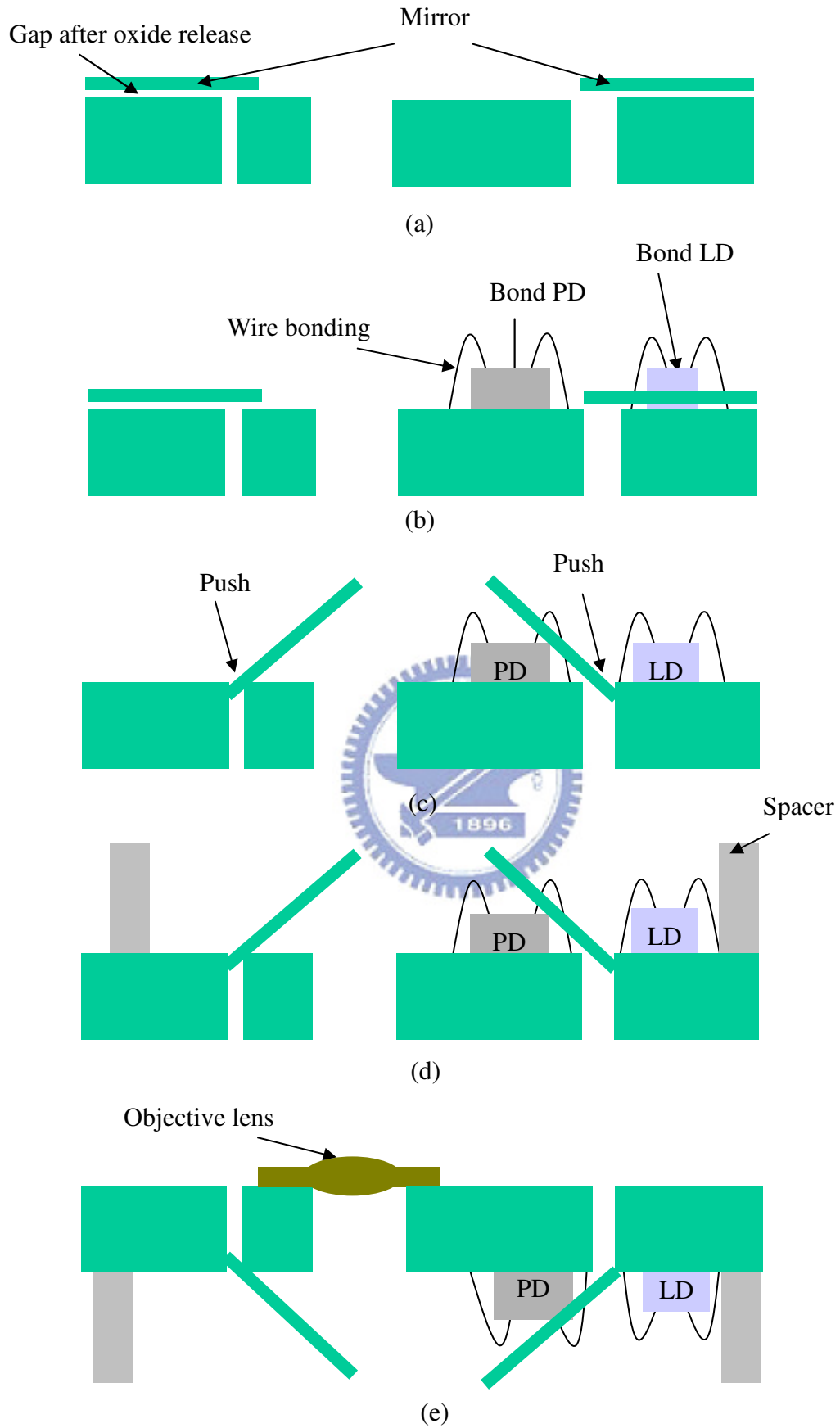


Figure 5-2 Fabrication process of the optical bench.

Reference

- [1] G. T. A. Kovacs, N. I. Maluf, and K. E. Petersen, "Bulk micromachining of silicon," *Proceedings of the IEEE*, vol. 86, no. 8, pp. 1536-1551, 1998.
- [2] J. M. Bustillo, R. T. Howe, and R. S. Muller, "Surface micromachining for microelectromechanical systems," *Proceedings of the IEEE*, vol. 86, no. 8, pp. 1552-1574, 1998.
- [3] C. Marques, Y. M. Desta, J. Rogers, M. C. Murphy, and K. Kelly, "Fabrication of high-aspect-ratio microstructures on planar and nonplanar surfaces using a modified LIGA process," *Journal of Microelectromechanical Systems*, vol. 6, no. 4, pp. 329-336, 1997.
- [4] L. Y. Lin, J. L. Shen, S. S. Lee, and M. C. Wu, "Realization of novel monolithic free-space optical disk pickup heads by surface micromachining," *Optics Letters*, vol. 21, no. 2, pp. 155-157, 1996.
- [5] A. Jain and H. Xie, "Microendoscopic Confocal Imaging Probe Based on an LVD Microlens Scanner," *IEEE Journal of Selected Topics in Quantum Electronics*, vol. 13, no. 2, pp. 228-234, 2007.
- [6] D. S. Greywall, P. A. Busch, F. Pardo, D. W. Carr, G. Bogart, and H. T. Soh, "Crystalline silicon tilting mirrors for optical cross-connect switches," *Journal of Microelectromechanical Systems*, vol. 12, no. 5, pp. 708-712, 2003.
- [7] W. Z. Huang, "Assembly of Three Dimensional Microstructures on SOI Wafers Using SU-8 Mechanisms," Master Thesis, Department of Electrical and Computer Engineering, National Chiao Tung University, Taiwan, 2007.
- [8] K. S. J. Pister, M. W. Judy, S. R. Burgett, and R. S. Fearing, "Microfabricated hinges," *Sensors and Actuators A: Physical*, vol. 33, no. 3, pp. 249-256, 1992.

- [9] A. Friedberger and R. S. Muller, "Improved surface-micromachined hinges for fold-out structures," *Journal of Microelectromechanical Systems*, vol. 7, no. 3, pp. 315-319, 1998.
- [10] T. Akiyama and K. Shono, "Controlled stepwise motion in polysilicon microstructures," *Journal of Microelectromechanical Systems*, vol. 2, no. 3, pp. 106-110, 1993.
- [11] L. Lih-Yuan, E. L. Goldstein, and R. W. Tkach, "On the expandability of free-space micromachined optical cross connects," *Journal of Lightwave Technology*, vol. 18, no. 4, pp. 482-489, 2000.
- [12] W. J. Robert, "Electrostatic self-assembly of raised surface micromachined structures for optics," Master Thesis, Department of Engineering Science, Simon Fraser University, Canada, 2000.
- [13] V. Kaajakari and A. Lal, "Electrostatic batch assembly of surface MEMS using ultrasonic triboelectricity," in *The 14th IEEE International Conference on Micro Electro Mechanical Systems*, pp. 10-13, 2001.
- [14] Y. W. Yi and C. Liu, "Magnetic actuation of hinged microstructures," *Journal of Microelectromechanical Systems*, vol. 8, no. 1, pp. 10-17, 1999.
- [15] E. Iwase and I. Shimoyama, "A design method for out-of-plane structures by multi-step magnetic self-assembly," *Sensors and Actuators A: Physical*, vol. 127, no. 2, pp. 310-315, 2006.
- [16] T. Ebefors, E. Kalvesten, C. Vieider, and G. Stemme, "New robust small radius joints based on thermal shrinkage of polyimide in V-grooves," in *International Conference on Solid State Sensors and Actuators*, pp. 675-678, 1997.
- [17] R. R. A. Syms, "Surface tension powered self-assembly of 3-D micro-optomechanical structures," *Journal of Microelectromechanical Systems*, vol. 8, no. 4, pp. 448-455, 1999.

- [18] R. R. A. Syms, E. M. Yeatman, V. M. Bright, and G. M. Whitesides, "Surface tension-powered self-assembly of microstructures - the state-of-the-art," *Journal of Microelectromechanical Systems*, vol. 12, no. 4, pp. 387-417, 2003.
- [19] V. A. Aksyuk, F. Pardo, D. Carr, D. Greywall, H. B. Chan, M. E. Simon, A. Gasparyan, H. Shea, V. Lifton, C. Bolle, S. Arney, R. Frahm, M. Paczkowski, M. Haueis, R. Ryf, D. T. Neilson, J. Kim, C. R. Giles, and D. Bishop, "Beam-steering micromirrors for large optical cross-connects," *Journal of Lightwave Technology*, vol. 21, no. 3, pp. 634-642, 2003.
- [20] D. C. Miller, Z. Wenge, and V. M. Bright, "Microrelay packaging technology using flip-chip assembly," in *The 13th Annual International Conference on Micro Electro Mechanical Systems*, pp. 265-270, 2000.
- [21] N. Dechev, W. L. Cleghorn, and J. K. Mills, "Microassembly of 3-D microstructures using a compliant, passive microgripper," *Journal of Microelectromechanical Systems*, vol. 13, no. 2, pp. 176-189, 2004.
- [22] S. H. Tsang, D. Sameoto, I. G. Foulds, R. W. Johnstone, and M. Parameswaran, "Automated assembly of hingeless 90° out-of-plane microstructures," *Journal of Micromechanics and Microengineering*, vol. 17, no. 7, pp. 1314-1325, 2007.
- [23] J. W. Wu, "MEMS Based Micro Optical Bench with Integration of SOI and SU-8," Master Thesis, Department of Electrical and Computer Engineering, National Chiao Tung University, Taiwan, 2006.
- [24] K. E. Petersen, "Silicon as a mechanical material," *Proceedings of the IEEE*, vol. 70, no. 5, pp. 420-457, 1982.
- [25] D. Bachmann, B. Schoerle, S. Kune, Y. Leiner, and C. Hierold, "Fabrication and characterization of folded SU-8 suspensions for MEMS applications," *Sensors and Actuators A: Physical*, vol. 130-131, no. pp. 379-386, 2006.

- [26] S. H. Tsang and M. Parameswaran, "Self-locking vertical operation single crystal silicon micromirrors using silicon-on-insulator technology," in *Canadian Conference on Electrical and Computer Engineering*, pp. 429-432, 2005.
- [27] R. Raymond and J. Raymond, "Torsion", in *Roark's formulas for stress and strain*, 6th edition: McGraw-Hill, 1989.
- [28] J. J. Wortman and R. A. Evans, "Young's Modulus, Shear Modulus, and Poisson's Ratio in Silicon and Germanium," *Journal of Applied Physics*, vol. 36, no. 1, pp. 153-156, 1965.
- [29] Y. Fukuta, H. Fujita, and H. Toshiyoshi, "Vapor Hydrofluoric Acid Sacrificial Release Technique for Micro Electro Mechanical Systems Using Labware," *Japanese Journal of Applied Physics*, vol. 42, no. 1, pp. 3690-3694, 2003.
- [30] G. G. Stoney, "The tension of metallic films deposited by electrolysis," *Proceedings of the Royal Society of London*, vol. 82, no. 553, pp. 172-175, 1909.
- [31] H. Windischmann, "An intrinsic stress scaling law for polycrystalline thin films prepared by ion beam sputtering," *Journal of Applied Physics*, vol. 62, no. 5, pp. 1800-1807, 1987.